UNIVERSIDAD POLITÉCNICA DE VALENCIA

DEPARTAMENTO DE COMUNICACIONES

Optical and Quantum Communications Group

Design and fabrication of customized fiber gratings to improve the interrogation of optical fiber sensors

PH.D. THESIS

AMELIA LAVINIA RICCHIUTI

Supervisor:
SALVADOR SALES MAICAS

Valencia, April 2016

Design and fabrication of customized fiber gratings to improve the interrogation of optical fiber sensors

Amelia Lavinia Ricchiuti
Optical and Quantum Communications Group (OQCG)
ITEAM Research Institute
Universidad Politécnica de Valencia (UPV)
Camino de Vera s/n, 46022 Valencia, SPAIN
amric1@iteam.upv.es

Valencia, April 2016

Acknowledgments

It is my great pleasure to take this opportunity to acknowledge all the people who contributed in some way to the work presented in this Ph.D. thesis.

Firstly, I would like to thank my academic supervisor Prof. Salvador Sales for giving me this great opportunity and allowing me to undertake my Ph.D. at Universidad Politécnica de Valencia in Spain. He gave me invaluable guidance, support, scientific contribution and also understanding during difficult times. I thank him for providing me intellectual freedom in my work, filling in the gaps in my knowledge and continuously engaging me in new ideas.

Additionally, I would like to express my sincere gratitude to Prof. José Capmany, leader of the *Optical and Quantum Communications Group* (GCOC), for his immense knowledge and constructive comments, but also for the warm atmosphere he cultivates within the group, creating a challenging and family-like environment.

I would also like to thank the various members of the GCOC for all the friendly discussions we had about science, research and life in general.

Special thanks goes to Prof. Luc Thévenaz for kindly hosting me at EPFL University in Switzerland during my two research stays. Through the collaboration between our groups, I received from him invaluable comments, technical criticisms and scientific contributions, which helped me grow professionally and personally.

My gratitude also goes to Prof. Francesco Prudenzano from Politecnico di Bari in Italy. I had the chance to work with some lovely people within his group, having a great time during my various scientific stays there.

Finally, I would like to express my sincere and warm gratitude to all the people whom I have constructively interacted and collaborated with during these remarkable Ph.D. years.

Abstract

Fiber grating sensors and devices have demonstrated outstanding capabilities in both telecommunications and sensing areas, due to their well-known advantageous characteristics. Therefore, one of the most important motivations lies in the potential of customized fiber gratings to be suitably employed for improving the interrogation process of optical fiber sensors and systems.

This Ph.D. dissertation is focused on the study, design, fabrication and performance evaluation of customized fiber Bragg gratings (FBGs) and long period gratings (LPGs) with the double aim to present novel sensing technologies and to enhance the response of existing sensing systems. In this context, a technique based on time-frequency domain analysis has been studied and applied to interrogate different kind of FBGs-based sensors. The distribution of the central wavelength along the sensing structures has been demonstrated, based on a combination of frequency scanning of the interrogating optical pulse and optical time-domain reflectometry (OTDR), allowing the detection of spot events with good performance in terms of measurand resolution. Moreover, different customized FBGs have been interrogated using a technology inspired on the operation principle of microwave photonics (MWP) filters, enabling the detection of spot events using radio-frequency (RF) devices with modest bandwidth. The sensing capability of these technological platforms has been fruitfully employed for implementing a large scale quasi-distributed sensor, based on an array of cascaded FBGs. The potentials of LPGs as fiber optic sensors has also been investigated in a new fashion, exploiting the potentials of MWP filtering techniques. Besides, a novel approach for simultaneous measurements based on a half-coated LPG has been proposed and demonstrated. Finally, the feasibility of FBGs as selective wavelength filters has been exploited in sensing applications; an alternative approach to improve the response and performance of Brillouin distributed fiber sensors has been studied and validated via experiments. The performance of the reported sensing platforms have been analyzed and evaluated so as to characterize their impact on the fiber sensing field and to ultimately identify the use of the most suitable technology depending on the processing task to be carried out and on the final goal to reach.

Resumen

Los sensores y dispositivos en fibra basados en redes de difracción han mostrado excepcionales capacidades en el ámbito de las telecomunicaciones y del sensado, gracias a sus excelentes propiedades. Entre las motivaciones más estimulantes destaca la posibilidad de fabricar redes de difracción *ad-hoc* para implementar y/o mejorar las prestaciones de los sensores fotónicos.

Esta tesis doctoral se ha enfocado en el estudio, diseño, fabricación y evaluación de las prestaciones de redes de difracción de Bragg (FBGs) y de redes de difracción de periodo largo (LPGs) personalizadas con el fin de desarrollar nuevas plataformas de detección y a la vez mejorar la respuesta y las prestaciones de los sensores fotónicos ya existentes. En este contexto, una técnica basada en el análisis tiempo-frecuencia se ha estudiado e implementado para la interrogación de sensores en fibra basados en varios tipos y modelos de FBGs. Se ha analizado la distribución de la longitud de onda central a lo largo de la estructura de sensado, gracias a una metodología que conlleva el escaneo en frecuencia del pulso óptico incidente y la técnica conocida como reflectometria óptica en el dominio del tiempo (OTDR). De esta manera se ha llevado a cabo la detección de eventos puntuales, alcanzando muy buenas prestaciones en términos de resolución de la magnitud a medir. Además, se han interrogado varias FBGs a través de una técnica basada en el principio de operación de los filtros de fotónica de microondas (MWP), logrando así la detección de eventos puntuales usando dispositivos de radio-frecuencia (RF) caracterizados por un moderado ancho de banda. La capacidad de sensado de estas plataformas tecnológicas ha sido aprovechada para la realización de un sensor quasi-distribuido de gran alcance, formado por una estructura en cascada de muchas FBGs. Por otro lado, se han puesto a prueba las capacidades de las LPGs como sensores ópticos según un enfoque novedoso; para ello se han aprovechados las potencialidades de los filtros de MWP. Asimismo, se ha estudiado y demostrado un nuevo método para medidas simultáneas de dos parámetros, basado en una LPG parcialmente recubierta por una película polimérica. Finalmente, se ha explotado la viabilidad de las FBGs en cuanto al filtrado selectivo en longitud de onda para aplicaciones de sensado; para ello se ha propuesto un sistema alternativo para la mejora de la respuesta y de las prestaciones de sensores ópticos distribuidos basados en el *scattering* de Brillouin. En conclusión, se han analizado y evaluado las prestaciones de las plataformas de sensado propuesta para caracterizar su impacto en el ámbito

de los sistemas de detección por fibra y además identificar el uso de la tecnología más adecuada dependiendo de la tarea a desarrollar y del objetivo a alcanzar.

Resum

Els sensors i dispositius en fibra basats en xarxes de difracció han mostrat excepcionals capacitats en l'àmbit de les telecomunicacions i del sensat, gràcies a les seus excel·lents propietats. Entre les motivacions més estimulants destaca la possibilitat de fabricar xarxes de difracció ad-hoc per a implementar i/o millorar les prestacions de sensors fotònics.

Esta tesi doctoral s'ha enfocat en l'estudi, disseny, fabricació i avaluació de les prestacions de xarxes de difracció de Bragg (FBGs) i de xarxes de difracció de període llarg (LPGs) personalitzades per tal de desenvolupar noves plataformes de detecció i al mateix temps millorar la resposta i les prestacions dels sensors fotònics ja existents. En este context, una tècnica basada en l'anàlisi temps-freqüència s'ha estudiat i implementat per a la interrogació de sensors en fibra basats en diversos tipus i models de FBGs. S'ha analitzat la distribució de la longitud d'ona central al llarg de l'estructura de sensat, gràcies a una metodologia que comporta l'escaneig en freqüència del pols òptic incident i la tècnica coneguda com reflectometria òptica en el domini del temps (OTDR). D'esta manera s'ha dut a terme la detecció d'esdeveniments puntuals, aconseguint molt bones prestacions en termes de resolució de la magnitud a mesurar. A més, s'han interrogat diverses FBGs a través d'una tècnica basada en el principi d'operació dels filtres de fotònica de microones (MWP), aconseguint així la detecció d'esdeveniments puntuals utilitzant dispositius de ràdio-freqüència (RF) caracteritzats per un moderat ample de banda. La capacitat de sensat d'aquestes plataformes tecnològiques ha sigut aprofitada per a la realització d'un sensor quasi-distribuït a llarga escala, format per una estructura en cascada de moltes FBGs. D'altra banda, s'han posat a prova les capacitats de les LPGs com a sensors òptics segons un enfocament nou; per a això s'han aprofitat les potencialitats dels filtres de MWP. Així mateix, s'ha estudiat i demostrat un nou mètode per a mesures simultànies de dos paràmetres, basat en una LPG parcialment recoberta per una pel·lícula polimèrica. Finalment, s'ha explotat la viabilitat de les FBGs pel que fa al filtrat selectiu en longitud d'ona per a aplicacions de sensat; per això s'ha proposat un sistema alternatiu per a la millora de la resposta i de les prestacions de sensors òptics distribuïts basats en el scattering de Brillouin. S'han analitzat i avaluat les prestacions de les plataformes de sensat propostes per a caracteritzar el seu impacte en l'àmbit dels sistemes de

detecció per fibra i a més identificar l'ús de la tecnologia més adequada depenent de la tasca a desenvolupar i de l'objectiu a assolir.

Contents

List of Acronyms

APC Angled polished connector
ASE Amplified spontaneous emission
BBS Broadband source
BOTDA Brilloiun optical time domain analysis
BOTDR Brilloiun optical time domain reflectrometry
BS Brilloiun scattering
CW Continuous wave
DBG Dynamic Brillouin grating
DC Direct current
DTG Draw tower grating
DUT Device under test
EDFA Erbium doped fiber amplifier
EMI Electromagnetic interference
EOM Electro-optical modulator
FBG Fiber Bragg grating
FSR Free spectral range
FT Fourier transform
FWHM Full width at half maximum
HBFLM High-birefringence fiber loop mirror
IMF Index-matching fluid
IFT Inverse Fourier transform
LbL Layer-by-layer
LPG Long period grating
MI Modulation instability
MMF Multimode fiber

MMI Multimode interference

MZI Mach-Zehnder interferometer

MZM Mach-Zehnder modulator

MW Microwave

MWP Microwave photonics

OFDR Optical frequency domain reflectometry

OLCR Optical low-coherence reflectometry

OSA Optical spectrum analyzer

OTDR Optical time domain reflectometry

PC Polarization controller

PD Photo-detector

PMF Polarization maintaining fiber

POF Plastic optical fiber

RF Radio-frequency

RH Relative humidity

RI Refractive index

SBS Stimulated Brilloiun scattering

SMF Single mode fiber

SNR Signal-to-noise ratio

SOA Semiconductor optical amplifier

SOCF Synthesis of optical coherence function

TDM Time-division multiplexing

TLS Tunable laser source

UV Ultraviolet

VNA Vector network analyzer

VOA Variable optical attenuator

WDM Wavelength division multiplexer

List of Figures

Chapter 1

Introduction

The discovery and development of fiber optic technology has had an immeasurable impact on both the technological and scientific worlds. Over the past four decades, fiber optics have been applied in many different fields, including medical area, military field, industry, networking, and communication systems. Although the area of fiber optics itself is actually very broad, one of the largest contributions it has made is in the world of telecommunications where optical fibers made possible high quality, large capacity and long distance links. In addition to the applications in telecommunications, fiber optics are also massively used in the growing field of fiber sensing systems.

Over the years, fiber optic devices have turned into one of the core technologies in a variety of sensing applications due to their advantageous characteristics such as simplicity, small size, light weight, low insertion loss, low cost, and the ability to make multiple distributed measurements along the fiber length. Furthermore, since optical fibers are made of dielectric material, they are non conducting, immune to electromagnetic interference (EMI), chemically inert, spark free and extraordinarily resistant to corrosive environments [1]. All these attractive characteristics are highly desirable for remote interrogation from long distance and/or in harsh environments.

However, although the important advantages offered by fiber optic sensors, the latter still result in relatively few commercial applications. Besides, despite the advancements in optical fiber manufacturing, basic optical components like mirrors, reflectors and wavelength filters have been a challenge to integrate with optical fibers. Grating-based structures, such as fiber Bragg gratings (FBGs) and long period gratings (LPGs) are examples of the type of sensors and devices which can provide this capability and overcome such limitations.

The discovery of the possibility to alter the refractive index (RI) of the core in an optical fiber by optical absorption of ultraviolet (UV) light have profoundly changed this scenario. The photo-sensitivity of optical fibers allows a permanent periodic, quasi-periodic or aperiodic change in the RI of the core of the fiber. In this branch, FBGs, with a sub-micron period, couple light from the forward propagating mode to the backward counter-propagating mode [2]. This coupling occurs at a specific wavelength, defined by the Bragg conditions, which depend on both the period and RI of the propagating mode. Indeed, a change in either of these parameters, caused by a change in strain and/or temperature, results in a shift of the Bragg wavelength, setting the foundation for FBG-based sensors [3]. Moreover, FBGs result to be a key components in optical and communication systems since they are able to perform many primary functions, such as signal reflection and filtering, in a highly efficient, low loss manner. For these reasons, FBGs have been widely used to perform a number of significant applications, such as wavelength filtering and multiplexing, fiber lasers fabrication, compensation for dispersion and polarization, fiber optic sensors, among others [4].

Furthermore, LPGs, having a periodicity in the range from 100 μm to 1 mm, act coupling light from the propagating core mode to the co-propagating cladding modes, producing a series of attenuation bands in the transmission spectrum, centered at discrete wavelengths [5]. The resonance wavelengths of these attenuation bands result to be sensitive to the local environment experienced by the fiber, making the LPGs a good candidate for fiber optics sensors. For these reasons, in recent years, fiber optic sensors based on LPGs have attracted growing interests due to the fact that they are able to measure various physical parameters, such as RI, temperature, strain, bending and liquid level, amongst others [6].

In the field of all-optical grating-based sensors, other important components are the dynamic Brillouin gratings (DBGs). This kind of weak FBG-like devices can be temporarily generated at any location along the entire length of a polarization maintaining fiber (PMF). Actually, a DBG can be created by stimulated Brillouin scattering between two pump pulses that are co-polarized along one principal axis of a PMF. Once this transient Brillouin grating has been created, it could be interrogated by an incoming probe signal if this is polarized along the orthogonal principal axis [7]. This is because of the DBG behaves similar to a FBG and its reflected spectrum is linearly proportional to the pump power. As the grating characteristics are affected by both strain and temperature reflected in the Brillouin frequency, DBGs have also been employed in sensing applications [8, 9].

1.1 Distributed fiber optics sensors

In many sensing applications, the parameter to be measured is detected at a specific position, as schematically illustrated in Fig. 1.1(a). This "point" measurement capability is widely applied for fiber optic sensors such as pressure probe, pH and RI sensors, among others. Over the years, fiber optic point sensors have been massively employed due to their compactness and performance. However, in many practical applications, the capability to spatially discriminate the measurand at different positions along the entire fiber length is desirable. In this case, shown in Fig. 1.1(b), distributed optical sensors can continuously interrogate the device within the whole sensing range, leaving no event undetected. If the optical fiber results not sensitive along its entire length, but is locally sensitized at certain discrete points, the system is known as "quasi-distributed" sensing system, as depicted in Fig. 1.1(c).

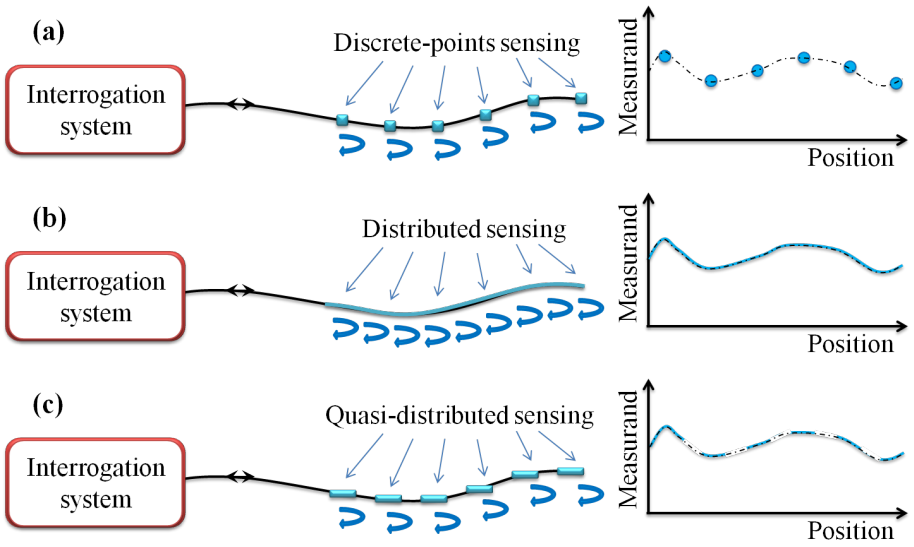

Figure 1.1: Schematic concepts for (a) discrete-point sensing, (b) distributed sensing and (c) quasi-distributed sensing.

Several distributed optical fiber sensors have been developed, as they present the key advantage that the entire optical fiber itself can be turned into a linear sensing element. In this context, optical time-domain reflectometry (OTDR) is an optical pulse-echo technique consisting of launching an optical pulse into the optical fiber under test and then measuring the back-scattered light (Rayleigh or Fresnel reflection) as a function of the time, which, in turn is directly related to each position along the fiber [10]. Indeed, the location d of a certain point along the fiber from the input connector is proportional to the related round-trip time

of the light Δt, according to

$$d = \frac{\Delta t \cdot c}{2n_g} \tag{1.1}$$

being n_g the group RI and c the speed of light in vacuum. Analogously, the spatial resolution δd is related to the input pulse duration t_p, according to

$$\delta d = \frac{t_p \cdot c}{2n_g}. \tag{1.2}$$

For the OTDR-based systems, the maximum measurement range is ultimately dictated by the back-and-forth losses arising from material absorption or cracks in the fiber. OTDR techniques have demonstrated distributed measurements over ranges of tens of kilometers with meter-sized spatial resolution.

Also based on Rayleigh scattering but now implemented in frequency domain, optical frequency-domain reflectometry (OFDR), has allowed temperature and strain measurements over long ranges (several tens of meters) with a sub-millimeter-sized spatial resolution and a level of precision equal to a few micro-deformation (for strain measurements) and to a tenths of Celsius degree (for temperature measurements) [11]. This performance has been obtained by combining OFDR with an advance correlation method: strain and temperature changes are detected by calculating local changes on optical path from cross-correlation function between the ongoing OFDR trace and a reference trace. In addition to this complex correlation method, OFDR presents a sophisticated scheme as it requires post processing and an auxiliary interferometer in order to avoid any non-linearity. Moreover, the systems results polarization dependent and thus requires the presence of a polarization beam splitter and two separate photo-detectors (PDs) to mitigate signal fading due to the polarization misalignment of the interfering measurement and reference fields.

Another approach for long range distributed sensing is based on optical low-coherence reflectomerty (OLCR) [12]. This simple method, essentially based on an interferometric structure, has been widely employed for measuring optical reflectivity as a function of distance. OLCR technique has demonstrated very good performance in terms of spatial resolution and reflection sensitivity when compared to direct-detection techniques such as OTDR and OFDR, offering advantages in both theoretical performance and practical application. However, the OLCR scheme presents a limited measurement range and a slow response time.

Furthermore, in the area of distributed fiber optic sensors, great interest has been focused on Brillouin scattering based schemes, because of their potential for performing large scale measurements, replacing thousands of point sensors due to their precision and high spatial resolution and accuracy. In this scenario, one of the systems allowing high sensing performance is Brillouin optical time-domain analysis (BOTDA), which used two counter-propagating lasers and took advantage of Brillouin amplification called stimulated Brillouin scattering (SBS) [13]. The operation principle and peculiarities of BOTDA can be found in chapter 5. Later on, a development to BOTDA has been presented based on a modified OTDR scheme, so called Brillouin optical time-domain reflectometry (BOTDR) [14]. In this system, the weak Brillouin back-scattered light is coherent mixed with a local oscillator laser; by changing the frequency difference between the pump source and local oscillator laser, the Brillouin frequency can be mapped along the entire length of the sensing fiber.

Certainly, many other methods and technologies have been investigated and presented in literature to continuously interrogate fiber optic sensors, however they are outside the scope of this work so will not be included in this dissertation.

1.2 Thesis objectives

The main goal of this work has been focused on the study, design and performance evaluation of customized FBGs and LPGs with the aim to improve the interrogation process of optical fiber sensors. Moreover, novel systems and technologies able to interrogate liquid level and strain/temperature sensors have been investigated and experimentally validated. The systems and technologies under study are basically founded on the measurement of the central frequency distribution of the grating based on time-frequency domain analysis and microwave photonics (MWP) filtering techniques. Furthermore, the main characteristics of LPGs have been investigated in order to perform simulation and experiments with the aim to realize novel platforms for LPG-based optical sensors. Finally, a technique to enhance the response and performance of Brillouin distributed fiber sensors has been investigated and validated, based on two arrays of FBGs.

The overall objectives of this Ph.D. thesis embraces different specific aims that have been properly accomplished:

1. Design novel and more efficient platform for distributed fiber optics sensors based on fiber grating structures.
2. Develop theoretical and numerical analysis to understand the process beyond the proposed techniques.
3. Propose new grating-based devices that when suitably combined with novel sensing platform can be practically used to implement temperature and strain sensing systems.

4. Exploit the potentials of polymeric coating and the high sensitivity of LPGs for simultaneous measuring two different magnitudes.
5. Apply customized FBGs as selective wavelength filters to improve the response and performance of Brillouin-based distributed fiber sensors.

1.3 Structure of the thesis

The content of this dissertation has been addressed in four main chapters, being each of them adequately focused in one of the different technological platforms embraced by the aforementioned objective.

In chapter 2, a simple scheme to measure the distribution of the central wavelength along different kinds of FBG-based sensors is proposed and demonstrated, based on time-frequency domain analysis. The measurement system is essentially based on a combination of frequency scanning of the interrogating optical pulse and OTDR technique [10]. Firstly, an optical input pulse, having a duration much shorter than the transit time through the grating, has been employed. By monitoring the reflected pulse by means of an oscilloscope, a liquid-level sensor is achieved, while the temperature of the liquid has been measured by an optical spectrum analyzer (OSA). The same technique has been further developed in order to implement a system able to detect the presence and location of a temperature gradient. In this case, the temperature measurements have been performed by the progressive scanning of the tunable laser. This permits the elimination of the OSA from the setup, simplifying the measurement scheme. Finally, a 5 m long cascaded-FBGs sensor has been used and the time-frequency domain analysis of the Bragg-frequency distribution along the long range sensor has been performed. By controlling the central frequency of the incident pulse, a time-resolved interrogation of spectral profiles of the cascaded-FBGs sensors has been obtained, allowing the detection of the position and length of spot events along the sensor with good performance in terms of measurand resolution.

Chapter 3 focuses on a novel technique for interrogating FBGs-based photonic sensors, dedicated to detect the presence and the precise location of several spot events. The principle of operation is based on a technique used to analyze MWP filters. The overall idea within this chapter has been developed and demonstrated step by step: firstly, we have demonstrated the possibility of using the MWP filtering technique to interrogate a 10 cm-long high reflectivity FBG as spot sensing device. However, due to the high reflectivity of the FBG, the most important limitation arises from the fact that the system is not able to detect events having the same magnitude. To overcome this limitation a pair of low-reflectivity FBGs has been applied as sensing device, allowing the detection of spot events, even if they have the same magnitude. Finally, a large scale fiber optic sensor based on ultra weak FBGs has been proposed, demonstrating the detection of spot events using radio-frequency (RF) devices with a modest bandwidth of only 500 MHz.

The potentials of LPGs as fiber optic sensors are presented and demonstrated in chapter 4. First, a LPG, cascaded with a high-reflectivity FBG, has been employed as liquid level sensor, exploiting the potentials of MWP filtering techniques. This is, to the best of our knowledge, the first demonstration of a LPG sensor interrogated with a RF based method, so avoiding the use of wavelength scanning systems such as OSA. This novel liquid level sensor system presents the advantages of easy and well-established fabrication procedure together with the advantages of using MWP filters such as repeatability, stability and robustness against environmental changes. Besides, a novel approach for simultaneous temperature and humidity sensing based on a half-coated LPG has been proposed and validated. The LPG has been coated with humidity sensitive nanostructured polymeric thin films by layer-by-layer (LbL) nano assembly technique. Then, half of the coating has been chemically removed, yielding to the split of the main attenuation band into two separated contributions, presenting different behaviors for humidity and temperature. To our knowledge, this is the first time that a single LPG is partially coated to develop a sensing device, allowing simultaneous response for two different external magnitudes.

The feasibility of FBGs as selective wavelength filters has been exploited in the sensing application presented in chapter 5, where an alternative approach to improve the response and performance of Brillouin distributed fiber sensors has been demonstrated. The technique requires the generation of pump and probe signal spread over different spectral components. While the power of each frequency component is still limited by the onset of nonlinear effects, the total amount of power launched into the sensor can be significantly increased, so as leading to a sensor response improvement. Two arrays of customized FBGs have been used to apply a frequency dependent delay to the pump components to avoid nonlinear cross-interaction. Experimental measurements demonstrate the capability of the method to improve the SNR, while the detrimental nonlinear effects are not observed in spite of increased pump and probe powers.

Finally, conclusions and future perspectives are commented in chapter 6. An overall summary of the technological platform and sensing systems proposed is presented, followed by the additional studies and open research lines.

Every chapter opens with its own introduction section, providing more details about its overall content. Bibliographic references are given at the end of each chapter.

Bibliography

[1] B. Culshaw, "Optical fiber sensor technologies: opportunities and-perhaps-pitfalls," *J. Lightwave Technol.*, vol. 22, pp. 39–50, Jan 2004.

[2] T. Erdogan, "Fiber grating spectra," *J. Lightwave Technol.*, vol. 15, pp. 1277–1294, Aug 1997.

[3] A. Kersey, M. Davis, H. Patrick, M. Leblanc, K. Koo, C. Askins, M. Putnam, and E. Friebele, "Fiber grating sensors," *J. Lightwave Technol.*, vol. 15, pp. 1442–1463, Aug 1997.

[4] A. Othonos, "Fiber Bragg gratings," *Review of Scientific Instruments*, vol. 68, pp. 4309–4341, Dec 1997.

[5] V. Bhatia and A. M. Vengsarkar, "Optical fiber long-period grating sensors," *Opt. Lett.*, vol. 21, pp. 692–694, May 1996.

[6] S. James and R. Tatam, "Optical fibre long-period grating sensors: characteristics and application," *Measurement Science and Technology*, vol. 14, pp. R49–R61, Jan 2003.

[7] Y. Antman, N. Primerov, J. Sancho, L. Thévenaz, and A. Zadok, "Localized and stationary dynamic gratings via stimulated Brillouin scattering with phase modulated pumps," *Opt. Express*, vol. 20, pp. 7807–7821, Mar 2012.

[8] W. Zou, Z. He, and K. Hotate, "Complete discrimination of strain and temperature using Brillouin frequency shift and birefringence in a polarization-maintaining fiber," *Opt. Express*, vol. 17, pp. 1248–1255, Feb 2009.

[9] Y. Dong, L. Chen, and X. Bao, "High-spatial-resolution time-domain simultaneous strain and temperature sensor using Brillouin scattering and birefringence in a polarization-maintaining fiber," *Photonics Technology Letters, IEEE*, vol. 22, pp. 1364–1366, Sept 2010.

[10] M. K. Barnoski, M. D. Rourke, S. M. Jensen, and R. T. Melville, "Optical time domain reflectometer," *Appl. Opt.*, vol. 16, pp. 2375–2379, Sep 1977.

[11] M. Froggatt and J. Moore, "High-spatial-resolution distributed strain measurement in optical fiber with Rayleigh scatter," *Appl. Opt.*, vol. 37, pp. 1735–1740, Apr 1998.

[12] M. Volanthen, H. Geiger, and J. Dakin, "Distributed grating sensors using low-coherence reflectometry," *J. Lightwave Technol.*, vol. 15, pp. 2076–2082, Nov 1997.

[13] T. Kurashima, T. Horiguchi, and M. Tateda, "Distributed-temperature sensing using stimulated Brillouin scattering in optical silica fibers," *Opt. Lett.*, vol. 15, pp. 1038–1040, Sep 1990.

[14] K. Shimizu, T. Horiguchi, Y. Koyamada, and T. Kurashima, "Coherent self-heterodyne Brillouin OTDR for measurement of Brillouin frequency shift distribution in optical fibers," *J. Lightwave Technol.*, vol. 12, pp. 730–736, May 1994.

Chapter 2

Time-frequency domain analysis for long fiber Bragg grating sensing applications

2.1 Introduction

As previously mentioned in the introduction, fiber optic devices and components are used in various applications and due to their advantageous characteristics (small size, light weight, low cost, chemical inertia, non conductivity, among others), fiber optics are suitable for remote, long distance and harsh environment measurements [1].

Recently, distributed optical fiber sensors have attracted growing interest in sensor technology as they present the key advantage that the entire optical fiber itself can be turned into a linear sensing element. Distributed fiber optic sensors are implemented by analyzing back-reflected light that occurs uniformly along the fiber. Those methods, based on elastic optical effects (Rayleigh) [2] or inelastic optical effects (Brillouin and Raman) of the back-scattered light, enable strain, temperature and vibration sensing over long range with relative fine spatial resolution [3, 4].

On the other hand, fiber Bragg gratings (FBGs) based devices have been playing a key role in sensing area applications owing to their fast response, high sensitivity, distributed and multiplexing capability of measuring different kinds of physical and mechanical parameters [5]. Furthermore, FBG sensors present some crucial advantages when compared to methods based on elastic/inelastic scattering.

As described in the previous chapter, a FBG is an optical component characterized by a periodic or aperiodic perturbation of the effective refractive index in the core of an optical fiber, which is permanently photo-induced by optical absorption of ultraviolet (UV) light. By means of the so-called *coupled-mode theory* [6], the reflectivity of a uniform FBG with constant index modulation and period, as a function of the grating length L and wavelength λ can be expressed as

$$R(L,\lambda) = \frac{\kappa^2 \sinh^2(\gamma L)}{\Delta\beta^2 \sinh^2(\gamma L) + \gamma^2 \cosh^2(\gamma L)} \tag{2.1}$$

being κ the coupling coefficient, $\beta = 2\pi n_0/\lambda$ the propagation constant, n_0 the average refractive index, $\Delta\beta = \beta - \pi/\Lambda$ the wave-vector detuning, Λ the grating period and $\gamma^2 = \kappa^2 - \Delta\beta^2$. For light at the Bragg grating center wavelength λ_B, there is no wave-vector detuning, i.e. $\Delta\beta = 0$, then the reflectivity becomes [6]

$$R_{max}(L,\lambda) = \tanh^2(\kappa L). \tag{2.2}$$

Fundamentally, a FBG does not isotropically radiate the light from the activating pulse like in a scattering process, but returns it unidirectionally back into the fiber like a partial reflector [7]. This multiplies the efficiency of the process, with the consequence that the systems employed to interrogate FBG sensors do not require very high pump power to be launched in the sensing fiber, avoiding therefore the onset of non-linear effects which may negatively affect the measurements. This also results in very simple and cost-effective interrogation systems with comfortable signal-to-noise ratios (SNRs). However, FBG sensors normally only supply information at discrete points; for this reason, FBGs-based devices have been largely employed to perform highly sensitive discrete point sensing. Nevertheless, a substantial added value is offered by fully distributed sensing, in which the entire length of the fiber generates information.

Preliminary proposals have been demonstrated to characterize the Bragg frequency distribution along a FBG, in order to realize distributed temperature/strain sensors. In this scenario, the optical low-coherence reflectometry (OLCR) technique [8] has demonstrated very good performance in terms of spatial resolution. However, the OLCR scheme presents a limited measurement range and a slow response time. Another approach is based on the synthesis of optical coherence function (SOCF) [9], which allows a point-by-point characterization of the grating properties by simply tuning the modulation frequency of the optical source. Anyway, this technique requires a very complicated setup and expensive devices.

A third alternative for distributed measurements along optical fibers has been proposed based on optical frequency domain reflectometry (OFDR) [2]. This approach enables temperature and strain measurements over long ranges with very good performance in terms of spatial resolution and precision. This performance has been obtained by combining OFDR with an advance cross-correlation based method. Indeed, strain and temperature changes have been detected by calculating local changes on optical path from cross-correlation functions. Also, the technique comprises a sophisticated post processing scheme and an auxiliary interferometer used to avoid any non-linearity. Moreover, the systems results polarization-dependent, thus requiring a polarization beam splitter and two photo-detectors (PDs) to mitigate any signal fading. Subsequently, fiber distributed sensing based on very-weak reflectivity FBG has also been demonstrated using optical time-domain reflectometry (OTDR) [10, 11]. By scanning the laser frequency a distribution map of the reflectivity along the fiber has been obtained, demonstrating very good performance in terms of accuracy and signal response.

In this chapter, a simple scheme to measure the distribution of the central frequency along different kinds of FBG-based sensors is proposed and experimentally demonstrated, based on time-frequency domain analysis. The measurement system is essentially based on a combination of frequency scanning of the interrogating optical pulse and OTDR technique [12]. A short optical pulse is employed with the purpose to perform the time-frequency domain analysis of the Bragg-frequency distribution. The signal back-reflected from the grating is scanned by means of an oscilloscope. This way, by controlling the central frequency of the incident pulse, a time-resolved interrogation of spectral profiles of the FBG-based sensors is obtained. The measurements here reported, clearly demonstrate that such a methodology can offer an attractive and potentially cost-effective solution for distributed fiber optic sensing.

2.2 Principle of operation

As above commented, the operation principle to analyze the spectral properties of different FBG-based sensors relays on OTDR technique. In particular, in the first part of the chapter, the time-frequency domain analysis of a high reflectivity FBG is presented, with the purpose to demonstrate its feasibility as quasi-distributed fiber optic sensor. Afterwards, the interrogation of an ultra weak FBGs network is demonstrated for spot events detection. For a start, theoretical simulations have been performed with the aim of studying the interaction between a short broadband optical pulse and fiber gratings having different values of reflectivity. In practice, the grating reflectivity can be suitably tailored by controlling the ultraviolet exposure time during the fabrication process. The theoretical analysis of linear pulse propagation through uniform FBGs for the case in which the input pulse spectrum is broader than that of the grating response, was already investigated [13, 14]. According to the mathematical modeling point of view, the reflected pulse from the grating is the inverse Fourier transform (IFT) of the

product between the input Gaussian pulse spectrum and the grating reflection response. In our simulations, a symmetric 2 ps Gaussian pulse is assumed as ultra short input signal; Fig. 2.1 shows theoretical simulations of such pulse propagation through a uniform 1 cm-long grating for different values of the reflectivity, ≈ 99% (Fig. 2.1(a)) and ≈ 0.1% (Fig. 2.1(b)).

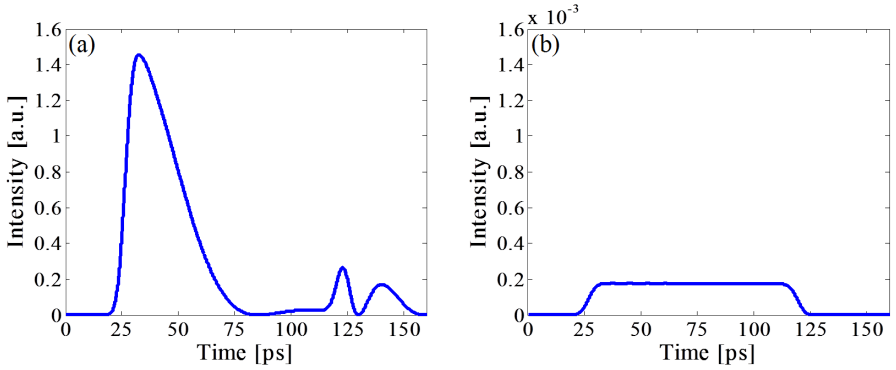

Figure 2.1: Reflected pulse from uniform FBGs having length of 1 cm and different reflectivities: (a) ≈ 99% (grating strength: 2 x 10^{-4}). (b) ≈ 0.1% (grating strength: 1.58 x 10^{-6}). The incident pulse is a 2 ps Gaussian pulse.

The theoretical analysis and the simulations performed clearly show as, in the case of a high reflectivity FBG the incident pulse is almost completely back-reflected at the beginning of the grating, as schematically illustrated in Fig. 2.2(a). If an external perturbation (i.e. strain or temperature change) is induced in any part of the grating, a change in the physical characteristics (i.e. refractive index and period) of this section of the FBG is expected, which causes, in turn, a Bragg wavelength shift. Indeed, it can be considered to have another secondary gratings centered at a new Bragg wavelength. In this case, when the input optical pulse is coupled into the FBG, a separation of the reflected pulse into two distinct components can be observed. A main reflection pulse will be reflected in the initial section of the FBG, and a transient sub-pulse will be reflected at the beginning of the "new" FBG (i. e. the portion under external perturbation), as schematically shown in Fig. 2.2(b). This is actually because an ultra short optical pulse presents a very broad spectrum [10] and hence an amount of the signal power at the new Bragg wavelength (i.e those of the zone under perturbation) is back-reflected beside the main reflection pulse, as it will be further explained afterwards. The main reflection pulse and the sub-pulse are separated in time by the round-trip propagation time between the initial part of the sensing FBG and the section where the perturbation is located. By evaluating the time separation between the two peaks, the position of the grating local perturbation can be detected.

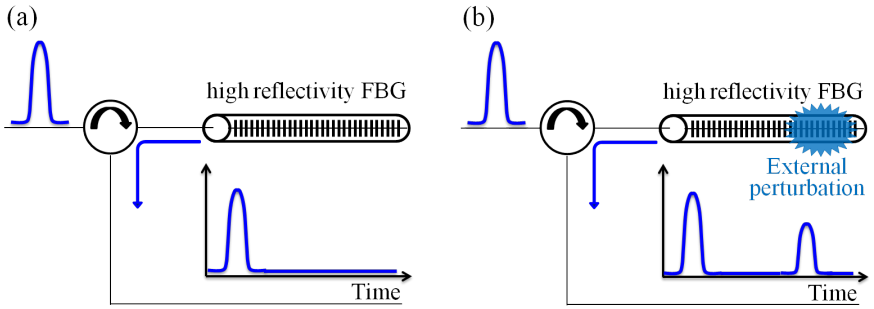

Figure 2.2: Operation principle to interrogate the 10 cm-long high reflectivity FBG by using an ultra short optical pulse. (a) Due to the high reflectivity of the grating, the input pulse is almost totally back-reflected at the beginning of the grating. (b) When a perturbation is provoked along the FBG, a transient sub-pulse is reflected by the grating portion under the external perturbation.

In case of high reflectivity FBG, it is no possible to discriminate two perturbations having the same magnitude (in terms of temperature or strain), due to the high reflectivity of the grating, which impedes the detection of the second events. On the contrary, two ore more events having different magnitudes can be retrieved, as schematically shown in Fig. 2.3(a). In order to rid out this limitation, a very weak FBG-based device can be applied as sensing element. In this case, the incident pulse at Bragg wavelength is continuously back-reflected while propagating through the entire grating length, as demonstrated in the theoretical simulations detailed above (see Fig. 2.1(b)). This fact makes the detection of several perturbations possible, even if they are at the same temperature (or at the same strain level), as illustrated in Fig. 2.3(b).

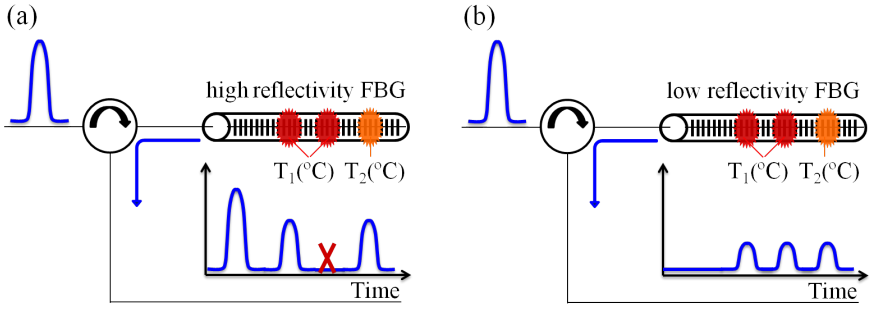

Figure 2.3: Schematic representing the interrogation of gratings having different reflectivities. (a) In case of high reflectivity FBG, only perturbations having different magnitudes can be detected. (b) In case of low reflectivity FBG, several external perturbations can be localized even if they have the same magnitude.

2.3 Fiber optic sensors using a 10 cm-long high reflectivity FBG

In this section, the time-frequency domain analysis along a 10 cm-long grating having reflectivity of $\approx 99\%$ is presented and demonstrated, with the purpose to realize quasi-distributed fiber optic sensors. In particular, a liquid level sensor and a temperature gradient sensor are proposed and developed.

2.3.1 Liquid level sensor

Liquid level sensing is an indispensable requirement in many applications in which monitoring of the volume of the liquid is necessary, for example in chemical processing, fuel storage and transportation. Electrical liquid level sensors are widely used in practice, but their applicability, reliability, and safety is compromised if the liquid to be monitored is conductive or corrosive or if the environment is potentially explosive. Moreover, in case of multiple sensors, an electrical liquid level sensing system requires intensive cabling and feed-through, unavoidably increasing the system cost and complexity.

Optical fiber liquid level sensors offer many advantages under these rigorous conditions because they are made of dielectric material and thus they are no-conducting and anti-corrosive. Besides, another important characteristic of fiber optic sensors is their multiplexing capability, which enables one to use a shared light source and detection system for multipoint measurement, thanks to various fiber optic components developed for communications [1].

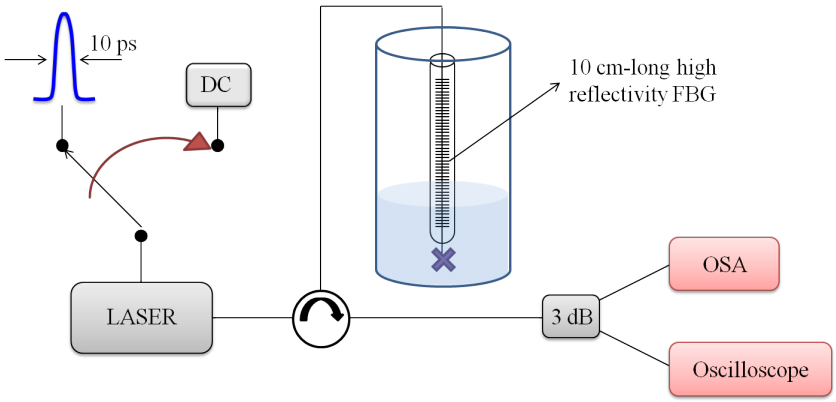

Figure 2.4: Experimental layout to interrogate the 10 cm-long uniform grating.

Different kinds of fiber optic liquid level sensing devices and techniques have been reported. For instance, liquid level measurements have been performed using a FBG suitably etched in order to enhance the sensitivity to the liquid refractive index [15] or by using mechanical components that are able to induce expansion or compression in the fiber which in turn induces change in transmission or reflection response [16]. Other types of fiber optic liquid level sensors has been proposed based on multimode interference (MMI) effects along a no-core multimode fiber (MMF) [17], on high-birefringence fiber loop mirror (HBFLM) [18], and on plastic optical fiber (POF) [19], amongst others.

Here a fiber optic liquid level sensor based on a 10 cm-long high reflectivity FBG is presented and experimentally validated. The schematic diagram used to perform the liquid level measurements is illustrated in Fig. 2.4. A train of 10 ps optical pulses generated by a laser operating at 1554.0 nm is launched into the sensing grating through an optical circulator. The FBG employed during the experiment consists in a 10 cm-long uniform grating mounted inside a graduated container. The Bragg resonance is 1554.0 nm at room temperature, while the reflectivity is $\approx 99\%$ and the full width at half maximum (FWHM) is ≈ 14 GHz. The back-reflected signal is captured and monitored by means of an oscilloscope and an optical spectrum analyzer (OSA). The incident pulse spectral width is much shorter than the transit time along the grating, with can be calculated according to

$$T_{trans} = \frac{2n_g L_{FBG}}{c} \tag{2.3}$$

where n_g is the group refractive index of the fiber and c is the speed of light in vacuum. Being the length of the FBG, $L_{FBG} = 10$ cm, by using (2.3) the transit time of the input pulse along the entire grating length (backwards and forwards) is estimated to be of almost 1 ns, resulting much longer than the incident pulse duration. The input pulse train has 2 ns repetition rate, which is equivalent to a twice the round-trip propagation time through the grating. In this way, it is ensured that only one pulse travels along the FBG and any reflection overlapping between adjacent pulses is avoided.

As already commented, when the short optical pulse is launched into the FBG, it is almost completely back-reflected in the initial section of the grating, due to the high reflectivity of the sensing FBG. However, when the 10 cm-long uniform FBG is partially immersed within the liquid having temperature different than that of the surrounding ambient, the structure and properties of the perturbed section of the grating change. This local change induces, in turn, a local Bragg wavelength shift. Indeed, it can be considered to have two separate gratings; the first one centered at the Bragg wavelength of the original FBG (i.e. 1554.0 nm) and the other one centered at a "new" Bragg wavelength. In this case, when the input optical pulse is coupled into the FBG, a separation of the back-reflected

signal into two distinct components can be observed; a main reflection pulse is reflected in the initial section of the original FBG, and a transient sub-pulse will be reflected in the initial section of the new FBG (i. e. the portion of the grating immersed in the liquid). The main reflection pulse and the sub-pulse are temporally separated by the round-trip propagation time between the two different gratings. By evaluating the time-separation between the two peaks, T_{LL}, the liquid level LL can be detected with high spatial resolution, by using

$$LL = L_{FBG} - \frac{T_{LL} \cdot c}{2n_g}. \tag{2.4}$$

Besides, as the incoming signal is always reflected at the beginning of each one of the FBGs [13, 14], the spatial resolution of this technique is essentially determined by half the incident pulse duration, such as any OTDR technique [12]. As the optical interrogating pulse has duration of 10 ps, the spatial resolution of the technique is 1 mm. Experimental liquid level measurements have been performed by step-emptying the container and by recovering the signal back-reflected by the sensor with an oscilloscope, as shown in Fig. 2.5.

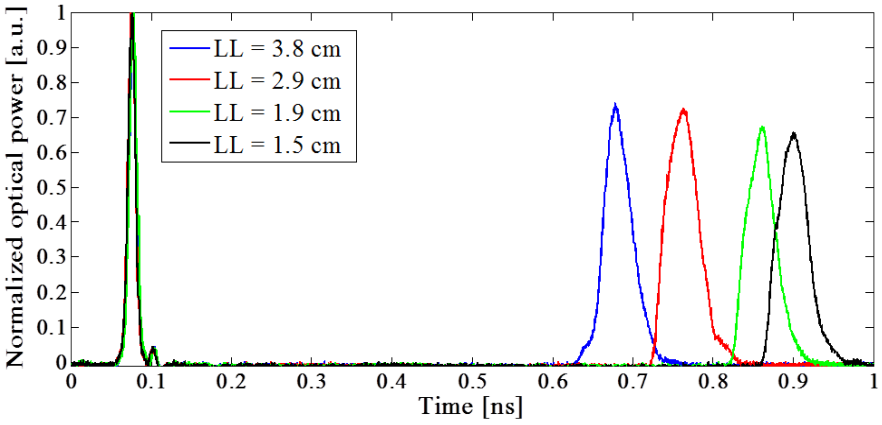

Figure 2.5: Measurements of the back-reflected time waveform obtained by step-emptying the container. The interrogating pulse has temporal width of 10 ps. The main pulse and the sub-pulse are temporally separated by the round-trip propagation time between the initial section of the sensing FBG and the beginning of the FBG section immersed in the liquid.

It is worth mentioning that, during this first experiment, the central frequency of the interrogating pulse is kept constant at the original Bragg resonance of the sensing FBG (i.e. 1554.0 nm). Besides, a Gaussian-shaped optical pulse having temporal width $\tau = 10$ ps, presents a spectral width $\Delta f_p = (2\ln 2/\pi)/\tau \approx 0.441/\tau \approx$ 44.1 GHz (i.e. $\approx$ 355.24 pm) [10]. The wideness of the pulse spectral width makes the detection of the liquid level possible as far as the shifted secondary peak (i.e. the one related to the portion of the FBG immersed in the liquid) is "captured" by the input pulse spectrum. This infers the existence of a maximum limit for the liquid temperature detectable by the sensor. Nevertheless, the temperature measurement range can be certainly extended by reducing the temporal width of the incident pulse (i.e. by enhancing the pulse spectral width) or by performing the measurements by step-wise scanning the central frequency of the incident pulse.

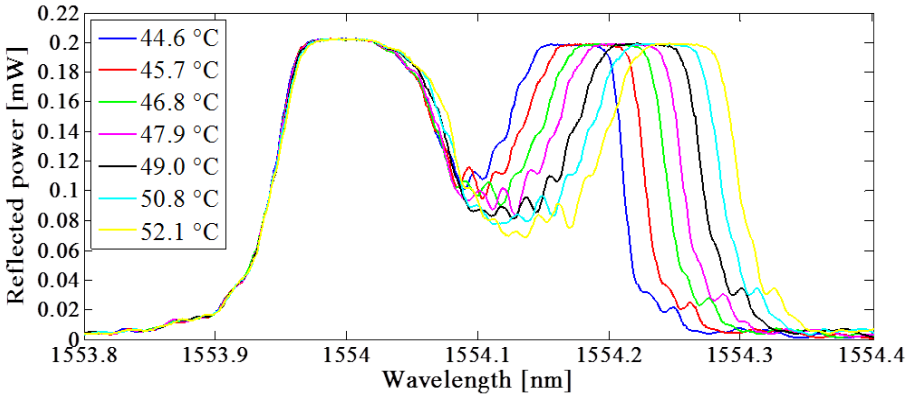

Figure 2.6: Sensing FBG spectra for different liquid temperatures. The inset shows the liquid temperatures.

The temperature of the liquid is calculated by scanning the laser output in direct current (DC) mode and by capturing the back-reflected signal by means of an OSA, as shown in Fig. 2.6. These measurements have been performed by dipping almost half of the FBG within the liquid which temperature is changed during the experiment. The temperature of the liquid has been calculated based on the FBG temperature coefficient which is 10 pm/°C. Finally, it is worth to notice that the minimum detectable temperature basically depends on the FWHM of the sensing FBG. However, this limitation can be overcome by making the sensing fiber response sensitive to the external refractive index, for instance by using an etched FBG, a coated FBG or a long period grating (LPG).

2.3.2 Temperature gradient sensor

Against the backdrop of the positive results achieved for the liquid level sensor, we have investigated the possibility of using the time-frequency domain analysis to perform temperature gradient measurements. The sensor employed is the same 10 cm-long FBG described above when it was applied as liquid level sensor. Fig. 2.7 shows the schematic interrogation layout which is actually similar to that of Fig. 2.4, with the important difference that now the temperature measurements are obtained by the progressive scanning of the tunable laser source. This permits the elimination of the OSA from the layout, dramatically simplifying the measurement scheme and reducing the cost of the method. Once again, a 10 ps optical pulse (having duration much shorter than the transit time through the FBG) is launched into the sensing grating and the back-reflected signal is analyzed via an oscilloscope. After the grating end a piece of single mode fiber (SMF) having length of 1 cm is placed. The end facet of this SMF is left open in the air to provide a reflection signal that will be used as a reference point. It is worth pointing out that, even if the temperature gradient were placed at the end of the grating, the measure of its position will not be adversely affected. In fact, by using (2.3) the transit time in 1 cm-long SMF is calculated to be ≈ 97.101 ps, resulting an order of magnitude bigger than the interrogating pulse duration.

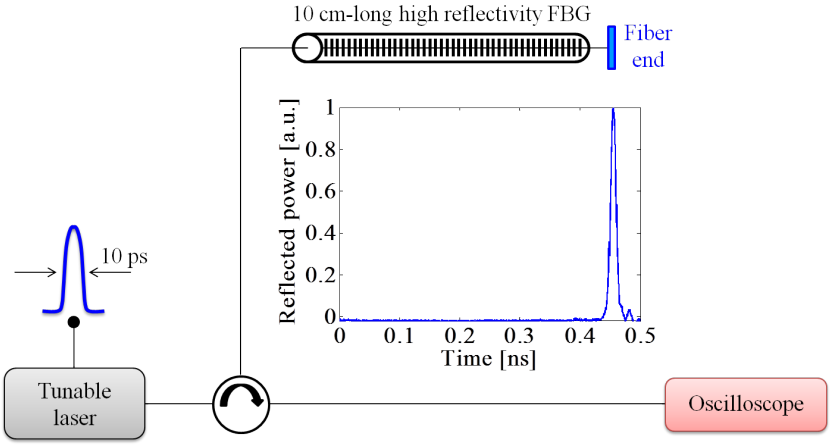

Figure 2.7: Schematic diagram for interrogating the 10 cm-long uniform FBG applied as temperature gradient sensor. Inset: measurement of the reflected pulse time waveform when the incident pulse has a wavelength different from the FBG resonance. The incident pulse is back-reflected at the end of the fiber.

The wavelength of the tunable laser used to perform the measurements has been previously calibrated in temperature; so as, by simply adjusting the thermistor resistance controlling the device temperature, the wavelength of the laser can be easily tuned. This way, with the purpose to measure the distribution of the grating spectral properties, the central frequency of the interrogating pulse is precisely controlled by the injection current applied to the laser. The configuration proposed for the temperature gradient measurements is based on the interrogation of the central frequency distribution of the FBG based on time-frequency analysis. When the incident pulse wavelength is far from the Bragg wavelength, at the oscilloscope only the signal related to the reflection at the end of the SMF will be retrieved, as illustrated in the inset of Fig. 2.7.

Hereafter, when a hot zone is provoked along the sensing FBG, a temperature gradient is obtained. This local change of temperature will produce a local Bragg frequency shift. When this occurs, besides the signal reflected at the end of the fiber, a second reflected signal is produced (due to the refractive index changes provoked by the heating) at the point where the hot zone is located, schematically depicted in Fig. 2.8(a). Now, by performing a step-wise scan of the central frequency of the interrogating pulse, the temperature shifts can be detected. As mentioned before, the signal reflected at the end of the grating is used as reference point in order to obtain the exact position and distribution of the hot zone along the sensing FBG. In fact, the distance L_{grad} between the different temperature zones and the end of the fiber is calculated by evaluating the time separation T_{grad} between the reference pulse and the time waveform provoked by the hot zone according to

$$L_{grad} = \frac{T_{grad} \cdot c}{2n_g}. \tag{2.5}$$

This is actually the same equation as (2.3). In this way, the temperature gradient and its distribution along the 10 cm-long grating are calculated.

Fig. 2.8(b) shows the distribution of the different temperature zones as well as their position along the grating. The hot zone has a minimum temperature shift of 52°C (see red curve in Fig. 2.8(b)) and a width of $\approx$ 1 cm. Since the interrogating pulse wavelength is progressively increased, the width of the pulse reflected at the hot zone is gradually reduced. This fact means that the heated surface presents its highest temperature in its middle point. In fact, when the tunable laser resistance is set in order to perform an interrogating pulse central wavelength of 1554.89 nm, a temperature of 89°C above the room temperature is detected. This temperature corresponds to the hottest point which is located in the midst of the hot zone. Fig. 2.8(c) schematically illustrates the characterization of the different heated zones and their positions along the sensing grating.

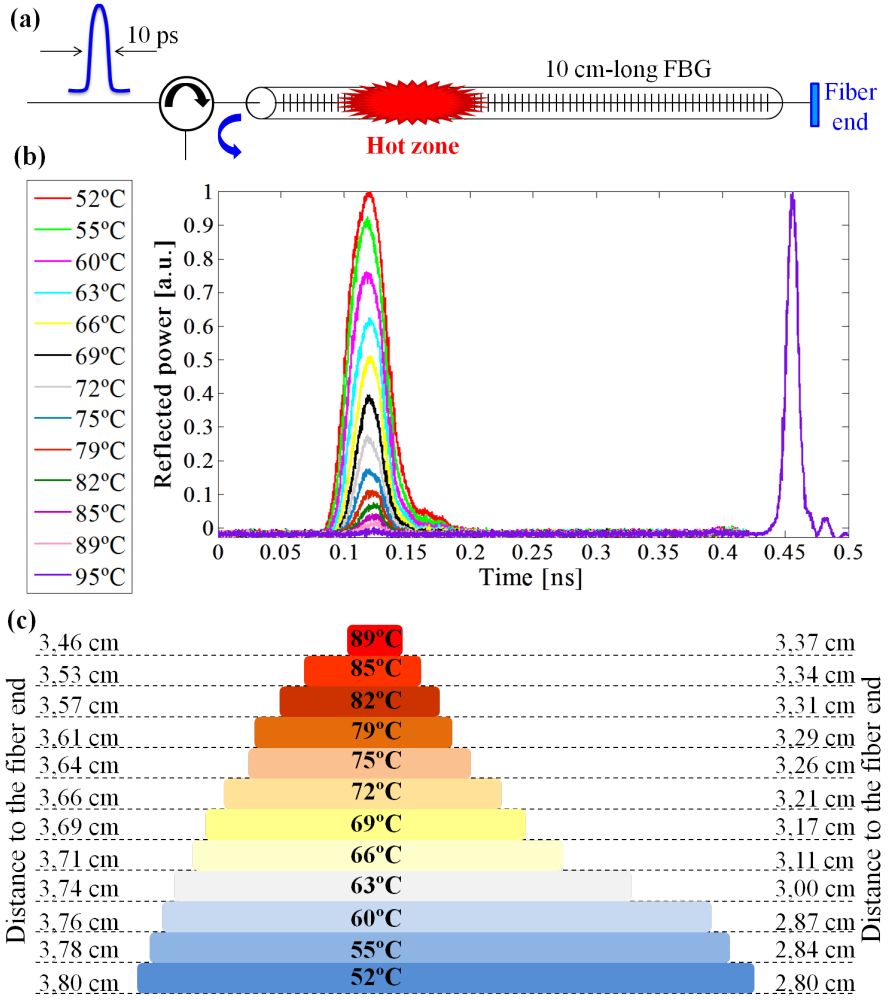

Figure 2.8: (a) Schematic detail of the FBG-based temperature gradient sensor. (b) Measurements of the reflected pulse time waveforms as a function of the laser emission wavelength. The text-box shows the increment in temperature. (c) Characterization of the heated zone in the sensing grating. The distance of the hot zone to the end of the fiber is indicated.

As commented for the liquid level sensor, the spatial resolution of this technique is essentially determined by half the pulse duration, such as as any OTDR technique [12]. Hence, since the optical interrogating pulse has duration of 10 ps, the proposed configuration presents a 1 mm spatial resolution. The temperature distribution along the sensing FBG has been calculated according to the fact that for the sensing grating employed, 10 pm shift in Bragg wavelength correspond to

1°C shift in temperature. It is worth mentioning that, since the laser wavelength calibration has been performed with an accuracy of less than 5 pm, the temperature gradient measurements have been carried out with an estimated accuracy of less than 0.5°C.

The measurements performed simply indicate the potential of the method in term of spatial resolution and measurement range, which are certainly attractive in some research areas such as micromechanics, bio and chemical fields, among others. Nevertheless, both these values can be further enhanced by using a shorter interrogating pulse (as far as the spatial resolution is concerned), and by fabricating a longer FBG (as far as the measurement range is regarded).

2.4 Spot event detection along a large scale sensor based on ultra weak FBGs

In the previous section two kinds of fiber optic sensors based on a 10 cm-long high reflectivity FBG have been demonstrated. In the midst of the results achieved so far, we have investigated the possibility to realize a long range FBG-based sensor. However, for a large scale FBG sensor network, ultra weak gratings are required, which ensures a low crosstalk level among elements in the array. On the other hand, the fabrication of a very long, continuous and homogenous FBG with no phase hopping and with very low reflectivity is an expensive and complicated issue, with a maximum reported length of 1 m [20]. The possibility of using weak reflectors written in cascade along a single optical fiber for sensing applications has attracted the interest of some research groups. For instance, in [21] a quasi-distributed fiber optic sensor based on multiple interferometers built from pairs of arbitrary weak reflectors was investigated. Inspired by the operation principle of microwave photonics (MWP) filters, Huang et al. proposed an optical carrier based microwave interferometry scheme for sensing application, demonstrating high signal quality and polarization-insensitive measurements. However, the method requires a weighty post-processing analysis including a complex and inverse Fourier transform (IFT) of the microwave spectrum, a time-gating to the time-domain signal and hence a Fourier transform (FT) of the gated signal to obtain the final microwave interferogram. Besides, an interrogation scheme based on time-division multiplexing (TDM) technique for large range sensing based on an array of identical ultra weak FBGs was demonstrated [22, 23]. A network of 843 serial FBGs with 2 m equidistance between two adjacent gratings was interrogated by using a 20 ns pulse, demonstrating the feasibility to integrate several hundreds of FBGs in a single optical fiber for sensing application. Anyway, this configuration presents a huge dark zone between consecutive sensing elements (2 m), hence, as a non-distributed sensing scheme, the system can only monitor and detect events at the positions where the FBGs are located.

In this section, we report a versatile long range sensing network based on 500 identical ultra weak FBGs (reflectivity $\approx 0.1\%$), written in cascade and covering 5 m of optical fiber. The sensing gratings are 9 mm-long and are spaced by $\approx$ 1 mm, as schematically depicted in Fig. 2.9. The FBG cascade fiber was kindly provided by FBGS International [24], which fabricates optical fibers by using draw tower gratings (DTGs) technology. This technique combines the drawing of the optical fiber with the writing of the grating. During the production process a glass pre-form is heated and then the pulling and formation of the fiber is initiated. The FBG cascade sensor is continuously written using a pulsed excimer laser during the fiber drawing process. Pulse repetition rate is synchronized with the drawing speed in order to obtain an equal spacing between consecutive FBGs. This automated production process results in very high quality, accurately positioned FBGs which allows controlling the production parameters very accurately, thus assuring high repeatability and grating uniformity. Since FBG writing is previous to coating, the fiber could be rolled up in a compact coil of around 10 cm diameter.

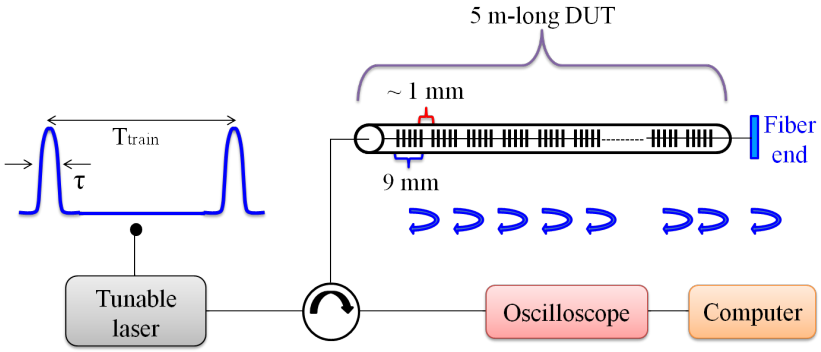

Figure 2.9: Experimentally layout to interrogate the 5 m-long photonic sensor composed of 500 identical ultra weak FBGs. A time-frequency domain analysis is performed enabling the detection of spot events along the sensor.

The most common approach to interrogate a FBG cascade sensor is to use optical pulses much shorter than the transit time of the light through two consecutive sensing elements [22, 23]. In this way, it is ensured that the optical pulse travelling along the FBGs chain one grating at the time, leads to no overlapping between back-scattered signals coming from adjacent FBGs. This allows stable and fluctuation-free time waveforms to be detected at the oscilloscope. In contrast, the measurements reported here show the possibility to interrogate a weak FBG cascade sensor using optical pulses having duration longer than the transit time through consecutive FBGs. Under these conditions, the input pulse will cover several gratings at one time; hence giving rise to coherent effects during the measurement process. Despite the presence of these coherent interferences, the

detection of the position and length of spot events along the sensor is demonstrated with good performance in terms of measurand resolution.

2.4.1 Experimental measurements and results

The experimental layout used to interrogate the weak FBG cascade sensor, which is similar to the schemes described in the previous section, is illustrated in Fig. 2.9. The output of a tunable laser source is shaped as a pulse train with a repetition rate T_{train} chosen to be longer than the transit time of the light through the sensing device. This way, it is secured that a single pulse is present along the entire length of the 5 m-long sensor, preventing crosstalk between adjacent pulses. As a result, a Gaussian-shaped optical pulse having temporal duration τ is launched into the device under test (DUT) through an optical circulator. Finally, the back-reflected signal from the DUT is acquired by an oscilloscope and analyzed via a computer. The other end of the DUT is left open in the air to provide a reflection signal that will be used as a reference point to localize the position of the spot event along the FBG-based cascade sensor. When the input pulse is launched into the photonics sensor composed of low reflectivity FBGs, it is continuously back-reflected while propagating through the entire DUT length. By controlling the central wavelength of the incident pulse, the detection of spot events can be achieved, with a spatial resolution dictated by half the input pulse duration, like any OTDR technique [10].

Firstly, the signal used to characterize the Bragg frequency distribution of the FBG cascade sensor is a train of 500 ps-long optical pulses with a repetition rate of 64 ns. As the DUT is 5 m-long, the round-trip time of the light over its length is around 50 ns. The pulse rate repetition $T_{train} = 64$ ns ensures the absence of overlapping between back-reflected signals from successive incident pulses. It is worth mentioning that the pulse temporal duration $\tau = 500$ ps is almost equivalent to the transit time through 10 weak FBGs of the array, since the separation between two consecutive 9 mm-long gratings is ≈ 1 mm. It is expected that this will produce two undesirable side effects: waveform instability and intensity fluctuations. However, as far as the first issue is concerned, initial measurements have revealed a slight instability of the traces recovered by the oscilloscope; this problem is easily overcome by averaging 20 repeated traces, allowing clear and stable measurement waveforms. On the other hand, intensity fluctuations of the time waveform due to random phase hops between adjacent gratings have been observed, causing the rising of dead zones in the reflected signal. Nevertheless, in our experiments, the length and position of the spot event can be measured starting by its time waveform duration, which is the difference between the final instant and the initial one, as will be detailed afterwards. The intensity fluctuations of the time waveform, however, only affects the inner zone between the rise and fall slopes, while the two transition sides of the time-waveform (i.e. rise and fall slopes) remain unchanged. This infers that, despite the presence of these dead zones in

the time domain traces, it does not impede the measurements of the position and length of the spot events.

The time response of the sensor when the central frequency of the tunable laser matches the DUT Bragg frequency and the aforementioned train of pulses is launched into the sensing device is shown in Fig. 2.10(a). Due to the weak reflectivity of the 500 FBGs contained in the DUT, a small fraction of the signal pulse experiences a back-reflection along the entire length of the sensor during the propagation. Hence, once again, the length L_{DUT} of the sensing array is encoded in the reflected waveform duration T_{DUT}, according to (2.5).

Then a hot zone is created by dipping a section of the DUT in a hot bath whose temperature is measured with a reference thermometer and is kept constant using a hot plate. This local change of temperature produces a local Bragg frequency shift. Now, the tunable laser is step-wise scanned and for each wavelength the time waveform is acquired by the oscilloscope and stored by the computer. At this point, the integrated intensity is calculated for each time-waveform, by simply summing up all the reflective intensity contributions. This is a very easy and cost-effective procedure as it only requires the sum of all the intensity samples avoiding sophisticated and time consuming post-processing techniques such as cross-correlation based methods. Clearly, the higher value of the integrated intensity corresponds to the waveform relevant to the laser wavelength which matches the original Bragg wavelength of the 5 m-long sensing device. Starting from this wavelength and gradually incrementing this value, a progressive reduction of the integrated intensity is observed. But, when the wavelength of the interrogating pulse is moved closer to that of the hot zone, the integrated intensity starts to rise as long as it reaches a maximum value, before decreasing again. When the maximum value is reached, the input pulse wavelength is matching the Bragg wavelength of the hot spot. The corresponding time-waveform is illustrated in Fig. 2.10(b), which also shows how the random effects make arbitrary changes in back-reflected intensity, causing the rising of dead zones in the reflected signal. Nevertheless, as previously mentioned, the presence of these dead zones does not impede the measurements of both position and length of the hot spot, as following. The reflection at time $t = 18$ ns is the one delivered by the end facet of the DUT, used as a reference point. By evaluating the time duration of the hot spot waveform T_{HS1}, and by using (2.5), the length of the spot event is measured to be $L_{HS1} = 55$ cm. Similarly, the position of the heated zone along the sensor is calculated by evaluating the time separation between the reference pulse and the time-waveform relative to the hot spot, according to (2.5). So, the middle point of the hot spot is calculated to be 132 cm from the end facet of the fiber. At a given wavelength of the interrogating pulse, the back-reflected signal is collected; as this operation is repeated by step-wise scanning the central wavelength of the incident pulse, the 3D map representing the distributed reflection spectrum is obtained, as shown in Fig. 2.10(c).

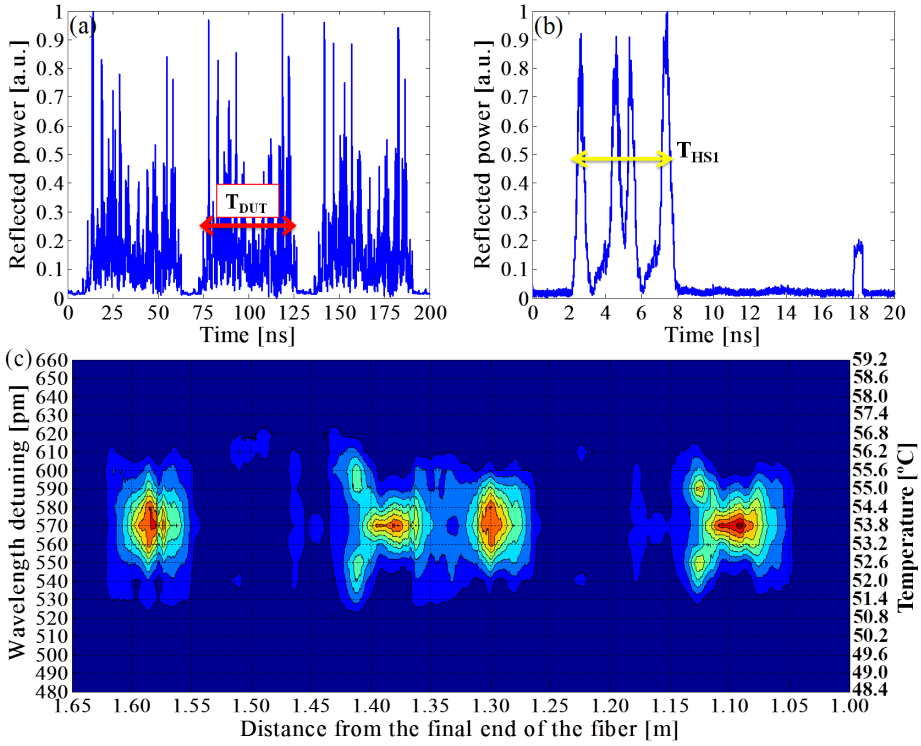

Figure 2.10: Measurement set for an input pulse width of 500 ps. (a) Measured time response of the DUT. Each waveform has duration of 50 ns corresponding to the round-trip time through the 5 m-long fiber sensor. (b) Measured time response of the hot spot created along the DUT. The reflection at time $t = 18$ ns is the one delivered by the end facet of the DUT, used as a reference point.(c) 3D distribution map of the back-reflected signal obtained by progressively scanning the central wavelength of the input pulse.

Another set of measurements has been performed by using a shorter interrogating pulse, showing a temporal width of $\tau = 80$ ps, following the same methodology as previously described. The purpose of this second experiment is to prove that a shorter input pulse may reduce the intensity fluctuations and therefore the presence of dead zones in the reflected signal. Once again a hot spot is applied at a certain point of the sensor and the step wise scanned procedure is repeated. Fig. 2.11(a) shows the time-waveform corresponding to the laser wavelength which matches the Bragg wavelength of the hot zone. The reflection at time $t = 4.8$ ns is the one provided by the end facet of the DUT. By evaluating the time duration of the hot spot waveform T_{HS2}, the length of the spot event is measured to be $L_{HS2} = 35$ cm. Moreover, the middle point of the hot spot is calculated to be 29 cm from the end facet of the fiber. The distributed reflection 3D map is obtained by scanning step-by-step the central wavelength of the interrogating pulse and is

illustrated in Fig. 2.11(b). Here it can be seen that using a shorter interrogating pulse the presence of dead zones in the intensity trace is dramatically reduced. This means that by interrogating the sensor with an appropriately short pulse the intensity fluctuation effects can be suppressed, leading to no dead zones in the measurement of back-reflected signals. In a similar way, the intensity ripples (and hence the dead zones) can be suppressed by using a FBGs cascade device having enough separation between each neighboring sensing element, though presenting insensitive sections.

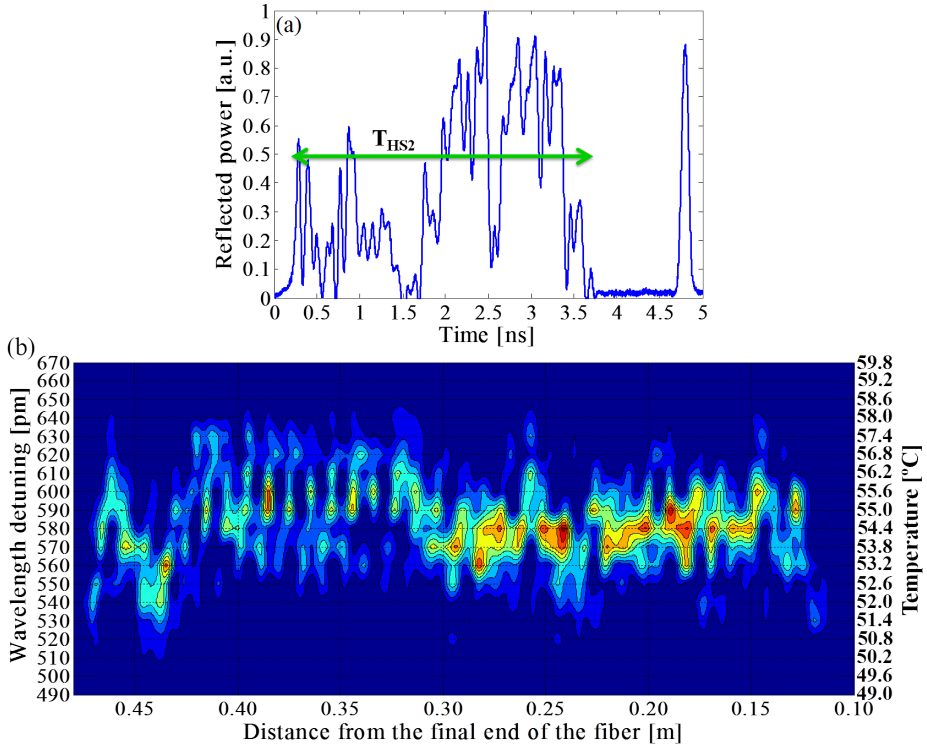

Figure 2.11: Measurement set for an input pulse width of 80 ps. (a) Measured time response of the hot spot provoked along the DUT. The reflection at time $t = 4.8$ ns is the one delivered by the end facet of the DUT, used as a reference point.(b) 3D distribution map of the back-reflected signal obtained by progressively scanning the central wavelength of the input pulse.

2.4.2 Sensor performances

In the following discussion, the performance that the proposed sensor presents in the measurement of the hot spot length, position and temperature are detailed.

- **Temperature analysis**
  The Bragg wavelength of the sensing device has been precisely measured at 20.0°C room temperature when neither strain nor temperature changes have been applied on the device. In this condition, the Bragg wavelength of the DUT has been calculated to be 1549.857 nm. Also temperature measurements have been performed several times in order to narrowly define the thermal coefficient of the fiber. The measurements performed have been achieved by scanning the central wavelength of the interrogating pulse by 10 pm increments. Based on the fiber temperature coefficient, which is 16.855 pm/°C, the temperature accuracy of the method is estimated to be better than 0.6°C. This is just a rough and safe approximation of the precision of the proposed method which can actually be improved by implementing standard fitting of the acquired data [25]. The temperature of the hot spot can be calculated by the wavelength shift between the laser wavelength which matches the Bragg wavelength of the hot zone and the original Bragg wavelength of the DUT. In the case of the 55 cm-long hot spot of Fig. 2.10(b) and Fig. 2.10(c) the wavelength shift has been measured to be 570 pm. By using the temperature coefficient, the measured temperature shift results to be 33.8°C. By adding this value to the room temperature, the temperature of the hot spot is calculated to be 53.8°C. The temperature of the hot bath is measured with a reference instrument to be 53.5°C, giving a temperature error of 0.3°C, which results to be below the value of the estimated accuracy. Temperature measurements have also been performed for the 35 cm-long hot spot of Fig. 2.11. In this case, the measured wavelength shift is 580 pm, leading to a temperature shift of 34.4°C, which in turn gives a calculated hot spot temperature of 54.4°C. The temperature of the hot bath measured by the reference thermometer is 54.2°C, demonstrating a temperature error of 0.2°C, in agreement with the predicted accuracy of 0.6°C.

  Besides, the temperature resolution of the configuration essentially derives from the width of the input pulse spectrum, which in turn depends on the pulse temporal duration τ. In case of Gaussian-shaped pulse, the pulse spectral width Δf is given as $\Delta f = (2\ln 2/\pi)/\tau \approx 0.441/\tau$ [10]. For a 500 ps-long pulse, this leads to a pulse spectral width of 7.056 pm which corresponds to a temperature resolution of less than 0.42°C. Whereas, for τ = 80 ps, the pulse spectral width is 44.1 pm, corresponding to a temperature resolution of less than 2.62°C.

- **Spatial resolution**
  As commented above, the spatial resolution of the method is essentially dictated by half the pulse duration τ, like any OTDR technique. To corroborate this fact, the time waveform reflected by the end facet of the

sensor left open in the air is retrieved and analyzed for different pulse widths $\tau = 500$ ps and $\tau = 80$ ps, as depicted in Fig. 2.12(a) and Fig. 2.12(b), respectively. By using (2.5) the spatial resolution is calculated to be less than 5 cm for a pulse width of 500 ps and it is estimated to be less than 8 mm in the case of a pulse width of 80 ps. The latter is just a theoretical estimation, as the ultimate limit for the spatial resolution is basically dictated by the length of the single sensing element, which is 9 mm. These results provided in these 2 latter sub-sections confirm the clear expected trade-off between spatial resolution and temperature resolution of the proposed method.

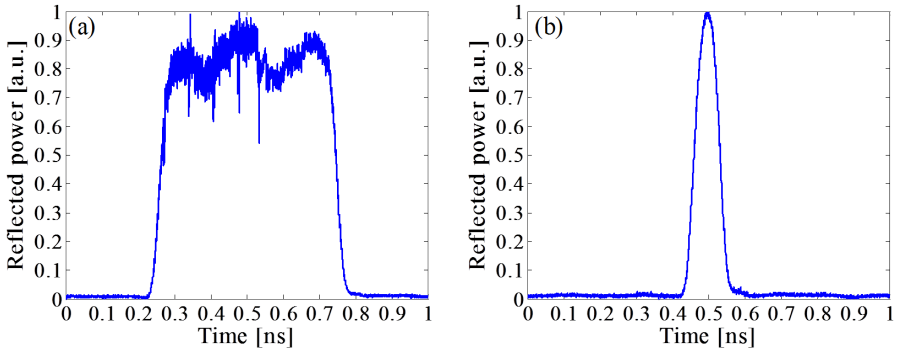

Figure 2.12: Measured reflection signal provided by the end facet of the FBG cascade fiber sensor for different widths of the interrogating pulse. (a) 500 ps. (b) 80 ps.

- **Length and position calculation**
  The length of the spot has been measured by estimating its time waveform duration, which is the difference between the final instant and the initial one. In case of "ideal" time waveform the rise (fall) slope of the trace would be perfectly vertical and it would take only one value for the starting (ending) instant. It is not the case for the measurements reported here. This is mainly because of the fact that the interrogating signal is a Gaussian-shaped pulse not a rectangular pulse. Fig. 2.13 shows a measured time response for a 2 cm-long hot spot, obtained with a pulse width of 80 ps. The length and the position of the hot spot have been calculated utilizing as initial and ending points those marked with orange stars. These symbols represent the middle points of the rise and the fall edges of the trace. Also, the time values corresponding to the two extremities of both edges have been retrieved: T_a and T_b for the rising edge, T_c and T_d for the falling edge. The error on the evaluations of length and position of the hot spot is estimated, according to

$$Err = \frac{max[L(T_b - T_a), L(T_d - T_c)]}{2} \tag{2.6}$$

where $L(T_b - T_a) = [(T_b - T_a)c]/(2n_g)$ and $L(T_d - T_c) = [(T_d - T_c)c]/(2n_g)$. The factor 2 is associated to the fact that the middle points of the slopes have been used to determine both the length and the position. In this way, the error has been estimated to be less than 5 mm. Similarly, these calculations have been repeated for the measurement set obtained with an input pulse width of 500 ps. In this configuration, the error has been evaluated to be less than 1 cm. This means that a broader interrogating pulse not only increases the spatial resolution but also the error made in measuring the length and the position.

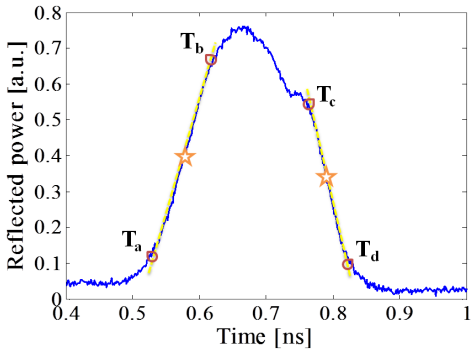

Figure 2.13: Measured time response for a 2 cm-long hot spot, obtained by using an 80 ps incident pulse.

- **Two hot spot sensing**
  The proposed configuration also shows its capability for detecting two spot events even when they have the same temperature. For a large-scale sensor network, very low reflectivity of the sensing units results absolutely necessary, ensuring that the incident signal is continuously back-reflected along the entire DUT length, and therefore allowing the detection of several spot events even if they have the same magnitude. In order to demonstrate this, two different sections of the DUT have been dipped in the hot bath. Fig. 2.14 shows the time-waveform corresponding to the laser wavelength which matches the Bragg wavelength of the hot zones. The reflection at time $t = 8.7$ ns is the one provided by the end facet of the DUT left open in the air. Once again, by using (2.5), the lengths of the spot events are measured to be $L_1 = 5$ cm and $L_2 = 6$ cm, respectively. Moreover, the positions of the heated zones are calculated by evaluating the time separations between the reference pulse and the time-waveforms relating to the hot spots. The initial and the final position of the first hot spot referred to the end-facet of the sensor (see Fig. 2.14) has been evaluated to be $D_1 = 83$ cm, and $D_2 = 78$ cm, respectively. Likewise, the initial and the final positions of the second hot spot referred to the end facet of the sensor have been calculated

to be $D_3 = 51$ cm and $D_4 = 45$ cm, respectively. The measured separation between the two hot spots is $D = 27$ cm.

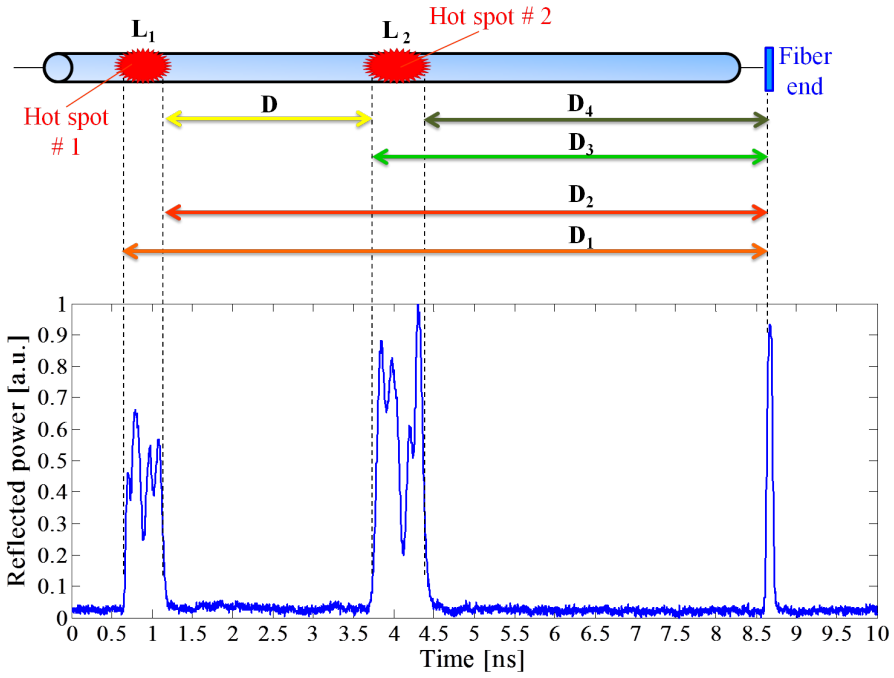

Figure 2.14: Measured time response when two hot spots are provoked along the sensor. The hot spots present different length but same temperature.

2.5 Conclusions

In this chapter, the possibility to measure the local spectral characteristics along FBG-based sensors has been presented and experimentally validated. The measurements have been performed by implementing a time-frequency domain analysis, combining the OTDR technique with the frequency scanning of the interrogating pulse. As a first step, a 10 cm-long high reflectivity FBG has been applied as liquid level sensor. A 10 ps optical pulse, having duration much shorter than the transit time of the light through the sensing grating, has been used as interrogating signal and launched into the sensor. The signal back-reflected from the sensing FBG has been collected and analyzed via an oscilloscope and an OSA. Liquid level and temperature measurements have been performed with a spatial resolution of 1 mm depending on the incident pulse duration, such as any OTDR-based method. Furthermore, the same FBG has been interrogated with a 10 ps optical pulse, with the purpose to detect the presence and the position of a temperature gradient. In this case, measurements have been performed by

the progressively increasing the central wavelength of the incident pulse, without using any additional wavelength scanning devices, such as OSAs. Once again, the method presents a spatial resolution of 1 mm, dictated by the input pulse duration.

Against the backdrop of these positive results, the possibility of realizing a long range FBG-based sensor for spot events detection has been investigated. For a large-scale sensor, ultra weak reflectivity elements are required to let the incident signal propagate along the entire sensing length. However, since the fabrication of a long continuous, ultra weak and homogeneous FBG is an expensive and complicated issue, we have proposed a sensor made of an array of 500 identical ultra weak FBGs written in cascade and covering 5 m of optical fiber. The time waveforms obtained by progressively incrementing the input pulse wavelength and the reflection provided by the end facet of the sensor left open in the air have been used to detect the length and the position of the hot spots located at a certain point of the sensing element. Despite the most common approach to interrogate an ultra weak FBGs sensing network is to use optical pulses much shorter than the transit time of the light through two adjacent sensing units, so avoiding overlapping between back-scattered signals coming from neighboring FBGs, we have demonstrated the possibility of interrogating a large-scale FBG-based sensor using pulses greater than the transit time of the light through consecutive gratings. This alleviates the requirement for ultra short optical pulses and hence reducing the cost and complexity of the interrogation system. Firstly, a 500 ps optical pulse has been employed, giving rise to substantial random coherent effects during the measurement process. Despite the presence of these interferences, which in turn causes dead zones over the acquired traces, the detection of the position and the length of spot events along the sensor has been demonstrated, as a proof-of-concept. In a second set of measurements, an 80 ps optical pulse has been used, in order to demonstrate that a shorter input pulse may reduce the intensity fluctuations and therefore the presence of dead zones in the reflected signal, without negatively affecting the performance of the method in terms of stability, temperature/spatial accuracy and resolution. In particular, the resolution of the system is only dictated by the interrogating pulse duration. It turns out anyway that the dead zones limitation can be only totally overcome by interrogating the sensor with an appropriately short pulse or by using a FBG cascade device having enough separation between neighboring sensing elements. Furthermore, the temperature of the spot event has been calculated with an estimated accuracy of less than 0.6°C, being this value a rough approximation that can certainly be improved by implementing standard fitting techniques. The spatial resolution of the proposed method comes from the interrogating pulse duration which is also responsible for the temperature resolution. In particular, the spatial resolution can be improved by compressing the interrogating pulse at the expense of the temperature resolution. Hence, there is a clear trade-off between these parameters resulting from the time-frequency fundamental duality; this means that the system performance can be controlled and suitably optimized by conveniently choosing the temporal duration of the interrogating pulse. A spatial resolution of 9

mm (ultimately dictated by one FBG length) and a temperature resolution of less than 2.62°C have been obtained with a 80 ps optical pulse; while a 5 cm spatial resolution and a temperature resolution of less than 0.42°C have been demonstrated by using a 500 ps incident pulse. Furthermore, as the measurement range is essentially dictated by the length of the sensor itself, large scale sensing network only requires a longer FBGs array (i.e. by further cascading sensing units) with no need to enhance the bandwidth in the acquisition electronics.

Finally, it is worth noticing that the interrogating method proposed can also be used to implement a crack/strain sensor. Moreover, due to the high sensitivity of the FBG spectrum to temperature and/or strain changes, the system presents great potential for the development of a simple solution for distributed fiber sensing with no need of optical pumping and/or sophisticated controlling systems. The proposed configuration proves to be potentially cost-effective, polarization insensitive, robust against environmental changes and easy to reconfigure. Furthermore, as no ultra-short optical pulses have been employed, the quasi-distributed sensors alleviates the instrumentation complexity and drastically simplifies the measurement scheme as the strength requires for obtaining ultra-short optical pulses is reduced.

Bibliography

[1] B. Culshaw, "Optical fiber sensor technologies: opportunities and-perhaps-pitfalls," *J. Lightwave Technol.*, vol. 22, pp. 39–50, Jan 2004.

[2] M. Froggatt and J. Moore, "High-spatial-resolution distributed strain measurement in optical fiber with Rayleigh scatter," *Appl. Opt.*, vol. 37, pp. 1735–1740, Apr 1998.

[3] A. Rogers, "Distributed optical-fibre sensing," *Measurement Science and Technology*, vol. 10, pp. R75–R99, Aug 1999.

[4] X. Bao and L. Chen, "Recent progress in distributed fiber optic sensors," *Sensors*, vol. 12, p. 8601, Jun 2012.

[5] A. Kersey, M. Davis, H. Patrick, M. Leblanc, K. Koo, C. Askins, M. Putnam, and E. Friebele, "Fiber grating sensors," *J. Lightwave Technol.*, vol. 15, pp. 1442–1463, Aug 1997.

[6] T. Erdogan, "Fiber grating spectra," *J. Lightwave Technol.*, vol. 15, pp. 1277–1294, Aug 1997.

[7] L. Thévenaz, "Next generation of optical fibre sensors: new concepts and perspectives," in *Proc. SPIE*, vol. 9157, pp. 9157AN–9157AN–4, Jun 2014.

[8] M. Volanthen, H. Geiger, and J. Dakin, "Distributed grating sensors using low-coherence reflectometry," *J. Lightwave Technol.*, vol. 15, pp. 2076–2082, Nov 1997.

[9] K. Hotate and K. Kajiwara, "Proposal and experimental verification of Bragg wavelength distribution measurement within a long-length FBG by synthesis of optical coherence function," *Opt. Express*, vol. 16, pp. 7881–7887, May 2008.

[10] L. Thévenaz, S. Chin, J. Sancho, and S. Sales, "Novel technique for distributed fibre sensing based on faint long gratings (FLOGs)," in *Proc. SPIE*, vol. 9157, pp. 91576W–91576W–4, Jun 2014.

[11] J. Sancho, S. Chin, D. Barrera, S. Sales, and L. Thévenaz, "Time-frequency analysis of long fiber Bragg gratings with low reflectivity," *Opt. Express*, vol. 21, pp. 7171–7179, Mar 2013.

[12] M. K. Barnoski, M. D. Rourke, S. M. Jensen, and R. T. Melville, "Optical time domain reflectometer," *Appl. Opt.*, vol. 16, pp. 2375–2379, Sep 1977.

[13] L. Chen, S. Benjamin, P. Smith, and J. Sipe, "Ultrashort pulse reflection from fiber gratings: a numerical investigation," *J. Lightwave Technol.*, vol. 15, pp. 1503–1512, Aug 1997.

[14] J. Azaña and M. A. Muriel, "Study of optical pulses-fiber gratings interaction by means of joint time-frequency signal representations," *J. Lightwave Technol.*, vol. 21, p. 2931, Nov 2003.

[15] B. Yun, N. Chen, and Y. Cui, "Highly sensitive liquid-level sensor based on etched fiber Bragg grating," *Photonics Technology Letters, IEEE*, vol. 19, pp. 1747–1749, Nov 2007.

[16] T. Guo, Q. Zhao, Q. Dou, H. Zhang, L. Xue, G. Huang, and X. Dong, "Temperature-insensitive fiber Bragg grating liquid-level sensor based on bending cantilever beam," *Photonics Technology Letters, IEEE*, vol. 17, pp. 2400–2402, Nov 2005.

[17] J. E. Antonio-Lopez, J. J. Sanchez-Mondragon, P. LiKamWa, and D. A. May-Arrioja, "Fiber-optic sensor for liquid level measurement," *Opt. Lett.*, vol. 36, pp. 3425–3427, Sep 2011.

[18] D. Bo, Z. Qida, L. Feng, G. Tuan, X. Lifang, L. Shuhong, and G. Hong, "Liquid-level sensor with a high-birefringence-fiber loop mirror," *Appl. Opt.*, vol. 45, pp. 7767–7771, Oct 2006.

[19] M. Lomer, A. Quintela, M. López-Amo, J. Zubia, and J. M. López-Higuera, "A quasi-distributed level sensor based on a bent side-polished plastic optical fibre cable," *Measurement Science and Technology*, vol. 18, p. 2261, Jun 2007.

[20] M. Gagné, S. Loranger, J. Lapointe, and R. Kashyap, "Fabrication of high quality, ultra-long fiber Bragg gratings: up to 2 million periods in phase," *Opt. Express*, vol. 22, pp. 387–398, Jan 2014.

[21] J. Huang, X. Lan, M. Luo, and H. Xiao, "Spatially continuous distributed fiber optic sensing using optical carrier based microwave interferometry," *Opt. Express*, vol. 22, pp. 18757–18769, Jul 2014.

[22] C. Hu, H. Wen, and W. Bai, "A novel interrogation system for large scale sensing network with identical ultra-weak fiber Bragg gratings," *J. Lightwave Technol.*, vol. 32, pp. 1406–1411, Apr 2014.

[23] W. Bai, H. Yu, D. Jiang, and M. Yang, "All Fiber Grating (AFG): a new platform for fiber optic sensing technologies," in *Proc. SPIE*, vol. 9634, pp. 96342A–96342A–4, Sep 2015.

[24] *FBGS - Draw Tower Gratings.* Available at `http://www.fbgs.com/home/`.

[25] M. A. Soto and L. Thévenaz, "Modeling and evaluating the performance of Brillouin distributed optical fiber sensors," *Opt. Express*, vol. 21, pp. 31347–31366, Dec 2013.

Chapter 3

Long FBGs-based sensors interrogating using microwave photonics filtering techniques

3.1 Introduction

Microwave photonics (MWP) is a promising discipline which collects together the field of microwave (MW) engineering with optoelectronics, relying on the interaction between MW or millimeter waves with optical wave signals. This emerging field has attracted great interest in the last decades not only from both the research communities but also from the commercial sector, leading to new possibilities in a variety of application fields such as radar, communications, sensor systems or instrumentation [1, 2]. The reason of this success stems from the fact that the optical domain allows the realization of key functionalities in MW and millimeter wave systems which are either complex or even not directly possible in the radio-frequency (RF) domain, such as high purity MW signal and waveform generation, tunable and reconfigurable adaptive filtering, optical beam forming, true-time delay and phase shift, optoelectronic oscillators, analog to digital conversion and radio over fiber communication systems [3–8].

The attractiveness and potentialities of MWP led us to study the possibility of mixing the areas of MW and optics for sensing applications. Both MW and optoelectronics obey to the same electromagnetic laws and then present common features but also significant differences. In MW domain, due to the large wavelength of MW (i.e. low frequency), construction of an interferometric structure does not require a precision as high as that needed by an optical interferometer, being the size of a MW interferometer larger than that of its counterpart in optical domain. Moreover, MW interference can be more easily resolved than the optical interference in which the detecting devices are not fast enough to follow the very high optical frequency. However, on the other hand, the loss in MW waveguides are consistently high if compared with the fiber optic link loss, limiting the maximum length that can be covered by MW transmissions. Furthermore, optical devices and systems generally have high quality factors than MW devices, are spark-free and immune to electromagnetic interference (EMI) [1, 9]. For these reasons, photonics-assisted techniques have raised increasing interest during the past decades, leading to new possibilities in a variety of sensing applications [10–14].

In this chapter, a technique to interrogate photonic devices based on long FBGs and theirs potential applications to distributed fiber sensing is proposed and demonstrated via experiments. This technique has several advantages derived from the fact that it relies on interference in the MW rather than optical domain. As commented above, MW interferometry is by far more stable and easier to control and, if suitably combined with photonics, provides a remarkable spatial accuracy. Furthermore, since the sensors are based on a discrete time filter configuration, the system spectral performance can be properly tailored/reconfigured. Thus, the methodology presented involves exploiting the best advantages brought by two symbiotic technologies: microwaves and photonics. Relying on MW interferometry and working under incoherent operation, as it will be described afterwards, the configurations proposed are intrinsically robust against environmental changes, stable and with good repeatable performance [15–17]. Finally, this technique is potentially low cost as it is based on low bandwidth RF and off-the-shelf photonic components rather than on ultra-short pulses, optical interferometry or optical frequency domain reflectometry (OFDR) techniques.

It is worth mentioning that MWP and OFDR techniques present common characteristics but also significant differences. Both MWP and OFDR schemes use interferometry-based technologies and Fourier transform based methods to map the response of the device under interrogation as a function of the distance. However, to do this, MWP approach employs a continuous wave (CW) light source which is electro-optically modulated with a MW signal. On the contrary, OFDR systems use a tunable laser source whose optical frequency is linearly swept in time. Moreover, unlike the case of MWP technology, OFDR results polarization-dependent and requires additional devices to mitigate signal fading. On the other hand, OFDR allows large-scale measurements with better performance in terms

of spatial resolution and precision, although such performance are made possible by means of a complicated cross-correlation method. [9, 18].

The proposed MWP technique is specifically suited when a spot event must be precisely identified and located, such as hot spots or cracks in structures. The overall idea within this work has been evolved and demonstrated step by step starting from preliminary tests that have led to the development of a very long distributed sensor based on an array of weak FBGs. To get started, we have demonstrated the feasibility of the MWP filtering technique to interrogate a grating by using a 10 cm-long high reflectivity FBG as sensing device. Such a system proved its feasibility to detect several spot events with spatial accuracy less than 1 mm. However, in this case since the FBG used as a quasi-distributed sensor has high reflectivity ($\approx 99\%$), the most important limitation arises from the fact that the system is not able to detect events having the same magnitude. Thus, to overcome this limitation a pair of low reflectivity ($< 6\%$) FBGs has been employed as sensing device. With this configuration, several events have been detected with a spatial accuracy of less than 1 mm using a modulator and a photo-detector (PD) with a modest bandwidth of 500 MHz. The latter has laid the foundation for the development and implementation of a long fiber optic sensor based on very weak FBGs (reflectivity $\approx 0.1\%$). Hence, we have proposed and validated a distributed sensor consisting of a 5 m-long fiber, containing 500 equal 9 mm-long Bragg gratings. The detection of spot events along the sensor has been demonstrated with remarkable accuracy under 1 mm, using a PD and a modulator with a bandwidth of only 500 MHz. All these sensors prove to be simple, robust, polarization insensitive and allow a lowering of the instrumentation complexity for distributed sensing applications.

3.2 Principle of operation

The fundamental concept beyond the proposed methodology is inspired on the principle of operation of a MWP filter and is depicted in Fig. 3.1(a). The output of a CW light source is electro-optically modulated with a MW signal. At the output of the electro-optical modulator (EOM) the modulated optical signal is split into N arms. Each arm has a delay-line and an attenuator (or amplifier) in order to provide a delayed and weighted replica of the original signal. These time-delayed and weighted optical signals are combined together and then photo-detected. In the detection process, the different taps can be mixed according to either a coherent or an incoherent basis. In case of incoherent mixing, the tap combination at the PD is insensitive to environmental effects, stable and with a remarkably good repeatable performance. For these reasons, the experimental configurations proposed to interrogate the long FBG-based sensors have been all implemented under incoherent operation. Working under incoherent regime limits the minimum delay between consecutive taps, which should be at least one order of magnitude greater than the source coherence time, as will be explained in the next section.

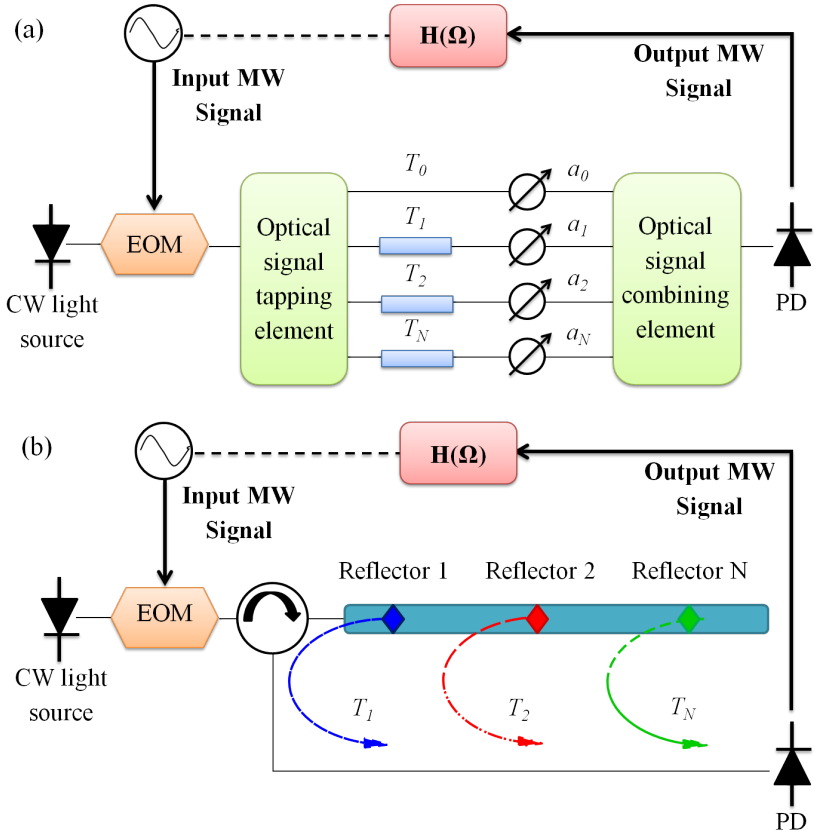

Figure 3.1: (a) Schematic diagram of the fundamental concept beyond the methodology, representing a N tap MWP filter configuration. (b) Conceptual illustration of the photonics sensor interrogation using MWP filtering technique.

The MW signal is acquired and the electrical frequency response $H(\Omega)$ of such a structure is given by [3]

$$H(\Omega) = \sum_{k=1}^{N} a_k e^{-j\Omega T_k} \tag{3.1}$$

where Ω is the MW angular frequency and a_k is the weight of the k-th replica that is delayed by T_k. When $T_k = k \cdot T, \forall k$, (3.1) identifies a transfer function with a periodic spectral characteristic; the frequency period is known as free spectral range (FSR) and it is inversely proportional to the time spacing T between samples [3].

In the case of the proposed sensing methodology, schematically illustrated in Fig. 3.1(b), delayed replicas of the original signal are produced by the different reflection points located along the sensing fiber, as it will be clarified hereinafter. Thus, the response of the sensor is described also by (3.1), where the number of taps N is equal to the number of reflectors located along the fiber, while the delays are proportional to the distances between consecutive reflectors.

In order to simplify the mathematics behind the proposed technique, let's assume to have a two tap MWP filter, which means two signal interference. The complex amplitudes of the two intensity modulated optical waves can be written as [9, 19]

$$E_i(t, L_i) = A\sqrt{1 + M\cos\left[\Omega\left(t + \frac{L_W + L_i}{c}\right)\right]} \cdot \exp\left[-j\omega\left(t + \frac{L_i}{c}\right)\right], \quad i = 1, 2 \tag{3.2}$$

being t the time, A and M the amplitudes of the optical carrier and MW envelope, respectively (for simplicity we assume that the two signals have the same amplitude), ω the optical angular frequency, c the speed of light in vacuum. L_1 and L_2 are the two optical path lengths while L_W is the electrical length of the common MW path. Hence, the power of the two superimposed signals at the PD results

$$\begin{aligned}
|E|^2 &= |E_1 + E_2|^2 \\
&= 2A^2 + \\
&+ 2A^2 M\cos\left[\Omega\left(\frac{L_1 - L_2}{2c}\right)\right]\cos\left[\Omega\left(t + \frac{2L_W + L_1 + L_2}{2c}\right)\right] + \\
&+ 2A^2\sqrt{\left\{1 + M\cos\left[\Omega\left(t + \frac{L_W + L_1}{c}\right)\right]\right\}\left\{1 + M\cos\left[\Omega\left(t + \frac{L_W + L_2}{c}\right)\right]\right\}} \cdot \\
&\cdot \int_{\omega_{min}}^{\omega_{max}} \frac{1}{\omega_{max} - \omega_{min}}\cos\left(\omega\frac{L_1 - L_2}{c}\right)d\omega
\end{aligned} \tag{3.3}$$

being ω_{max} and ω_{min} the maximum and minimum frequencies of the light source, respectively. There are three different contributions in (3.3): the first contribution is the direct current (DC) term, which is canceled if the optical detection is synchronized at the modulation frequency. The second and third contributions are the MW term and the optical term, respectively. By performing a frequency scanning, the MW term can be obtained in terms of scattering parameters, and then used for sensing applications, as it will be explained in the next sections.

The main limitation of this technique arises from the fact that the conditions for incoherent regime operation have to be guaranteed. This implies that the minimum delay between two consecutive reflections, has to verify that $t_c << T$ where t_c, the optical source coherence time is given by [20]

$$t_c = \frac{1}{\Delta f} \tag{3.4}$$

being Δf the spectral bandwidth of the source. In the proposed method, in order to reduce the value of t_c and to obtain a better range, a broadband source (BBS) is proposed. When the optical path difference $\Delta L = L_1 - L_2$ is sufficiently grater than the coherence length of the optical source, $L_c = t_c \cdot c$, the integral form in the optical contribution approaches to zero [9]. The minimum delay between the two adjacent reflectors T_{min}, is related to the distance L_{min} between them by

$$T_{min} = \frac{2n_g L_{min}}{c} \tag{3.5}$$

where n_g is the group refractive index of the fiber. Therefore, to secure an incoherent regime

$$L_{min} >> \frac{c}{2n_g \Delta f} = \frac{\lambda^2}{2n_g \Delta \lambda} \tag{3.6}$$

where $\Delta f = c\Delta\lambda/\lambda^2$, being $\Delta\lambda$ the source linewidth in wavelengths units and λ the central emission wavelength.

3.3 Experimental measurements and results

In this section, different FBG-sensors based on MWP filtering implementations are presented, for spot events detection and quasi-distributed sensing applications. Firstly, the feasibility of the MWP filtering technique to interrogate a 10 cm-long high reflectivity FBG is demonstrated. However, due to high reflectivity of the sensing grating, the system results not able to detect events having the same magnitude, as it has been already explained in the section 2 of the 2$^{\text{nd}}$ chapter. To overcome this limitation a pair of low reflectivity FBGs has been employed as sensing device, so laying the foundation for the development and implementation of a 5 m-long sensor based on a network of 500 ultra weak gratings cascading along a single optical fiber.

3.3.1 High reflectivity FBG sensor interrogation

Fig. 3.2 shows the experimental setup used to interrogate a 10 cm-long FBG with $\approx 99\%$ reflectivity and ≈ 14 GHz full width at half maximum (FWHM). The signal from a BBS is filtered by means of a tunable band-pass filter featuring a bandwidth of 0.45 nm centered at the Bragg wavelength of the FBG. The resonance of the grating is 1554.0 nm at room temperature. Using (3.4), a time coherence of 17.78 ps for the filtered optical source is obtained, which dictates smallest time spacing between spot events of ≈ 100 ps. This implies that the distance between hot spots should be longer than 10 mm to maintain the conditions of the incoherent regime.

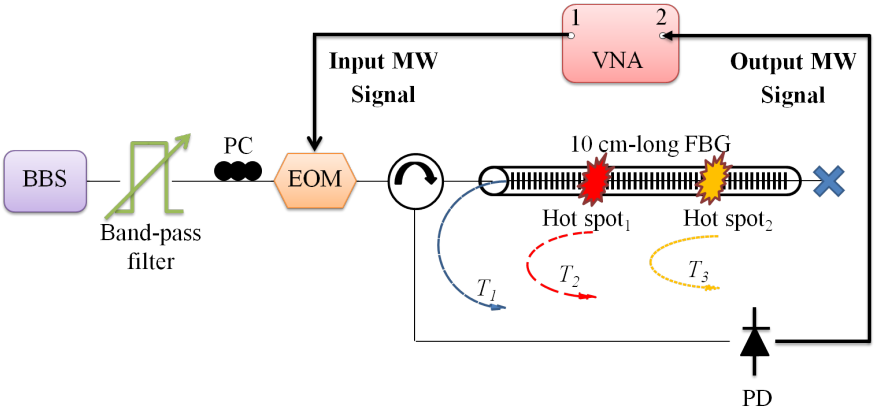

Figure 3.2: Schematic layout used to interrogate the 10 cm-long high reflectivity FBG.

The output of the tunable optical filter is electro-optically modulated with a MW signal generated by a vector network analyzer (VNA). The MW signal consists of a RF tone swept from 10 MHz to 10 GHz. A polarization controller (PC) is placed before the modulator to enhance the modulation efficiency. At the output of the EOM, the signal is sent into the FBG through an optical circulator, and hence the signal back-reflected by the grating is photo-detected. In this way, the frequency response of the system can be analyzed by monitoring the scattering parameter S_{21}, which relates the RF detected signal to the input modulating MW signal.

Due to the high reflectivity of the FBG, most of the input signal is reflected at the initial section of the FBG [21, 22]. However, a local change of temperature in a 5 mm hot spot placed at a certain point along the sensing grating will produce a local Bragg frequency shift. When this occurs, besides the main reflected signal, which is generated at the initial section of the grating, a second reflected signal is produced at the point where the hot spot is located. In this way, the presence of a hot spot results in a two tap MWP filter and it is possible to determine the location of the spot event by evaluating the FSR of the filter. In fact, in the case

of a two tap MWP filter, the delay between taps T (which is inversely proportional to the FSR of the MWP filter) is related to the distance L between them by

$$T = \frac{1}{FSR} = \frac{2n_g L}{c}. \tag{3.7}$$

Fig. 3.3(b) shows the experimental results obtained by moving the hot spot along the FBG as schematically illustrated in Fig. 3.3(a). As expected the recovered response is similar to a two tap MWP filter; the two taps are the reference reflection placed at the entry point of the FBG and the reflection caused by the hot spot. Fig. 3.3(b) shows as the closer the hot spot is to the beginning of the grating, the smaller results the delay between taps T and, in turn, the higher is the FSR of the MWP filter. The FSR has been evaluated with a frequency step of 0.01 MHz, which corresponds to an estimated spatial accuracy under 1 mm. The length spacing between the two taps is calculated according to the (3.7) and from this value the hot spot position (referred to the beginning of the FBG) is determined.

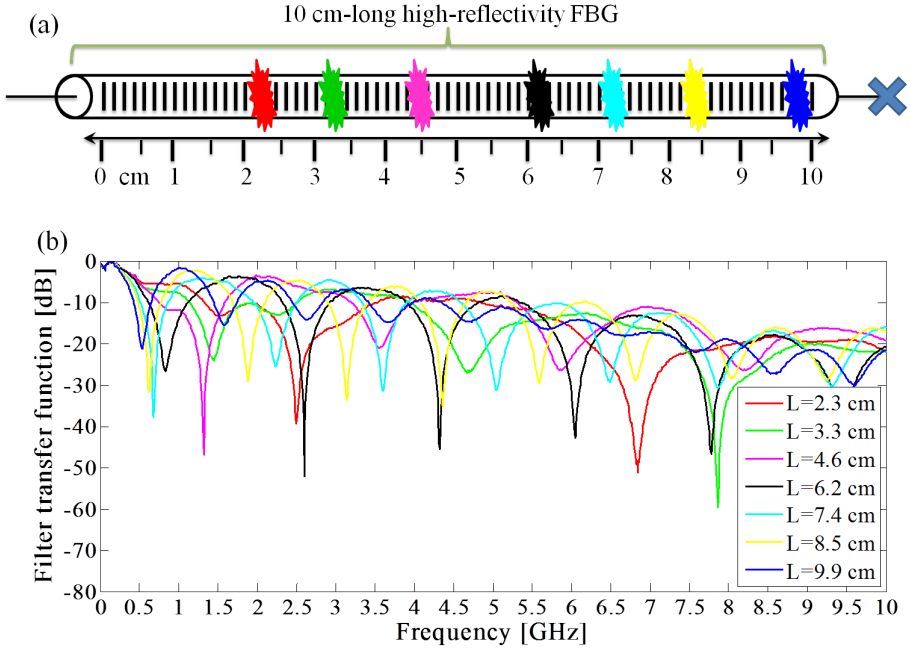

Figure 3.3: (a)Schematic illustrating the different position of the hot spot along the sensor. (b) Frequency response of the two tap MWP filters achieved by moving the hot spot along the 10 cm-long high reflectivity FBG.

The system is also able to detect the presence and position of two or more hot spots. Fig. 3.4(a) shows the response of the sensor when one and two hot spots are present (two tap and three tap MWP filter, correspondingly). In the latter, since retrieving the delays directly from the transfer function is time consuming, the most efficient approach to calculate the distance between the input end of the FBG and the hot spots is simply to take the inverse Fourier transform (IFT) of the measured S_{21} parameter. Fig. 3.4(b) shows the IFT of the amplitude of the three tap filter transfer function illustrated in Fig. 3.4(a) where two hot spots are placed along the grating (blue curve) and the IFT of the amplitude of the two tap filter obtained when one of the hot spots is suppressed (red curve). The time differences between the main peak and the two pairs of sub-pulses from Fig. 3.4(b) (blue curve) represent the time separations between the beginning of the FBG and the position of the first and second hot spot, respectively. By using (3.7), the distance between the entry point of the grating and each event is calculated to be 4.2 cm for the first hot spot and 7.8 cm for the second hot spot.

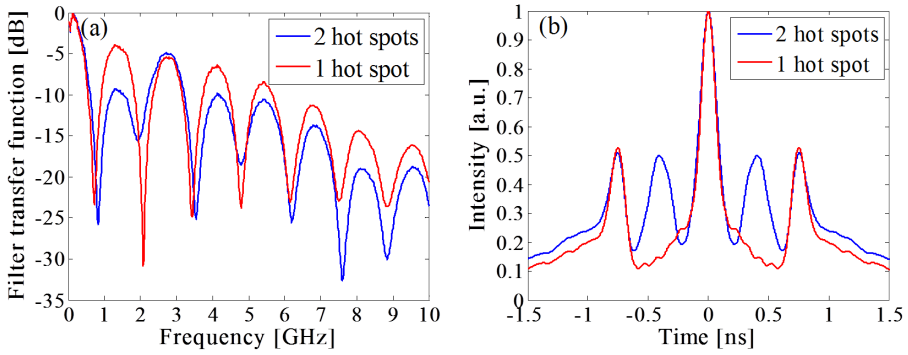

Figure 3.4: (a) Frequency response of the three tap and two tap MWP filters obtained by placing two hot spots and one hot spot along the 10 cm-long grating, respectively. (b) IFT of the amplitude of the MWP filters illustrated in Fig. 3.4(a).

It is worth to notice that Fig. 3.4(b) shows two sub-pulses (one on the negative time semi-axis and the other one on the positive time semi-axis) symmetrically located with respect to the main pulse at time $t = 0$. This is because only the amplitude (and not both amplitude and phase response) of the MWP filter has been considered. The reason of this choice comes to the fact that we have calculated both the IFT of the amplitude of the acquired filter transfer function and the IFT of amplitude and phase of the filter transfer function. Eventually we have observed that both IFT signals show identical results (from the viewpoint of our measurements purpose) and that only the amplitude response of the acquired MWP filter is actually needed to determine the time separation between taps and therefore the position of the events along the sensor. For this reason, we have decided to only use the amplitude response in the IFT calculation, because it makes the IFT algorithm easier and faster and the setup more cost efficient.

To alleviate the bandwidth requirements of the modulator and the PD, a variant of the setup is proposed, which is illustrated in Fig. 3.5. A reference arm is used in this case in order to obtain a higher time spacing T between taps, which leads to a shorter FSR. Here a variable optical attenuator (VOA) is placed to control the magnitude of the reference signal in order to make it matches as much as possible the weight of the tap provided by the hot spot. This is actually a key step for achieving a high visibility of the two tap MWP filter [9]. Besides, in the reference arm a piece of single mode fiber (SMF) is also located, whose length has been opportunely chosen in order to suitably control the FSR of the two tap MWP filter. Under these conditions, the hot spot position can be evaluated by using a modulator and a PD with a modest bandwidth of only 1 GHz.

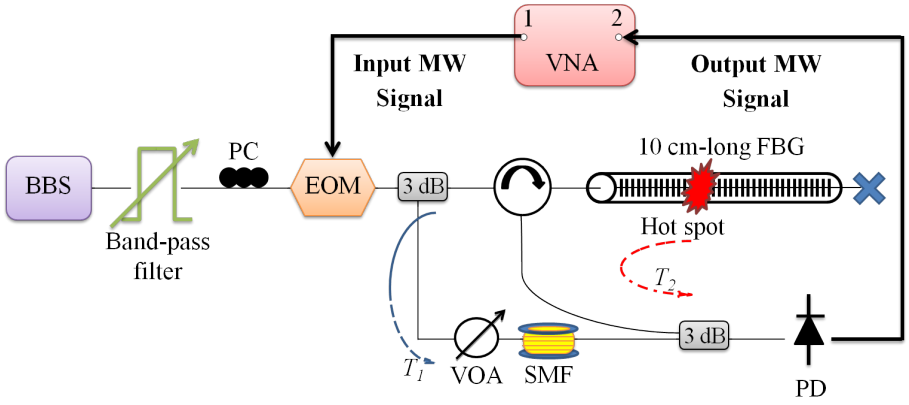

Figure 3.5: Experimental setup to interrogate the 10 cm-long FBG. A reference arm is used to obtain higher time spacing between taps (i.e. shorter FSR), so alleviating the bandwidth requirements of the EOM and the PD.

The blue curve in Fig. 3.6 represents the two tap MWP filter created by the combination of the tap provided by the signal reflected by the initial section of the grating and the tap provided by the reference arm. When a hot spot is placed along the FBG, another tap is created, actually resulting in a three tap MWP filter. But, a two tap filter is desirable to simplify the measurement process; for this reason, by judiciously tuning the optical band-pass filter, the tap created at the initial section of the FBG (reflecting the signal at the original Bragg resonance, 1554.0 nm) is filtered out and a two tap MWP filter is obtained - due to the combination of the tap provided by the signal reflected by the hot spot and the tap provided by the reference arm - as schematically illustrated in Fig. 3.5. In this case the location of the hot spot along the sensing FBG can be calculated according to

$$L = \frac{c}{2n_g}\left(\frac{1}{FSR} - \frac{1}{FSR_{ref}}\right) \tag{3.8}$$

being FSR_{ref} the FSR of the two tap MWP filter used as reference trace (see Fig. 3.6). This way, the position of the hot spot referred to the beginning of the grating is evaluated with a spatial accuracy of less than 1 mm, depending of the VNA frequency resolution.

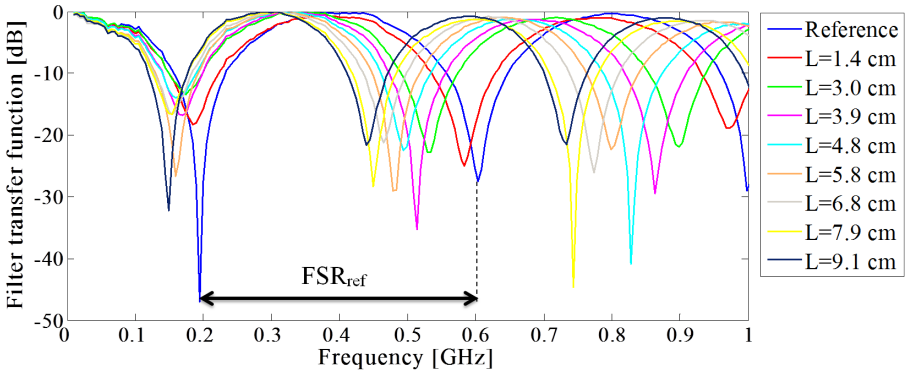

Figure 3.6: Two tap MWP filters obtained by using a reference tap provided by a reference arm and a tap provided by a hot spot located along the sensing FBG. The blue curve represents the two tap MWP filter created by the combination of the reference tap and the tap provided by the reflection at the beginning of the FBG.

Anyway, in the former configurations, due to the high reflectivity of the sensing FBG, the most important limitation arises from the fact that both schemes are not able to detect events having the same magnitude. This is basically because hot spots having the same temperature will reflect light at the same Bragg wavelength λ_{HS}; however, due to the strong reflectivity of the grating, the incoming signal at λ_{HS} will be almost completely back-reflected by the first spot event [21, 22] so impeding the detection of the second hot spot (as actually no light at λ_{HS} reaches the second hot zone). To overcome this limitation, a weak FBGs-based sensing device has been investigated, as detailed in the following subsection.

3.3.2 Weak FBGs-based sensor interrogation

In this subsection, a FBG sensing device able to detect one or more spot events, even if they have the same magnitude, is described. Experimental measurements have been performed using the setup illustrated in Fig. 3.7. Once again, an optical signal provided by a BBS is filtered using a tunable band-pass filter centered at the Bragg wavelength of the FBG sensing device, which is 1534.55 nm at room temperature. The FBGs have a bandwidth of about 16.65 pm. Here, as the filter bandwidth is 1 nm, the time coherence of the filtered optical source is 8 ps [8]. The smallest time spacing between hot spots which safely secures the incoherent regime operation would be an order of magnitude bigger than this value. This implies that the distance between spot events should be longer than 8.24 mm [20]. The output

of the optical filter is electro-optically modulated by a MW signal generated by the VNA. In this scheme, the RF modulating signal is swept in a limited frequency range from 10 MHz to 500 MHz, so reducing the system bandwidth requirements. At the output of the EOM, the signal is sent into the FBG sensor through an optical circulator. Hence the reflected signal is photo-detected and finally the frequency response of the system is analyzed by monitoring the scattering parameter S_{21}.

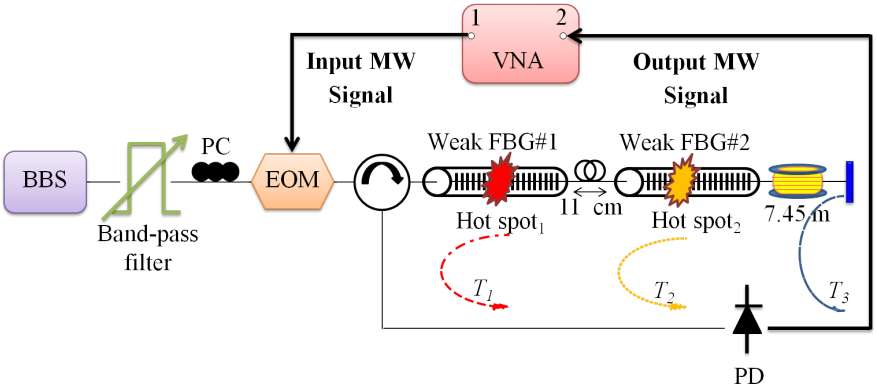

Figure 3.7: Experimental setup to interrogate the weak FBGs sensor.

The initial idea of this experiment was to fabricate a very long weak FBG, but due to the limitations of our FBGs fabrication system, gratings longer than 10 cm cannot actually be fabricated. Hence, as a proof-of-concept, the quasi-distributed sensor proposed is made by a pair of identical weak ($R < 6\%$) 10 cm-long FBGs separated by 11 cm, while a 7.45 m-long SMF is appended after the second FBG. The other end of this fiber sensor is left opened in the air to provide a reflection signal that will be used as reference tap. The reason of this choice comes to the fact that in the case of a weak FBG, the input signal is continuously back-reflected while propagating through the entire length of the grating [21, 22]. Hence we no longer have a reflection at the beginning of the grating that can be used as a reference point to establish the locations of the spot events along the sensor. Therefore we use the Fresnel reflection at the end facet of the fiber left open in the air as reference point to measure the positions of the spot events along the sensor.

If a hot zone is created at a certain point of the first grating, this will produce a local Bragg frequency shift and generate a reflected signal at the point where the hot spot is placed. The wavelength sweep of the optical band-pass filter is synchronized with the data acquisition process. This way, by performing a wavelength scan of the input signal, the amplitude of the MWP filter response can be maximized. Hence, by tuning the optical band-pass filter, the taps related to the original FBGs reflections are filtered out and a two tap MWP filter is obtained

(see Fig. 3.8(a)), resulting from the combination of the tap provided by the signal reflected by the hot spot and the reference tap.

In the same way, if the hot spot is removed from the first FBG and placed along the second grating, another two tap MWP filter is created, as shown in Fig. 3.8(b). The locations of the spot events can be obtained directly by evaluating the FSR of the MWP filters as it is described by (3.7), or equivalently by using the IFT. The FSR has been evaluated with a frequency step of 1 kHz, which corresponds to an estimated spatial accuracy of less than 1 mm. This way, the distances between the end of the SMF and the two hot spots placed in the first and the second FBG are $l_1 = 7.716$ m and $l_2 = 7.506$ m, respectively.

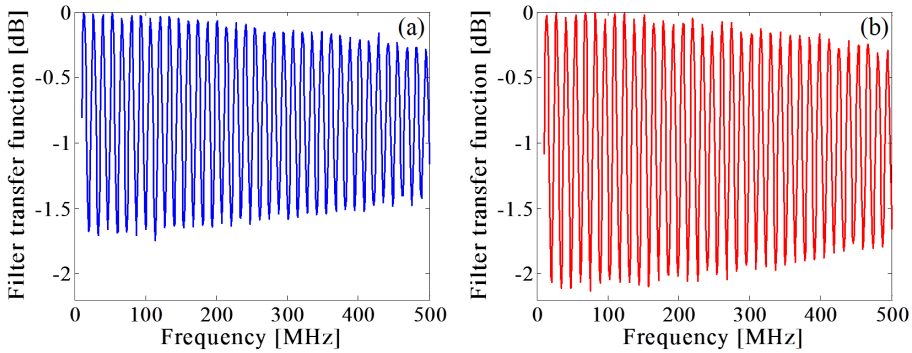

Figure 3.8: (a) Two tap MWP filter created by the reference tap and by the tap provided by the hot spot placed in the first FBG. (b) Two tap MWP filter obtained by the reference tap and by the tap provided by the hot spot placed in the second FBG.

When two hot spots are placed along each FBG and the band-pass filter is properly tuned in order to eliminate the original FBG reflections, a three tap MWP filter is obtained, as shown in Fig. 3.9(a) (blue solid line). In this case, the most efficient approach to calculate the positions of the two hot spots referred to the end of the SMF is simply to take the IFT of the amplitude response of the measured S_{21} parameter, which is depicted in Fig. 3.9(b) (blue solid line). The above mentioned distances are calculated to be $l_1^{IFT} = 7.7166$ m and $l_2^{IFT} = 7.5063$ m, in agreement with the values evaluated previously. Also simulations have been performed for the three tap MWP filter response (green dashed line in Fig. 3.9(a) and (b)), matching the measurement real data and so proving the rightness of the methodology employed.

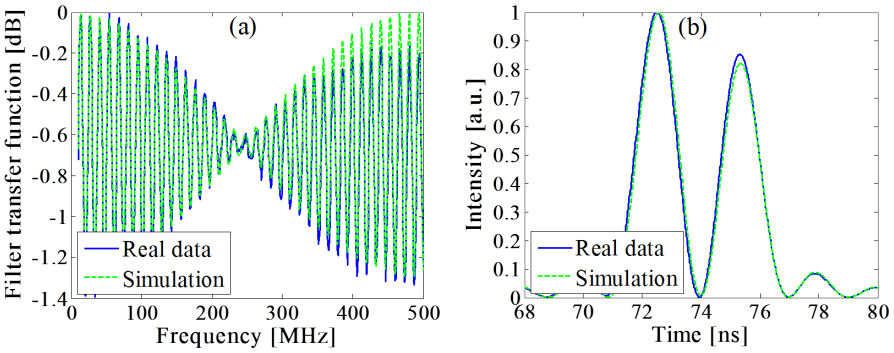

Figure 3.9: (a) Frequency response of the three tap MWP filters (real and theoretical) obtained by placing two hot spots along the sensor and using the end-facet of the sensing fiber as reference tap. (b) IFT of the amplitude response of the three tap MWP filters (real and theoretical) depicted in Fig. 3.9(a).

Furthermore, the distance between the two hot spots, L_{1-2}, can be measured evaluating the FSR of the two tap MWP filter, obtained if the reflection at the end of SMF is suppressed, as illustrated by the blue curve in Fig. 3.10. In order to eliminate this reference tap, an angled polished connector (APC) and an index-matching fluid (IMF) are now applied at the end of the SMF. This way, if the second hot spot is moved, the FSR of the two tap filter changes, as shown by the red curve in Fig. 3.10. By evaluating the FSR, the distance between spot events can be calculated by (3.7).

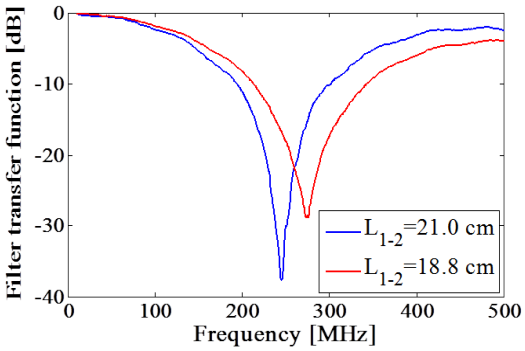

Figure 3.10: Frequency response of the two tap MWP filters obtained by placing two hot spots along the weak FBG-based sensor and eliminating the reference tap. When the second hot spot is moved, the FSR change.

Finally, it is worth mentioning that since the filter formed by the taps provided by the hot spots has just one FSR span (see Fig. 3.10), the minimum distance between two events should be more than 20 cm if an accuracy under 1 mm is desirable. Actually, this value arises from the modest bandwidth used to perform the experiment which means that the minimum distance between events could be further reduced by extending the frequency range. In fact, in order to correctly estimate the distance between hot spots by means of the IFT, the frequency response of the related MWP filter has to present at least one FSR span, if an accuracy of less than 1 mm is desirable. For this reason, the minimum detectable distance between spot events L_{1-2}^{min} is directly related to the VNA frequency span Δf_{VNA}, according to

$$L_{1-2}^{min} = \frac{c}{2n_g \Delta f_{VNA}}. \tag{3.9}$$

By using (3.9) the necessary increase in frequency span to reduce the distance between spot events to a desired value can be estimated.

The experiments and tests reported so far have demonstrated the capability of the approach based on a MWP filtering technique of interrogating quasi-distributed sensors based on grating structures. Against the backdrop of these positive results, we have proposed and validated a large scale distributed sensor network based on 500 identical FBGs, as it will be analyzed in the following subsection.

3.3.3 Large scale sensor network based on 500 ultra weak FBGs

For a large-scale sensor network, very low reflectivity of the sensing units results absolutely necessary, ensuring a low crosstalk level among identical sensors in the array and allowing the propagation of the optical signal over the entire length of the sensor. The long range sensor described here is composed of an array of 500 equal very weak (reflectivity $\approx 0.1\%$) FBGs written in cascade in a 5 m-long optical fiber. The nominal length of each FBG is 9 mm and the separation between consecutive FBGs in the array is ≈ 10 mm (from the center of a grating to the center of the consecutive one). The FBG cascade fiber was kindly provided by FBGS International [23], which fabricates optical fibers by using draw tower gratings (DTGs) technology, and its main features have been already described in the section 4 of the chapter 2.

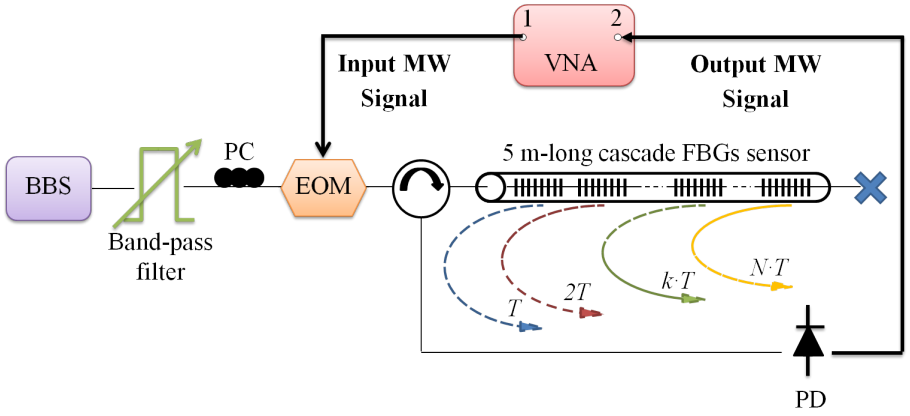

Figure 3.11: Schematic diagram implemented for interrogating the ultra weak FBG-based sensor.

The system used to interrogate the 5 m-long cascade sensor is the same as those described previously and it is schematically illustrated in Fig. 3.11. Once again, the band-pass filter bandwidth has been chosen to be 1 nm and it is centered at the nominal Bragg wavelength of the ultra weak FBGs. According to (3.4), the time coherence of the filtered optical source is 8 ps. The smallest time spacing which safely secures the incoherent regime operation would be at least an order of magnitude greater than this value. This implies that the distance between consecutive FBGs should be longer than 8.24 mm [20]; as the separation between the middle points of adjacent FBGs in the array is ≈ 10 mm, the incoherent regime operation is assured.

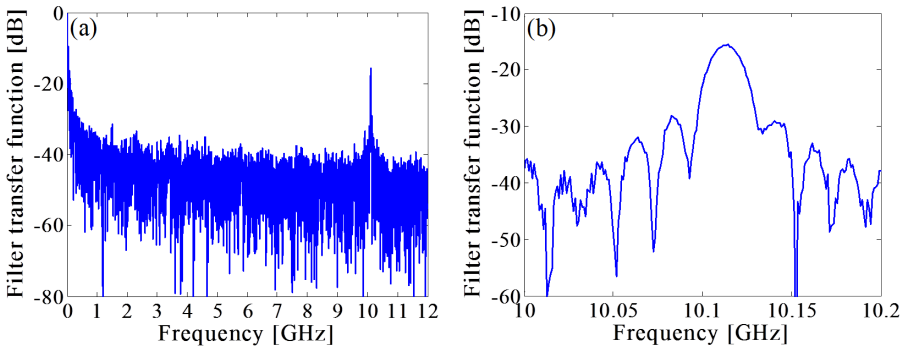

Figure 3.12: (a) Transfer function of the MWP filter describing the electrical system response (S_{21} parameter). (b) Detail of the filter transfer function showing the first main resonance.

As a first step, the MW tone provided by the VNA is swept from 10 MHz to 12 GHz in order to retrieve the electrical response of the system, described by the module of the scattering parameter S_{21} which is shown in Fig. 3.12(a), while Fig. 3.12(b) illustrates the detail of the MWP filter main resonance around 10.11 GHz. The FBGs very low reflectivity lets us assume that the incoming signal is back-reflected with almost the same weight from each of the 500 identical gratings. The value of the first main resonance (i.e., the FSR span), is related to the distance L_{FBGs} between two consecutive FBGs according to an equation identical to (3.7)

$$L_{FBGs} = \frac{c}{2n_g FSR}. \tag{3.10}$$

Similarly, taking advantage of this concept, the length of a spot event located along the sensing fiber can be calculated. The proposed device under test (DUT) produces delayed replicas of the original signal at the place where each reflector is located, as schematically shown in Fig. 3.11. As the spacing between consecutive gratings is constant, $T_k = kT, \forall k$, which means that (3.1) identifies a transfer function with a periodic spectral characteristic; the frequency period (FSR) is inversely proportional to the time-spacing T between samples [3]. The MWP filter so created and illustrated in Fig. 3.12(a) presents $N-1$ minima between two consecutive maxima. Hence, the distance between two minima (hereinafter FSR') can be used to calculate the number of taps contributing to the filter response. As the distance between consecutive FBGs in the DUT, L_{FBGs}, is a constant and known parameter, by evaluating the FSR' of the MWP filter response, the length L_{HS} of the hot spot can be calculated through the same way as before, using

$$L_{HS} = \frac{c}{2n_g FSR'}. \tag{3.11}$$

To corroborate this assumption, an experiment is set up using a frequency span of 500 MHz. The reason for this choice is due to the fact that this frequency range allows a better discrimination of the FSR' on the one hand, and on the other, this moderate span enables the use of devices with modest bandwidth.

The tunable optical band-pass filter located after the BBS plays a fundamental role in both the data acquisition process and the hot spot temperature estimation. In fact, the progressive sweep of the central wavelength of the optical filter is synchronized with the data acquisition process. This way, the sensing response to the hot region can be maximized when the rise/fall slope is located as close as possible to the peak corresponding to the hot spot, as shown in Fig. 3.13(d). Fig. 3.13(a) shows the case in which the optical filter response is far from both the DUT original reflection and the hot spot reflection. In this condition, no signal will be back-reflected and the VNA only displays a noise trace. Fig. 3.13(c) represents the case in which both the DUT original reflection and the hot spot reflection

are selected, while Fig. 3.13(b) and Fig. 3.13(d) illustrates the situation in which the band-pass of the optical filter is tuned in order to select the original reflection of the DUT and the hot spot reflection, respectively. In these cases a frequency response of a MWP filter will be represented at the VNA monitor. Finally, by continuing to move the band-pass of the optical filter towards higher wavelengths (see Fig. 3.13(e)), again no signal will be reflected from the DUT. Hence, a noise trace will be displayed by the VNA. This way, by performing a wavelength scan of the input broadband signal, the amplitude of the MWP filter response can be monitored and analyzed.

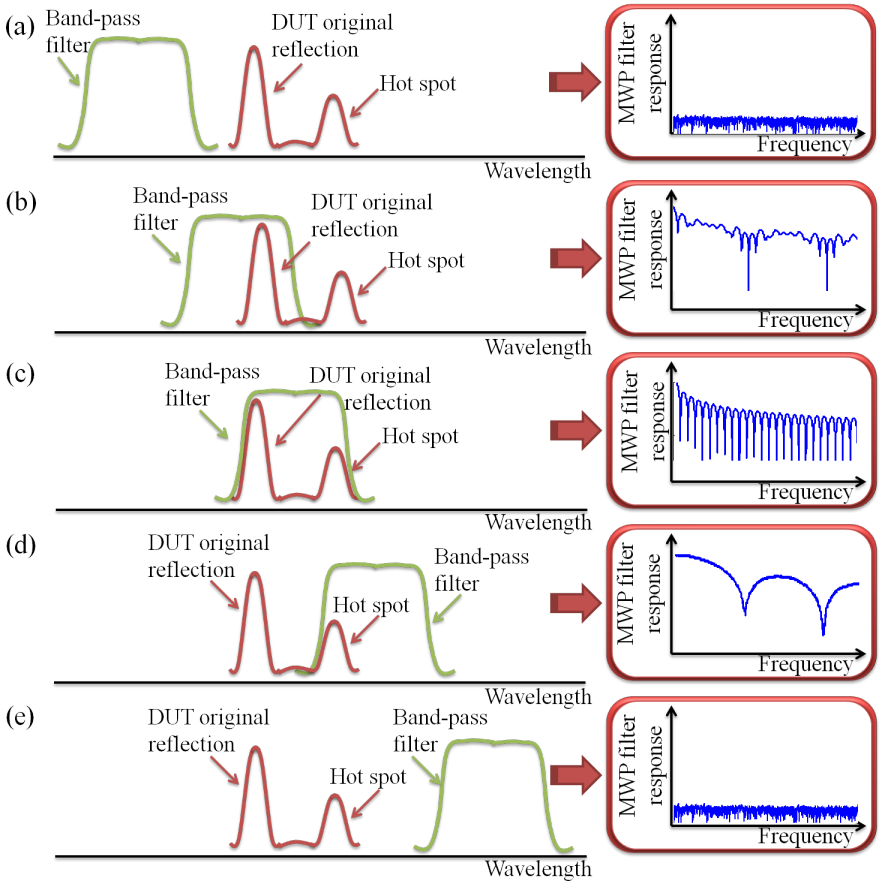

Figure 3.13: Schematic of the optical band-pass filter central wavelength scan. (a) The filter response is far from both the DUT original reflection and the hot spot reflection. (b) The filter is tuned to select the DUT original response reflection. (c) The filter is tuned to select both the DUT original reflection and the hot spot reflection. (d) The filter is tuned to select the hot spot reflection. (e) The filter response is again far from both the DUT original reflection and the hot spot reflection.

When no spot events are placed along the sensing device and the central wavelength of the optical filter is tuned in order to select the DUT original reflection, the electrical response of the system in the frequency range from 10 MHz to 500 MHz, in analyzed as illustrated in Fig. 3.14(a) (blue curve), which is in agreement with the theoretical simulation (red curve). These initial results indicate that, as the MWP filter presents 500 taps (i.e., 499 minima between one FSR span), the frequency separation between two consecutive minima is $FSR' = 20.23$ MHz, confirming the theory described above. Now, it is worth noting that, in case of non-uniformity of the 500 FBGs, it will negatively affect the periodicity of the filter transfer function. But, the results in Fig. 3.14(a) show how the frequency response of the MWP filter representing the measured system response matches the frequency behavior of the simulated system response in the 500 MHz span. This fact leads us to consider the contribution of the possible grating non-uniformity negligible in the evaluation of the sensing performance.

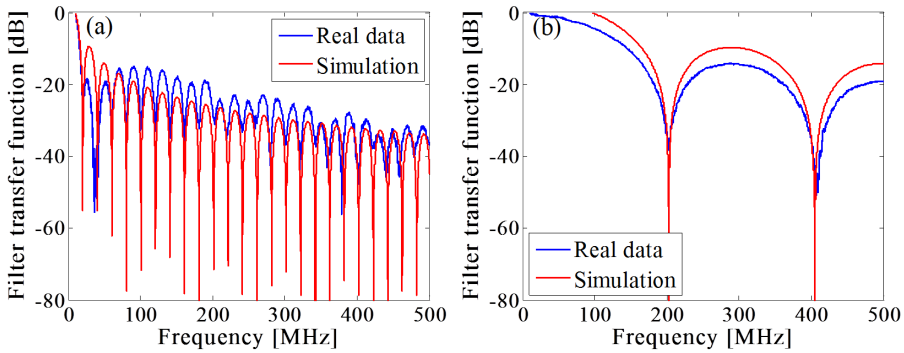

Figure 3.14: (a) Frequency response of the MWP filter representing the measured (blue curve) and simulated (red curve) system response in the frequency range from 10 MHz to 500 MHz. (b) Frequency response of the MWP filter (measured and simulated) obtained by placing a hot spot along the DUT and by opportunely tuning the optical band-pass filter.

Now, when a hot spot is placed along the 5 m-long sensing fiber, the heated surface suffers a period change which leads to a Bragg wavelength shift affecting the FBGs underlying the hot zone. If the optical filter is properly tuned in order to select the zone of the source spectrum reflected by the heated gratings (see Fig. 3.13(d)), the distance between minima in $H(\Omega)$ gives the length of the hot spot. This means that by evaluating the FSR' of the MWP filter depicted in Fig. 3.14(b) and using (3.11), the length of the hot zone is calculated to be 50.7 cm, with a spatial accuracy under 1 mm, dictated by the spatial resolution of the VNA.

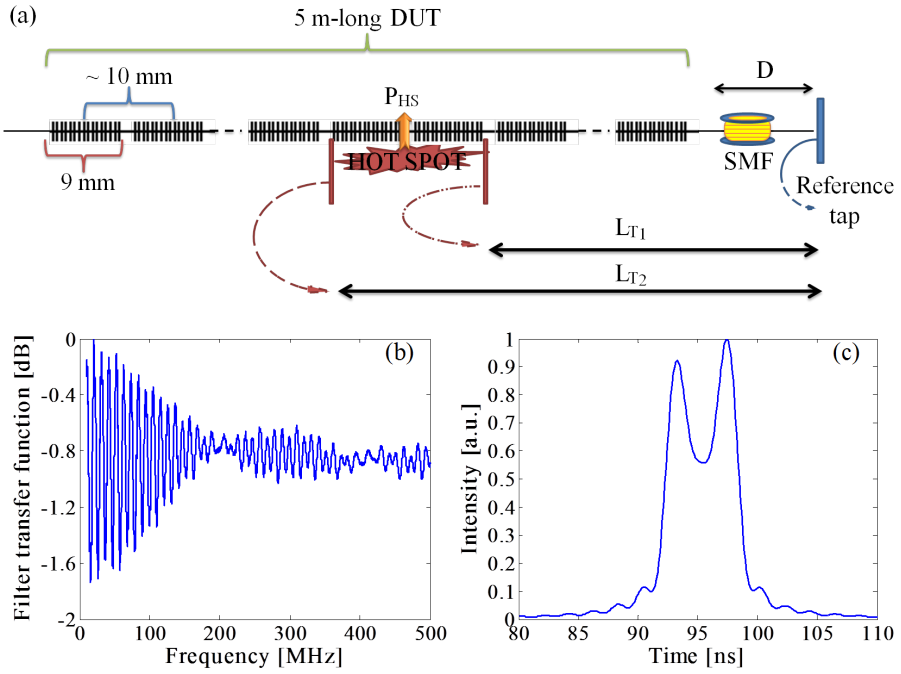

Figure 3.15: (a) Schematic illustration representing the portion of the system used to retrieve the position of the hot spot. (b) Frequency response of the three tap MWP filter obtained by placing a hot spot along the DUT and by using the reflection at the end facet of the SMF as a reference tap. (c) IFT of the amplitude of the MWP filter illustrated in Fig. 3.15(b).

Furthermore, in order to estimate the position of the spot event along the DUT, a piece of a SMF of length $D = 7$ m is appended at the end of the DUT, as illustrated in Fig. 3.15(a). As for the case of the pair of weak FBGs described in the above subsection, the other end of the SMF is left open in the air to provide a reflection signal that will be used as a reference tap. The distance between initial end of the hot spot and the end facet of the SMF, L_{T_1}, and the distance between the final end of the hot spot and the end facet of the SMF, L_{T_2} are related, once again, to the respective transit time between each end of the hot spot and the end facet of the SMF, T_1 and T_2 by

$$L_{T_i} = \frac{cT_i}{2n_g}, \quad i = 1, 2. \tag{3.12}$$

Now, by opportunely tuning the optical band-pass filter in order to select only the hot spot corresponding reflection (see Fig. 3.13(d)) the transfer function of the MWP filter in the frequency range from 10 MHz to 500 MHz is detected, as shown

in Fig. 3.15(b). Since retrieving the delays directly from the transfer function is time consuming, the most efficient approach to calculate the distance between the middle point of the hot spot and the end of the DUT, is simply to take the IFT of the measured S_{21} parameter, which is plotted in Fig. 3.15(c). In fact, the position of the middle point P_{HS} of the hot spot along the sensor can be calculated by

$$P_{HS} = \frac{(L_{T_2} - D) + (L_{T_1} - D)}{2} = \frac{L_{T_2} + L_{T_1}}{2} - D. \tag{3.13}$$

By using (3.12) in (3.13), one can find

$$P_{HS} = \frac{(T_2/2 + T_1/2)c}{2n_g} - D. \tag{3.14}$$

This way, the position of the hot spot middle point is measured from the DUT farest end, resulting $P_{HS} = 2.844$ m.

It is worth mentioning that since the filter formed by the taps provided by the hot spot has about two minima (see Fig. 3.14(b)), the proposed configuration can also be used to detect the presence and location of spot events shorter than 50 cm. In particular, the minimum detectable hot spot is directly related to the VNA frequency span Δf_{VNA}, according to

$$L_{HSmin} = \frac{1.5c}{2n_g \Delta f_{VNA}}. \tag{3.15}$$

This means that by using a frequency span of 500 MHz the minimum measurable spot event is about 31 cm, if the methodology and the mathematical calculation so far detailed are used.

Even so, we have found that shorter hot spots can still be detected in this frequency range. In order to validate this concept, a hot spot shorter than 31 cm is placed at a certain point of the DUT. The electrical response of the MWP filter, obtained by sweeping the MW signal from 10 MHz to 500 MHz, is depicted in Fig. 3.16(a). Once again, by evaluating the FSR' of the MWP filter response and by using (3.11), the length of the hot spot is calculated to be $L_{HS} = 26.5$ cm. Also, the position of the hot spot can be calculated by using the reference tap, similarly to the procedure previously described, and by employing the IFT of the resulting filter transfer function (depicted in Fig. 3.16(b)), which is illustrated in the inset of Fig. 3.16(b). Now it can be seen that the IFT presents only one peak, which results related to the position of the hot spot middle point. In this case, the location of the spot event can be calculated by retrieving the peak time position T' and by using

$$P_{HS} = \frac{T'c}{2n_g} - D. \tag{3.16}$$

This way, the location of the middle point of the hot spot along the sensor is estimated to be $P_{HS} = 2.891$ m from the DUT farest end. Thus, the ultimate limit in the hot spot length and location results to be related to the VNA frequency span Δf_{VNA} according to

$$L_{HSmin} = \frac{c}{2n_g \Delta f_{VNA}}. \tag{3.17}$$

Even so, it is possible to release this limitation if the number of replicas of the MWP filter is increased, either by extending the frequency range or by mathematically improving the algorithm used for the IFT.

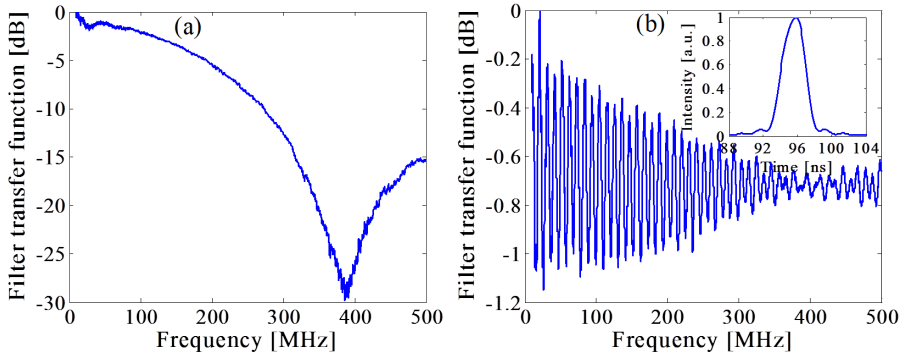

Figure 3.16: (a) Frequency response of the two tap MWP filter obtained by placing a 26.5 cm-long hot spot along the DUT. (b) Frequency response of the three tap MWP filter obtained by placing a 26.5 cm-long hot spot along the DUT and by using the reference tap. Inset: IFT of the three tap MWP filter depicted in Fig. 3.16(b).

Finally, in all configurations presented, the temperature of the hot spot can be evaluated due to the progressive scan of the central wavelength of the tunable band-pass filter, without using any more devices or additional wavelength scanned systems. For instance, in the last scheme proposed, based on the fiber temperature coefficient, which is 16.855 pm/°C, the temperature of the 50.7 cm long hot spot is estimated to be around 70°C. During this part of the experiment, the temperature of the hot spot was also measured with a commercial thermometer, which let us able to ensure a temperature accuracy of less than 1°C. Besides, the sensor temperature resolution is actually limited by the rise/fall slope of the optical band-pass filter and it will be certainly improved by using a tunable optical filter with high abrupt transition slope.

3.4 Conclusions

In this chapter, a technique for estimating the position, length and temperature of spot events along different FBGs-based sensors, inspired on the principle of operation of a MWP filter, has been described and demonstrated via experiments. By evaluating the FSR of the resulting MWP filter (or equivalently by calculating the IFT of the measured S_{21} parameter) the location and length of several spot events along the distributed FBG sensors can be detected with a remarkable spatial accuracy dictated by the frequency scanning step of the VNA.

The overall idea beyond this work has been developed and demonstrated step by step starting from preliminary experiments. Firstly, the feasibility of the MWP filtering technique to interrogate a 10 cm-long high reflectivity FBG has been demonstrated. In fact, hot spots have been detected along the sensing grating with a spatial accuracy under 1 mm. However, due to the high reflectivity of the grating, the system is not able to detect events having the same magnitude. To overcome this limitation a pair of identical low reflectivity FBGs has been employed as sensing device. With this configuration, hot spots have been detected (even having the same temperature) with identical performance as before in terms of spatial accuracy and using RF devices with a limited bandwidth. The latter has laid the foundation for the development and implementation of a large scale sensing network, based on 500 ultra weak FBGs. The detection of a hot spot along a 5 m-long FBG cascade sensor has been demonstrated with remarkable spatial accuracy of less than 1 mm, using a PD and a modulator with a modest bandwidth of only 500 MHz. Since the spatial accuracy basically depends on the system frequency step, the MWP-based methodology will be certainly able to reach the same performance in terms of accuracy even if the length of the sensing device is enhanced to obtain a higher measurement range.

Furthermore, in all configurations presented, the temperature of the hot spot can be evaluated due to the progressive scan of the central wavelength of the tunable band-pass filter, without using any more devices or additional wavelength scanned systems, with a measured accuracy of less than 1°C. The sensor temperature resolution is actually limited by the rise/fall slope of the optical filter and hence will be improved by using a tunable band-pass filter with a high abrupt transition slope.

Relying on MW interferometry and working under incoherent operation, the schemes proposed result intrinsically robust against environmental changes, stable and with remarkable good repeatable performance. For these reasons the measurements of the MWP filter response have been achieved with no need of averaging mode. The technique is potentially quasi-cost effectively solution as it is based on low bandwidth RF and off-the-shelf photonic components rather than on ultra-short pulses, optical interferometry or OFDR techniques.

Finally, it is worth mentioning that all the MWP filtering interrogation systems here described can also be used to implement crack/strain sensors. Besides, the use of a BBS relieves the complexity and the cost for stabilization control on light source, and since MW frequencies changes were measured, the influence of the intensity noise of the incoherent source does not lead to resolution impoverishment. In addition, although the use of a VNA may enhance the system complexity and expense, the instrumentation required could be simplified by replacing the VNA with an oscillator and a device able to analyze the magnitude response of the MWP filter generated.

Bibliography

[1] J. Capmany and D. Novak, "Microwave photonics combines two worlds," *Nature photonics*, vol. 1, pp. 319–330, Jun 2007.

[2] A. Seeds, "Microwave photonics," *Microwave Theory and Techniques, IEEE Transactions on*, vol. 50, pp. 877–887, Mar 2002.

[3] J. Capmany, J. Mora, I. Gasulla, J. Sancho, J. Lloret, and S. Sales, "Microwave photonic signal processing," *J. Lightwave Technol.*, vol. 31, pp. 571–586, Feb 2013.

[4] R. Minasian, "Photonic signal processing of microwave signals," *Microwave Theory and Techniques, IEEE Transactions on*, vol. 54, pp. 832–846, Feb 2006.

[5] A. Loayssa, J. Capmany, M. Sagues, and J. Mora, "Demonstration of incoherent microwave photonic filters with all-optical complex coefficients," *Photonics Technology Letters, IEEE*, vol. 18, pp. 1744–1746, Aug 2006.

[6] Y. Liu, J. Yang, and J. Yao, "Continuous true-time-delay beamforming for phased array antenna using a tunable chirped fiber grating delay line," *Photonics Technology Letters, IEEE*, vol. 14, pp. 1172–1174, Aug 2002.

[7] H. Shahoei and J. Yao, "Tunable microwave photonic phase shifter based on slow and fast light effects in a tilted fiber Bragg grating," *Opt. Express*, vol. 20, pp. 14009–14014, Jun 2012.

[8] W. Li and J. Yao, "An optically tunable frequency-doubling optoelectronic oscillator incorporating a phase-shifted-fiber-Bragg-grating-based frequency-tunable photonic microwave filter," in *Microwave Photonics, 2011 International Topical Meeting on Microwave Photonics Conference, 2011 Asia-Pacific, MWP/APMP*, pp. 429–432, Oct 2011.

[9] J. Huang, X. Lan, H. Wang, L. Yuan, and H. Xiao, "Optical carrier-based microwave interferometers for sensing application," in *Proc. SPIE*, vol. 9098, pp. 90980H–90980H–6, Jun 2014.

[10] M. Li, W. Li, J. Yao, and J. Azaña, "Femtometer-resolution wavelength interrogation of a phase-shifted fiber Bragg grating sensor using an optoelectronic oscillator," in *Advanced Photonics Congress*, p. BTu2E.3, Optical Society of America, Sep 2012.

[11] X. Zou, M. Li, W. Pan, B. Luo, L. Yan, and L. Shao, "Optical length change measurement via RF frequency shift analysis of incoherent light source based optoelectronic oscillator," *Opt. Express*, vol. 22, pp. 11129–11139, May 2014.

[12] Y. Deng, M. Li, N. Huang, H. Wang, and N. Zhu, "Optical length-change measurement based on an incoherent single-bandpass microwave photonic filter with high resolution," *Photon. Res.*, vol. 2, pp. B35–B39, Aug 2014.

[13] J. Huang, X. Lan, M. Luo, and H. Xiao, "Spatially continuous distributed fiber optic sensing using optical carrier based microwave interferometry," *Opt. Express*, vol. 22, pp. 18757–18769, Jul 2014.

[14] J. Yao, "Microwave photonics for high-resolution and high-speed interrogation of fiber bragg grating sensors," *Fiber and Integrated Optics*, vol. 34, pp. 230–242, Oct 2015.

[15] J. Capmany, B. Ortega, D. Pastor, and S. Sales, "Discrete-time optical processing of microwave signals," *J. Lightwave Technol.*, vol. 23, p. 702, Feb 2005.

[16] J. Capmany, B. Ortega, and D. Pastor, "A tutorial on microwave photonic filters," *J. Lightwave Technol.*, vol. 24, pp. 201–229, Jan 2006.

[17] J. Yao, "Microwave photonics," *J. Lightwave Technol.*, vol. 27, pp. 314–335, Feb 2009.

[18] M. Froggatt and J. Moore, "High-spatial-resolution distributed strain measurement in optical fiber with Rayleigh scatter," *Appl. Opt.*, vol. 37, pp. 1735–1740, Apr 1998.

[19] W. Zhao and R. O. Claus, "Optical fiber grating sensors in multimode fibers," *Smart Materials and Structures*, vol. 9, p. 212, Mar 2000.

[20] B. Saleh and M. Teich, *Fundamentals of Photonics*. Wiley Series in Pure and Applied Optics, Wiley, 2007.

[21] L. Chen, S. Benjamin, P. Smith, and J. Sipe, "Ultrashort pulse reflection from fiber gratings: a numerical investigation," *J. Lightwave Technol.*, vol. 15, pp. 1503–1512, Aug 1997.

[22] J. Azaña and M. A. Muriel, "Study of optical pulses-fiber gratings interaction by means of joint time-frequency signal representations," *J. Lightwave Technol.*, vol. 21, p. 2931, Nov 2003.

[23] *FBGS - Draw Tower Gratings*. Available at `http://www.fbgs.com/home/`.

Chapter 4

Fiber optic sensors using long period gratings

4.1 Introduction

The discovery and exploitation of optical fiber gratings has had a growing impact on research and development of both fiber optic sensing and telecommunications applications [1]. Fiber gratings are intrinsic optical components allowing the control over the properties of the light which propagates through the fiber. Broadly speaking, optical fiber gratings consist of a periodic perturbation of the refractive index (RI) of the fiber core, and can be split into two distinct groups depending on the grating period. Widely described in the previous chapters, short period fiber gratings, also known as fiber Bragg gratings (FBGs), have a sub-micron period and couple light from the forward propagating mode to the backward counter-propagating mode [2]. This coupling occurs at a specific wavelength, known as Bragg wavelength, defined by the Bragg conditions, which are depending on both the period and RI of the propagating mode. Indeed, a change in either of these parameters, caused by a change in strain and/or temperature, results in a shift of the Bragg wavelength, setting the foundation for FBG-based sensors [3].

On the other hand, long period gratings (LPGs) have a periodicity typically in the range from 100 μm to 1 mm. LPGs act to couple light from the propagating core mode to the co-propagating cladding modes, producing a series of attenuation bands in the transmission spectrum, centered at discrete wavelengths [4]. These resonance wavelengths of the attenuation bands result to be sensitive to the local environment experienced by the fiber, making the LPGs a good candidate for fiber optics sensors [5].

In the first part of this chapter, a LPG has been used and applied as liquid level sensor, exploiting the potentials of the microwave photonics (MWP) filtering techniques, yet described in chapter 3. The fundamental concept behind the proposed method is based on the RI sensitivity of the LPG. The LPG has been cascaded with a high reflectivity FBG and the pair LPG-FBG has been employed to obtain the two taps of a MWP filter. When the liquid level surrounding the sensor increases, the LPG resonance shifts towards lower wavelengths and hence the magnitude of the tap related to the LPG grows, causing a gradual imbalance between the weights of the two taps of the MWP filter. This intensity imbalance causes, in turn, a step-wise reduction of the MWP filter visibility. By monitoring the latter, the measurement of the liquid level can be achieved.

In the second part of the chapter, a novel approach for simultaneous temperature and humidity sensing based on a half-coated LPG is proposed and demonstrated via experiments. Firstly, the LPG has been completely coated with humidity sensitive nanostructured polymeric thin films by layer-by-layer (LbL) nano assembly technique. The full-coated LPG has been exposed to relative humidity (RH) and temperature tests. Then, half of the coating has been chemically removed, yielding to the split of the main attenuation band into two separated contributions, presenting different behaviors for humidity and temperature. The experimental tests in temperature and RH have been repeated using the semi-coated LPG as sensing device, demonstrating the simultaneous measurement of both magnitudes using a single LPG.

This chapter is a result of a collaboration between UPVLC and UPNA.

4.2 LPGs fabrication and characteristics

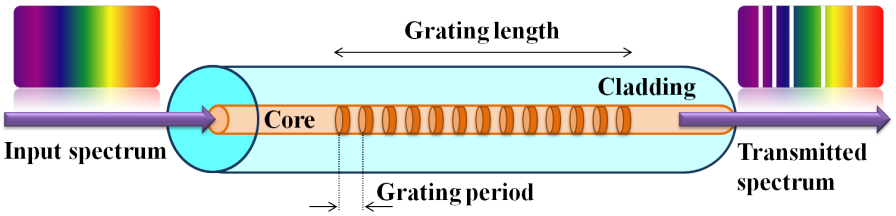

Figure 4.1: Schematic of a LPG.

A LPG is an optical fiber device consisting of a periodic modulation of the RI in the fiber core, with the period (Λ) of hundreds of micrometers. Such a structure couples the guided core mode to the co-propagating cladding modes at different resonant wavelengths (λ_i), resulting in several attenuation bands in the LPG transmission spectrum, as schematically depicted in Fig. 4.1. The form of the spectrum and the center wavelengths of the attenuation bands are sensitive to the period and length of the LPG and to the local surrounding environment: strain,

temperature, bending radius, liquid level and RI of the medium surrounding the LPG, among others [6].

According to the coupled mode theory, the phase matching condition depends on the difference in the effective RI of the core and cladding modes and on the LPG period [5], according to

$$\lambda_i = (n_{co\_eff} - n_{cl\_eff,i})\Lambda \tag{4.1}$$

being n_{co_eff} the effective RI of the core mode and $n_{cl\_eff,i}$ the effective RI of the i-th order cladding mode. Hence, changes in the external parameters surrounding the LPG can modify the grating period and/or the differential RI of the core and cladding modes. This way, the phase matching conditions, and hence the resonance wavelengths of the attenuation bands, also change. The sensitivity to a particular physical parameter depends on the fiber composition and on the order of the cladding mode to which the guided optical power is coupled, and hence varies from one attenuation band to another [5]. Besides, the LPG sensitivity to a particular measurand can be enhanced by suitably coating the grating with a specific layer [7–10].

The LPGs used to perform the tests proposed in this chapter have been fabricated using the point-by-point technique by means of an Argon-ion frequency doubled laser at a wavelength of 244 nm and a high precise translation stage with an accuracy of few nanometers. The laser beam, with 50 μm in diameter, has been focused onto the optical fiber to modify the RI of the core. The exposure time in each point has been kept constant along the total length of the grating. The LPGs have been fabricated by using optical fiber PS1250/1500 (from Fibercore Inc.), and the resultant grating parameters have been 464 μm for period and 4 cm for length, for the LPG applied as liquid level sensor, and 464 μm for period and 6 cm for length, for the LPG employed as RH and temperature sensor.

4.3 Liquid level sensor based on a LPG and MWP technique

As commented above, fiber optic sensors based on LPGs have attracted growing interests due to the fact that they are able to measure various physical parameters, such as RI, temperature, strain, bending and liquid level, amongst others. Different kinds of liquid level sensors based on such a fiber gratings were already proposed and demonstrated. For instance, in [11] a simple solution for liquid level sensing based on a single LPG was illustrated. The measurement of the liquid level was performed by evaluating the changes in the transmission spectrum of the LPG by means of an optical spectrum analyzer (OSA). Moreover, in [12] two identical LPGs were cascaded to form a Mach-Zehnder interferometer (MZI), in order to improve both measurement range and sensitivity. The part between the LPGs

was interrogated by means of a broadband source (BBS) and an OSA. In this way, the measurement was obtained by retrieving the shifts in the interference fringes of the transmission spectrum of the MZI. Also, in [13] a Michelson interferometer was fabricated by employing a LPG and by silvering the end facet of the fiber, in order to create a reflective mirror. The portion between the LPG and the reflective mirror was exposed to the liquid. Here too, a BBS together with an OSA were used and the changes in the interference fringes were monitored, showing good linearity and high sensitivity.

Analogously, excessively tilted grating structures were also investigated, presenting a mode coupling behavior similar to that observed for a LPG, and were employed as liquid level sensors [14, 15]. In this context, liquid level measurements were performed by examining the optical spectra of such structures by the use of a BBS and an OSA, showing lower temperature cross sensitivity than the LPG based liquid level sensor. However, the manufacturing of excessively tilted gratings results a complicated issue when compared with the more approachable LPGs fabrication process.

Here, an approach for interrogating a LPG-based liquid level sensor is proposed and validated via experiments. The fundamental concept behind the method is based on the RI sensitivity of the LPG together with a technique used to analyze MWP filters, which has been previously described in chapter 3. This is, to the best of our knowledge, the first demonstration of a LPG sensor interrogated with a radio-frequency (RF) based method.

4.3.1 Description of the method

The experimental setup of the liquid level sensing system is illustrated in Fig. 4.2. The signal from a continuous wave (CW) tunable laser source (TLS1) is mixed with the signal provided by another CW tunable laser source (TLS2), by means of a 3-dB coupler. Two polarization controllers (PCs) are placed after the optical sources to enhance the modulation efficiency. The signal from the 3-dB coupler is sent into an EOM and hence modulated with a microwave tone (10 MHz - 500 MHz) generated by a vector network analyzer (VNA). The modulated signal is sent into the sensing device through an optical circulator. The sensing device consists in a 4 cm-long LPG having periodicity of 464 μm, written in cascade with a 1 cm-long high reflectivity FBG. The signal from the TLS1 is set at the Bragg wavelength of the high reflectivity grating, while the signal provided by the TLS2 is set at one of the wavelength resonance of the LPG. In this way, these two signals will travel along two different optical paths. The modulated lightwave at the Bragg resonance will pass through the LPG, before to be reflected from the FBG and then reach the port 3 of the optical circulator (green path, L_1 in Fig. 4.2). Here a variable optical attenuator (VOA) is placed to control the magnitude of the Bragg reflected signal, in order to make it match as much as possible the weight of the tap related to the LPG. This is a key step for achieving a high visibility of the two-tap MWP filter (i.e. notch filter). On the other hand, the

signal at the LPG resonance will pass through the two gratings (red path, L_2); when crossing the LPG this signal will experience a huge attenuation. Finally, the light components from the two different optical paths are combined together and sent into a photo-detector (PD). The frequency response of the system is analyzed by monitoring the scattering parameter S_{21}, which relates the RF detected signal to the input modulating microwave signal. By analyzing the amplitude changes in the frequency response of the two-tap MWP filter so created, the liquid level can be retrieved as will be better explained afterwards.

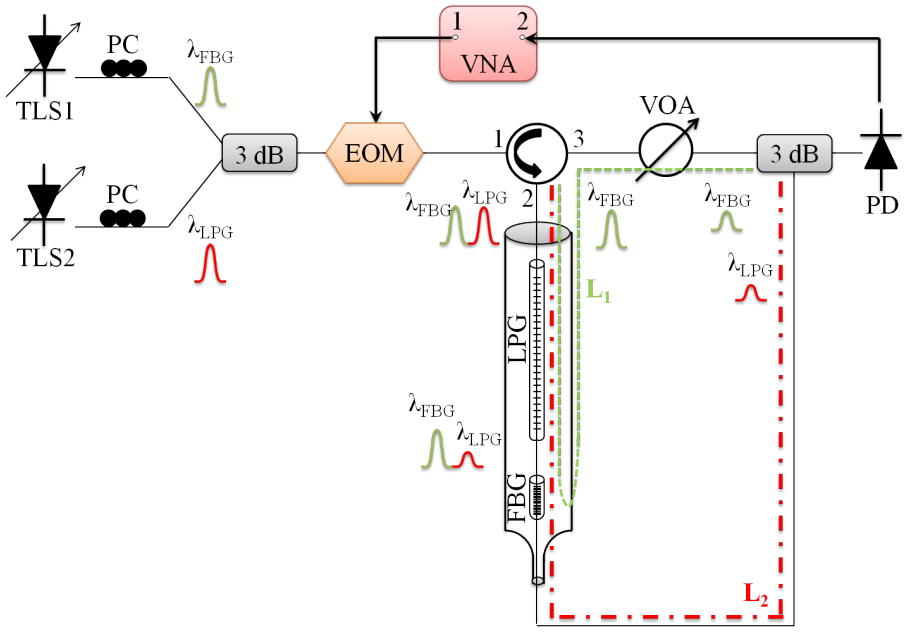

Figure 4.2: Experimental layout implemented to interrogate the LPG-based liquid level sensor. The operation principle is based on a technique used to analyze MWP filters.

To perform the liquid level measurements, the optical fiber containing the pair LPG-FBG is passed through the nozzle of a syringe and mounted in such a way that the LPG lay within a graduated region, as seen in Fig. 4.3. During the experiment, the liquid level is controlled with the aid of another syringe. The liquid used in the experimental measurements is water. The FBG fabricated in cascade with the sensing LPG has a dual purpose: the first function is to provide a second tap and hence allowing the formation of the two-tap MWP filter. The second function is the liquid temperature detection: this is used to compensate the temperature influence on the LPG wavelength shift.

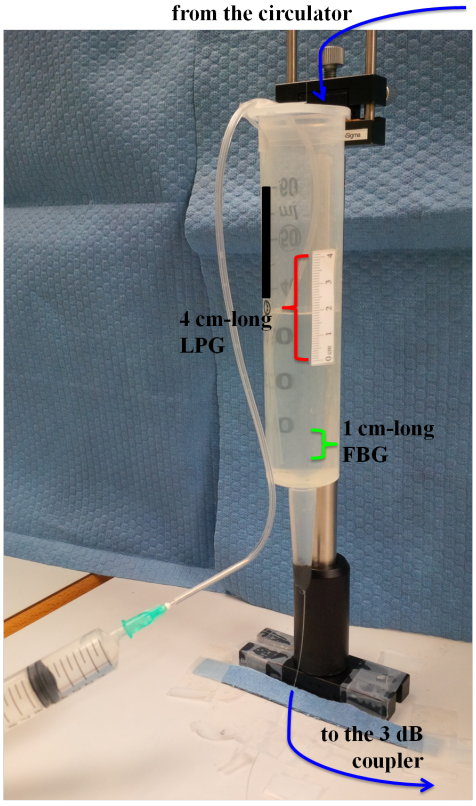

Figure 4.3: Picture representing the optical fiber containing the pair LPG-FBG used as liquid level sensor. The fiber is passed through the nozzle of a graduated syringe.

4.3.2 Experimental measurements and results

Once the liquid is surrounding the sensor, the first step is the tuning of the TLS1 at the FBG resonance, as schematically described in Fig. 4.4, while the other laser is kept off. When the TLS1 is step-wise scanned, the relation between the laser wavelength and the FBG resonance can be described as follows: Fig. 4.4(a) and Fig. 4.4(e) illustrate the case in which the laser wavelength is far from the FBG central resonance. In such a case, the signal passes through the grating following the optical path L_2, reaching the coupler and then the PD. This tap is photo-detected and a continuous amplitude signal is displayed at the VNA. The case in which the laser wavelength is close to the FBG resonance but just below (above) the FBG central wavelength is illustrated in Fig. 4.4(b) (Fig. 4.4(d)). Under these circumstances, part of the laser signal is back-scattered by the grating while the other part passes through the FBG. These two taps follow different optical paths before being re-combined at the 3-dB coupler and then photo-detected. These components of the same laser signal are mixed under coherent basis: this is

because the delay between the taps is smaller than the source coherence time. As a consequence, an interference "noisy" trace is displayed at the VNA.

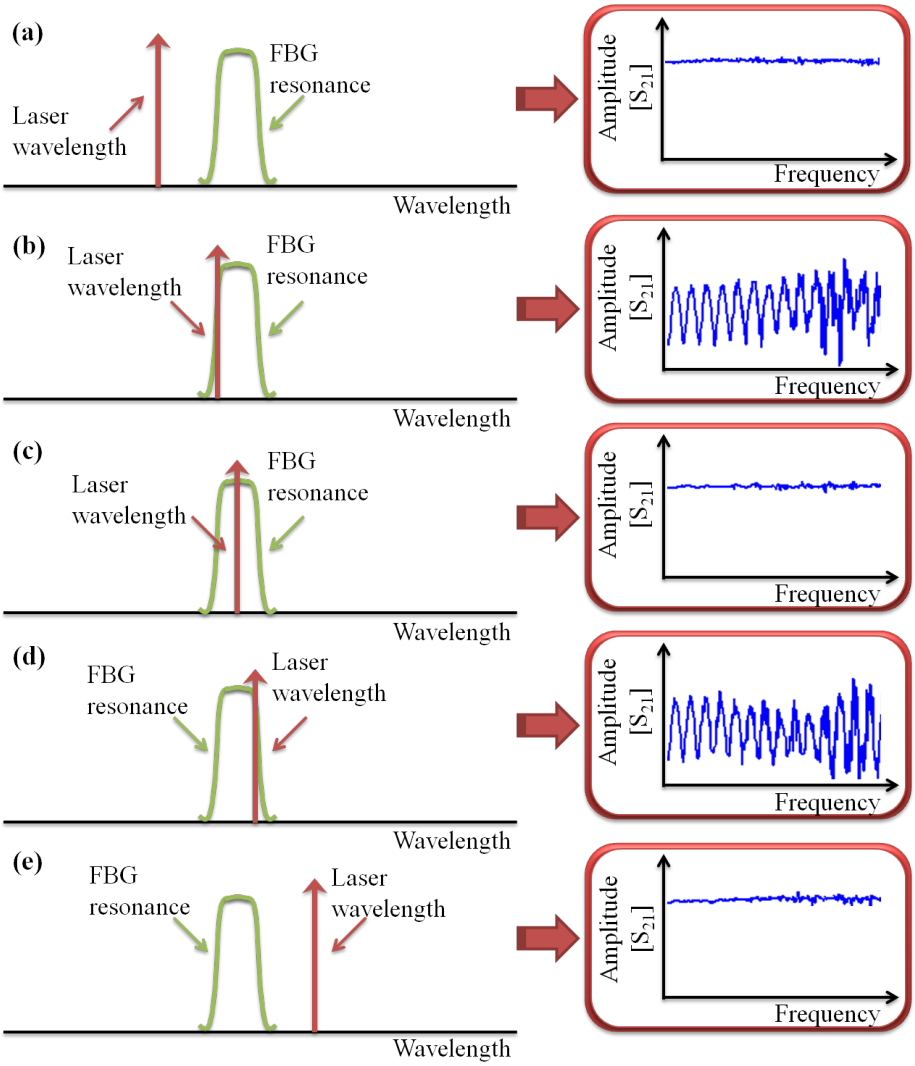

Figure 4.4: Schematic representing the wavelength tuning of TLS1 at the FBG resonance. (a) and (e) The laser wavelength is far from the FGB resonance: this signal completely passes through the FBG and hence a continuous line is visualized at the VNA. (b) and (d) The laser wavelength is close to the FBG resonance: part of the light is back-reflected while the other part passes through the FBG, as a result an interference signal is displayed at the VNA. (c) The laser wavelength is set at the FBG central resonance: the signal is completely back-reflected and a line is displayed at the VNA.

In the last case, when the laser wavelength is set at the FBG central resonance, as depicted in Fig. 4.4(c), this signal is entirely back-reflected by the grating and then reaches the coupler following the optical path L_1. Hence, a continuous line is visualized at the VNA. Following this procedure, the signal from the TLS1 is set at the Bragg resonance of the FBG, as in the case of Fig. 4.4(c). As the Bragg resonance of the FBG has been previously characterized at room temperature of 20°C, resulting in 1532.8 nm, and taking into account the FBG temperature coefficient, which is 10 pm/°C, the liquid temperature can be calculated.

Now, the wavelength of the TLS2 is adjusted at the LPG resonance and the magnitude of the tap related to the FBG reflection is opportunely set via VOA (see Fig. 4.2) in order to match as much as possible the magnitude of the tap at the LPG resonance. This is because by achieving equal amplitudes of the two taps, a large MWP filter visibility is obtained [16]. The liquid level measurements are performed by tracking the changes in the MWP filter visibility, therefore in order to get better accuracy, the number of "dips" of the MWP filter can be suitably controlled by setting the free spectral range (FSR) of the MWP filter. This periodic spectral characteristic is inversely proportional to the time spacing T between taps, according to [16]

$$FSR = \frac{1}{T} = \frac{c}{n_g|L_1 - L_2|} \tag{4.2}$$

where n_g is the group refractive index of the fiber and c is the speed of light in vacuum. According to (4.2), the FSR of the two-tap MWP filter (and hence the number of dips) can be opportunely chosen by tailoring the difference between optical paths $|L_1 - L_2|$.

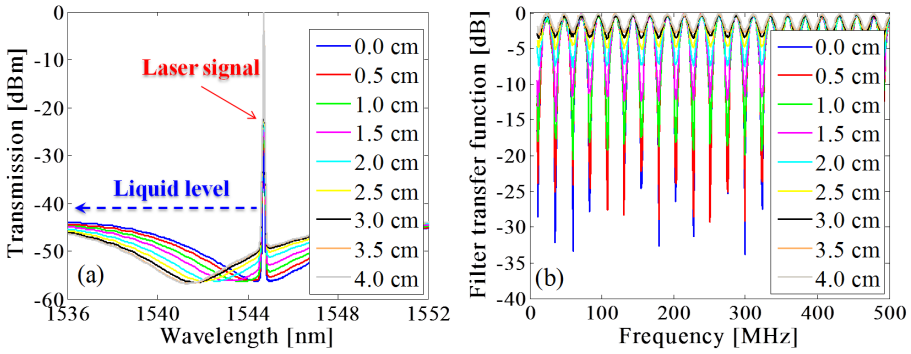

Figure 4.5: (a) Measured spectra representing the LPG resonance shift for different values of liquid level. Measurements performed using water. (b) Two-tap MWP filters obtained for different values of liquid level. When the liquid level increases the notch filter visibility decreases.

When the liquid level increases, the LPG resonance shifts towards lower wavelengths as measured and shown in Fig. 4.5(a). This shift represents the same behavior corroborated in other works, such as [17] and occurs when the RI of the liquid is near 1.33 (mostly water based solutions). As it was demonstrated in [11], the wavelength shift between LPG resonance peak in air and LPG resonance peak in liquid is very low when the RI of the liquid is lower than 1.40. Due to this, both peaks are overlapped during the liquid level test, and only a wavelength shift of few nanometers appears, as experimentally corroborated in our test and shown in Fig. 4.5(a). When this occurs, the magnitude of the tap related to the LPG, grows causing a gradual imbalance between the amplitudes of the two taps of the MWP filter. This intensity imbalance causes, in turn, a step-wise reduction of the MWP filter visibility, as illustrated in Fig. 4.5(b). By monitoring the latter, the measurement of the liquid level can be achieved. For each liquid level, the values of the 21 dips represented in Fig. 4.5(b) have been averaged in order to obtain the relationship between the MWP filter visibility and the liquid level.

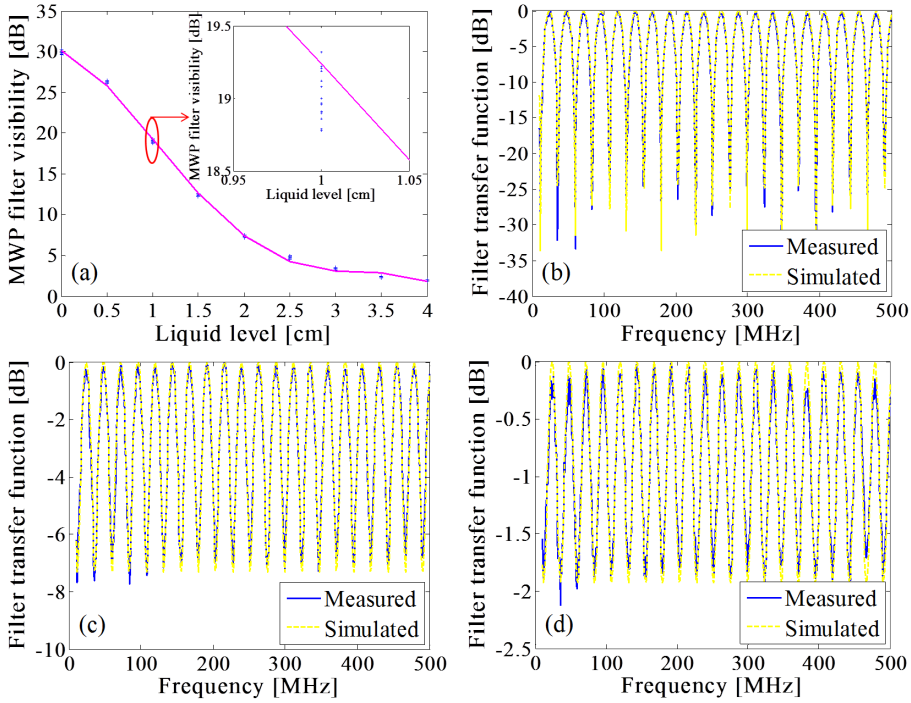

Figure 4.6: (a) Relationship between the MWP filter visibility and the liquid level. Inset: Zoom representing the measurements collected for a given liquid level. The set of data shows that the sensor has good stability and repeatability. Simulated and measured MWP filter responses for different values of liquid level: (b) 0 cm. (c) 2 cm. (d) 4 cm.

Several sets of experimental data have been collected in order to show how good the stability and repeatability of the sensor are. The relationship between the MWP filter visibility and the liquid level at the sensor is depicted in Fig. 4.6(a), from which it is possible to see as the notch amplitude decreases near exponentially with the liquid level. Furthermore, the inset in Fig. 4.6(a) proves that the continuous liquid level sensor proposed has very good performance in terms of stability and repeatability, with a measured standard deviation of 0.52 dB. The measurements in Fig. 4.6(a) also show a quasi-linear range in the initial region of the liquid level sensor, yielding a sensitivity of -12.71 dB/cm.

Also, a set of simulations has been performed and compared to the experimental data in order to prove the feasibility of the method. The simulations have been implemented for different values of liquid level; the simulated (yellow dashed lines) and measured (blue continuous lines) MWP filter responses for liquid level of 0 cm, 2 cm and 4 cm are represented in Fig. 4.6(b), Fig. 4.6(c) and Fig. 4.6(d), respectively. These latter graphics show that the experimental results are consistent with the theoretical simulations, proving the feasibility of the pair FBG-LPG as a continuous liquid level sensor.

Besides, it is worth noticing that if the temperature of the liquid is different from the room temperature, this provokes a further wavelength shift of the LPG resonance. However, as previous mentioned, the temperature of the liquid is evaluated by the step-wise tuning of the TLS1 wavelength at the FBG resonance (which is shifted due to the liquid temperature change). Once the temperature of the liquid is known and based on the LPG temperature coefficient, the temperature influence on the LPG wavelength shift can be compensated by setting the signal provided by the TLS2 at the new LPG resonance. This way, once the TLS1 wavelength is set at the FBG resonance and the TLS2 is set at the LPG resonance, the two-tap MWP filters are retrieved for different liquid levels and the measurements are performed using the procedure described above.

4.4 RH and temperature sensor based on half-coated LPG

In this section, a novel approach for simultaneous humidity and temperature sensing based on a half-coated LPG, is described and demonstrated via experiments. To our knowledge, this is the first time that a single LPG is partially coated to develop a sensing device, allowing simultaneous response for two different external magnitudes. In recent years, techniques have been implemented for two or more magnitudes sensing, by employing more than one grating along the optical fiber [18, 19]. Also, a theoretical study has been proposed allowing the feasibility of partially coated LPG for sensing applications [20].

For these experiments, a LPG having period Λ=464 μm and length L_{LPG}=6 cm has been coated with polymeric thin films using the LbL assembly method [21]. The deposition process has been repeated 40 times, obtaining a final coating of 40 bilayers onto the LPG surface. The building performance has been monitored, recording the transmission spectrum after each bilayer formation, using a BBS and an OSA. The evolution of the spectrum is plotted in Fig. 4.7, which shows as the coating causes a variation in the external RI, hence modifying both the spectrum and the attenuation bands of the LPG. As a consequence of this, the original main attenuation band is blue-shifted as the nanostructured thin film is deposited. Once the deposition process is over, the coated LPG has been left to rest for 24 h at room conditions. After this time, necessary for the coating stabilization and drying, the main attenuation band is centered in 1515 nm.

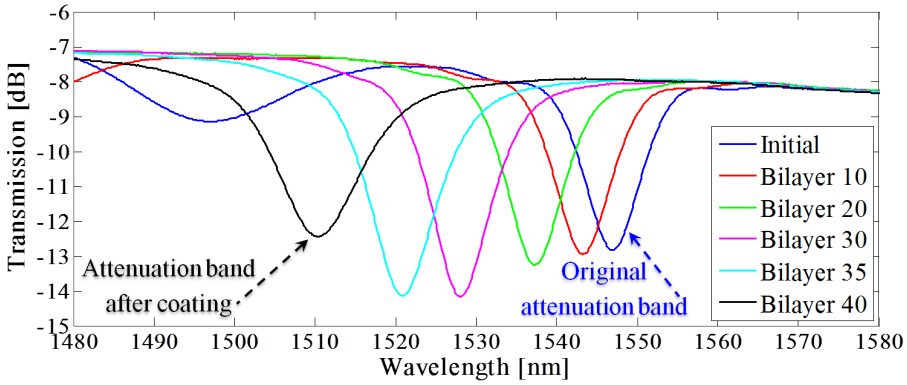

Figure 4.7: Evolution of the sensing LPG spectrum for the main attenuation band during the LbL assembly process.

The experimental setup in Fig. 4.9(a) has been used for the RH and temperature tests. Fig. 4.9(b) schematically illustrated the sensing LPG after the full coating process. The totally coated LPG has been submitted to several RH cycles by means of a programmable climatic chamber. The humidity tests have been carried out following a constant slope from 80% RH to 20% RH, then the RH variation has been inverted from 20% RH to 80% RH. This up-and-down humidity profile has been repeated 3 times, while temperature has been kept constant at 25°C. The transmission spectrum of the full-coated LPG shows a wavelength shift pattern of the attenuation band, due to the swelling/de-swelling properties of the polymeric coating depending on the RH conditions [22]. This effect provokes a huge variation of the external RI, which modifies, in turn, the resonance modes and their attenuation bands, as illustrated in Fig. 4.8(a) The RH text shows that, as the RH values decreases, the peak presents a red shift, ranging from 1513 nm for 80% RH to 1517.7 nm for 20% RH. Analogously, the peak returns at 1513 nm when the RH comes back to 80% RH. These patterns has been observed for several

RH cycles, obtaining a sensitivity ratio of -81.61 pm/%RH and a maximum peak wavelength shift of $\Delta\lambda_{max}$= 4.7 nm.

After that, the full-coated LPG has been exposed to temperature values ranging from 15°C to 35°C at constant RH. This is just a preliminary test for measuring and characterizing the LPG intrinsic temperature dependence [5]. The results are depicted in Fig. 4.8(b), showing a linear behavior in the mentioned temperature range, yielding a sensitivity of -398.57 pm/°C and maximum wavelength shift of $\Delta\lambda_{max}$= 7.8 nm.

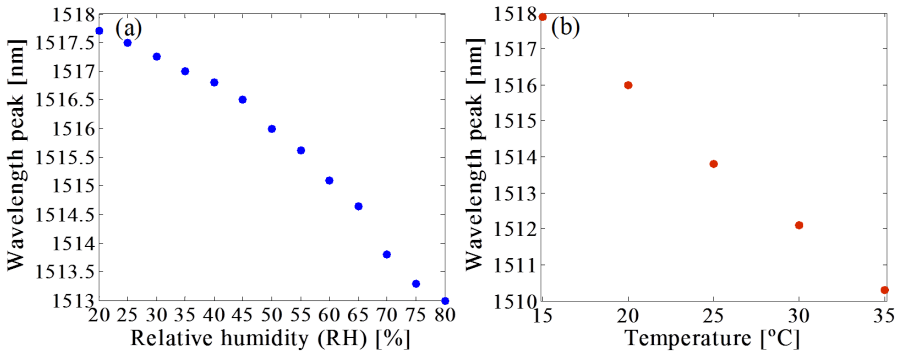

Figure 4.8: Evolution of the wavelength peak of the main attenuation band in the case of the full-coated LPG for: (a) RH variation from 20% to 80% and (b) temperature variation from 15°C to 35°C.

Thereafter, the polymeric LPG coating has been chemically removed in part. This removing process has been step-wise carefully made so as not to remove more than 50% of the coating according to the theoretical study [20]. As a result of this, a semi-coated LPG has been obtained as schematically depicted in Fig. 4.9(c). After the chemical removing treatment, the half-coated LPG has been cleaned and rinsing in several steps with ultra-pure water.

The transmission spectrum of the new sensing device has been recorded to observe the semi-coated effects: the main attenuation band has been split into two contributions, as shown in Fig. 4.10. On one hand, the coated LPG contribution remains, but its magnitude (optical attenuation in intensity) has been significantly lowered due to the reduction of the coating length along the grating. On the other hand, a second attenuation band appears because of the chemical removing process. As expected, the new attenuation band corresponds to the half uncoated grating area, and it is centered in 1547 nm, in the same spectral wavelength of the original uncoated LPG attenuation band (see Fig. 4.7). Both contributions have similar weights in magnitude due to their lengths which are approximately half of the total length of the sensing LPG, in agreement with the theoretical analysis [20].

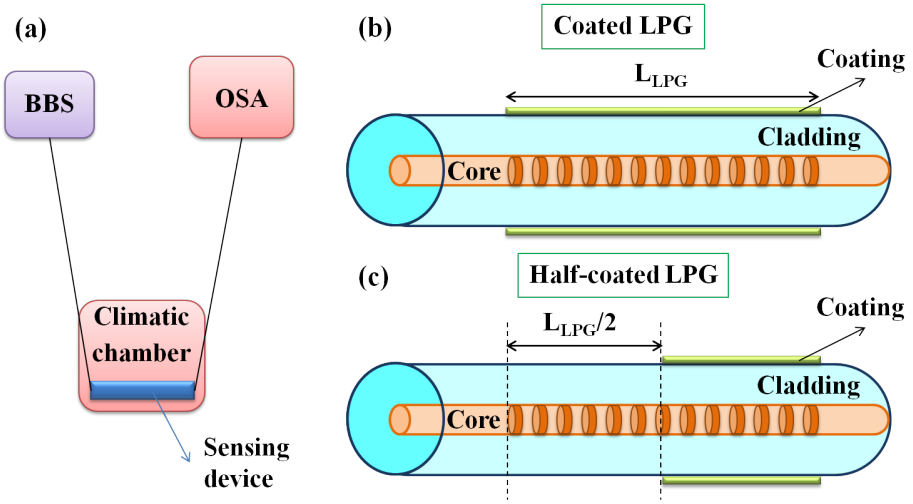

Figure 4.9: (a)Experimental setup implemented to monitor the LPG-based sensors. (b) Schematic of the full-coated LPG. (c) Schematic of the half-coated LPG obtained by chemically removing part of the LPG coating in Fig. 4.9(b).

The half-coated LPG has been submitted to the RH and temperature cycles at the same previous conditions and the optical responses have been monitored. The peak of the attenuation band related to the coated part shifts in wavelength from 1515.6 nm for 20% RH to 1511.5 for 80% RH, as shown in Fig. 4.11(a), while the wavelength peak shift is depicted in Fig. 4.11(b) (black dots). The data shows a sensitivity of -63.23 pm/%RH and a maximum peak wavelength shift of $\Delta\lambda_{max}$= 4.1 nm, in agreement with the previous results.

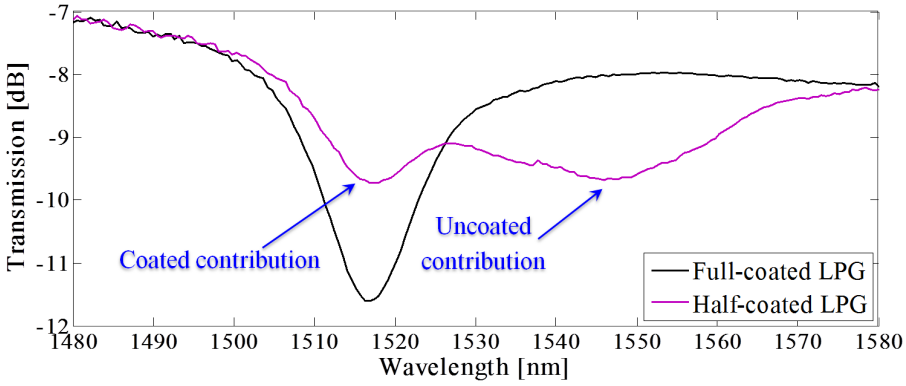

Figure 4.10: Transmission spectra of the full-coated LPG (black curve) and the half-coated LPG (purple curve).

On the contrary, the attenuation band attributable to the original uncoated LPG, presents an opposite behavior: as the RH increases, the peak shifts to higher wavelength, from 1546.2 nm for 20% RH to 1549.3 nm for 80% RH, as illustrated in Fig. 4.11(a). These evolution peaks are represented in Fig. 4.11(a) (green dots), yielding a sensitivity ratio of 55.22 pm/%RH and a maximum peak wavelength shift of $\Delta\lambda_{max}$= 3.1 nm. These results have been corroborated after multiple RH tests, showing high repeatability.

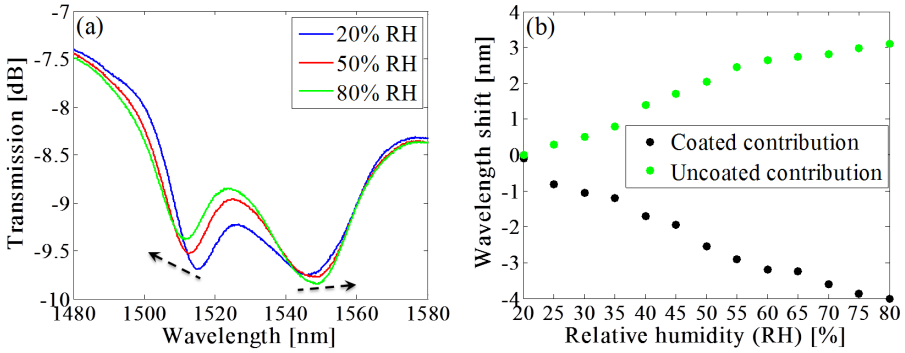

Figure 4.11: (a) Transmission spectra of the semi-coated LPG for RH changes. (b) Wavelength shift of the different attenuation bands during the RH test: coated LPG contribution (black dots) and uncoated LPG contribution (green dots).

Then, the optical response of the semi-coated LPG has been monitored under a temperature test, ranging from 25°C to 85°C, while keeping RH constant at 30%RH. Both peak contributions present a linear behavior, as the coated LPG case. When temperature increases, both contribution peaks shift towards lower wavelengths, as shown in Fig. 4.12(a) and Fig. 4.12(b). Both coated and uncoated contributions show very high sensitivity: -410.66 pm/°C and -405.09 pm/°C, respectively.

Once the humidity and temperature tests have been performed and against the backdrop of the positive results achieved so far, the possibility to employ the half-coated LPG for simultaneous RH and temperature measurements has been investigated. The optical response of the semi-coated LPG as RH and temperature sensor can be characterized as a two equations system for two parameters [18], given by

$$\begin{bmatrix} \Delta\lambda_{LPG} \\ \Delta\lambda_{coat} \end{bmatrix} = \begin{bmatrix} k_{Temp\_LPG} & k_{RH\_LPG} \\ k_{Temp\_coat} & k_{RH\_coat} \end{bmatrix} \begin{bmatrix} \Delta Temp \\ \Delta RH \end{bmatrix} \tag{4.3}$$

being k_{Temp_coat}= -410.66 pm/°C and k_{Temp_LPG}= -405.09 pm/°C the temperature sensitivities for the coated and uncoated contributions, respectively, while

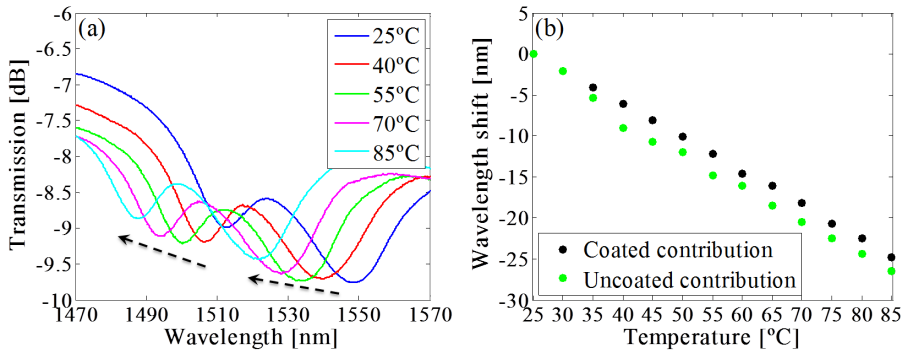

Figure 4.12: (a) Transmission spectra of the semi-coated LPG for temperature changes. (b) Wavelength shift of the different attenuation bands during the temperature test: coated LPG contribution (black dots) and uncoated LPG contribution (green dots).

k_{RH_coat}= -63.23 pm/%RH and k_{RH_LPG}= 55.22 pm/%RH the humidity sensitivities for the coated and uncoated contribution, respectively. The wavelength peaks shift for the coated and uncoated LPG contributions are $\Delta\lambda_{coat}$ and $\Delta\lambda_{LPG}$, respectively, while the temperature and RH variations are $\Delta Temp$ and ΔRH, respectively.

From (4.3) and by the theory of matrix operations [18], it can be written as

$$\begin{bmatrix} \Delta Temp \\ \Delta RH \end{bmatrix} = \frac{1}{Det} \begin{bmatrix} k_{RH\_coat} & -k_{RH\_LPG} \\ -k_{Temp\_coat} & k_{Temp\_LPG} \end{bmatrix} \begin{bmatrix} \Delta\lambda_{LPG} \\ \Delta\lambda_{coat} \end{bmatrix} \tag{4.4}$$

being Det the matrix determinant containing the RH and temperature sensitivities (Det= $k_{Temp\_LPG} \cdot k_{RH\_coat}$ - $k_{RH\_LPG} \cdot k_{Temp\_coat}$). Hereinafter, the final expression for the half-coated LPG sensor, can be expressed as

$$\begin{bmatrix} \Delta Temp \\ \Delta RH \end{bmatrix} = 20.70801 \begin{bmatrix} -0.06323 & -0.05522 \\ 0.41066 & -0.40509 \end{bmatrix} \begin{bmatrix} \Delta\lambda_{LPG} \\ \Delta\lambda_{coat} \end{bmatrix} \tag{4.5}$$

Finally, the simultaneous temperature and RH sensing system described by (4.5) has been experimentally validated. To do so, the semi-coated LPG has been firstly submitted to a humidity variation from 20%RH to 80%RH at a constant temperature of 25°C. Then, the sensor has been tested under a temperature variation ranging from 25°C to 80°C, while keeping the RH at a constant value of 40%RH. The measurements of the position of both optical peaks (coated and uncoated contributions) have been monitored and mathematically processed by means of (4.5) and the results obtained are illustrated in Fig. 4.13.

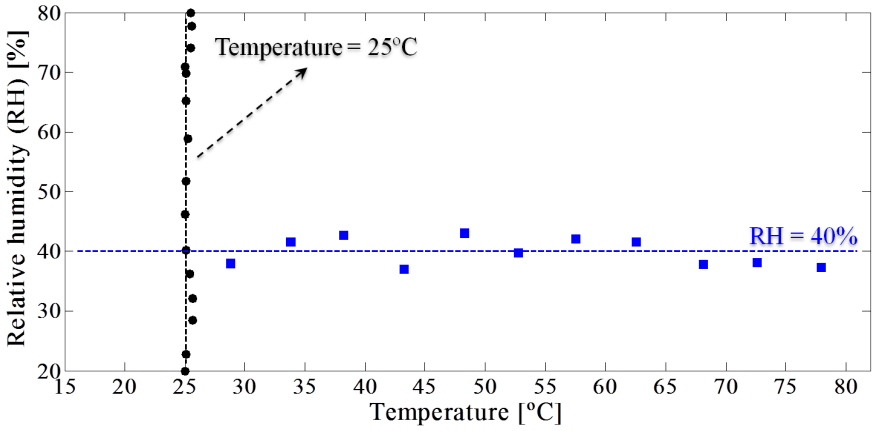

Figure 4.13: Half-coated LPG response from (4.5) for RH variations at constant temperature (black dots) and for temperature variations at constant RH (blue squares).

The experimental results show an excellent fit in temperature for any RH variations in the range from 20%RH to 80%RH. The standard deviation obtained in this case is 0.244°C. On the other hand, the RH values recorded for different values of temperature in the range from 25°C to 80°C show a higher standard deviation of 2.352%RH. This difference in terms of standard deviation is attributable to the performance of the climatic chamber and to the intrinsic instability of the RH as temperature is changed. Nevertheless, the wavelength-based measurement system proposed have succeeded in the extraction of the temperature and RH measurements from the absolute wavelengths of the two adjacent peaks obtained from a single sensor based on a half-coated LPG.

4.5 Conclusions

In this chapter, a new scheme for fiber optic liquid level sensor based on a LPG and MWP filtering technique has been proposed and experimentally validated. The measurement system is based on the principle of operation of a MWP filter, in particular on the measurement of the amplitude of the electrical S_{21} scattering parameter that characterizes the filter transfer function. A simple layout is used to interrogate a 4 cm-long LPG, written in cascade with a high reflectivity FBG. The fundamental concept behind the proposed method is based on the RI sensitivity of the LPG. This is, to the best of our knowledge, the first demonstration of a LPG sensor interrogated with a RF based scheme. In fact, the liquid level measurements have been performed by using RF devices, i.e. EOM and PD, with a modest bandwidth of only 500 MHz, without using any additional wavelength scanned system.

The sensing features of the LPG-based liquid level sensor have been theoretically and experimentally validated, proving that all measured data are consistent with the theoretical simulations. Several sets of experimental measurements have been collected in order to prove the stability and repeatability of the sensor. The liquid level measurements have been performed by tracking the changes in the MWP filter visibility, yielding a sensitivity of -12.71 dB/cm and a standard deviation of 0.52 dB. The measurement range of 4 cm is limited by the physical length of the LPG but it may certainly be enhanced by fabricating a longer grating. Moreover, although the use of a VNA may enhance the system complexity and expense, the instrumentation required could be simplified by replacing the VNA with an oscillator and a device able to analyze the magnitude response of the MWP filter generated. Besides, the FSR of the two-tap MWP filter can be suitably chosen by opportunely tailoring the optical path difference of the configuration. By judiciously selecting an appropriate value for the FSR, the operating frequency range of the system can be further reduced below the 500 MHz. This will lower the system cost and complexity and also improve the interrogation speed.

The proposed continuous liquid level sensor presents the advantages of easy and well-established fabrication procedure, good repeatability and stability. Furthermore, the simple scheme investigated proves to be intrinsically robust against environmental changes and easy to reconfigure, and hence results as a very good candidate for several commercial and industrial applications.

Besides, a temperature and humidity sensor based on a half-coated LPG has been presented. Firstly, the variation of the optical response of a LPG has been studied when a polymeric LbL overlay was built-up onto the cladding. Then, half of the LbL coating has been chemically removed. The half-coated LPG provided a split of the attenuation band observed in the full-coated LPG into two components: one for the coated section and the other for the uncoated part of the LPG. This device has been also exposed to humidity and temperature cycles, and the optical response has been studied. Both attenuation bands presented wavelength shift as the RH changes. The peak related to the coated contribution had a similar behavior than the full-coated LPG. In contrast, the other peak presented an opposite shift variation. The LPG-based sensor has been also characterized under different temperature conditions. The experimental results have been analyzed, obtaining a dual-wavelength sensing mechanism based on the shifts of both peaks. The dual-wavelength based measurements provided a simultaneous monitoring of RH and temperature, with sensitivity ratios of -63.23 pm/%RH and -410.66 pm/°C for the attenuation band corresponding to the coated contribution, and 55.22 pm/%RH and -405.09 pm/°C for the attenuation band corresponding to the uncoated grating.

This novel, simple and cost-efficient approach could be applied in many coated LPG based sensors with the purpose to measure more than one magnitude at a time. Besides it could be a good alternative to the cascaded-LPGs sensing systems where the use of at least two gratings is required to simultaneously monitor two different parameters.

Bibliography

[1] P. S. Russell, J.-L. Archambault, and L. Reekie, "Fibre gratings," *Physics World*, vol. 6, pp. 41–6, Oct 1993.

[2] T. Erdogan, "Fiber grating spectra," *J. Lightwave Technol.*, vol. 15, pp. 1277–1294, Aug 1997.

[3] A. Kersey, M. Davis, H. Patrick, M. Leblanc, K. Koo, C. Askins, M. Putnam, and E. Friebele, "Fiber grating sensors," *J. Lightwave Technol.*, vol. 15, pp. 1442–1463, Aug 1997.

[4] V. Bhatia and A. M. Vengsarkar, "Optical fiber long-period grating sensors," *Opt. Lett.*, vol. 21, pp. 692–694, May 1996.

[5] S. James and R. Tatam, "Optical fibre long-period grating sensors: characteristics and application," *Measurement Science and Technology*, vol. 14, pp. R49–R61, Jan 2003.

[6] V. Bhatia, "Applications of long-period gratings to single and multi-parameter sensing," *Opt. Express*, vol. 4, pp. 457–466, May 1999.

[7] J. M. Corres, I. del Villar, I. R. Matias, and F. J. Arregui, "Fiber-optic pH-sensors in long-period fiber gratings using electrostatic self-assembly," *Opt. Lett.*, vol. 32, pp. 29–31, Jan 2007.

[8] X. Wei, T. Wei, H. Xiao, and Y. Lin, "Nano-structured Pd-long period fiber gratings integrated optical sensor for hydrogen detection," *Sensors and Actuators B: Chemical*, vol. 134, no. 2, pp. 687–693, 2008.

[9] D. Viegas, J. Goicoechea, J. M. Corres, J. L. Santos, L. A. Ferreira, F. M. Araújo, and I. R. Matias, "A fibre optic humidity sensor based on a long-period fibre grating coated with a thin film of SiO2 nanospheres," *Measurement Science and Technology*, vol. 20, p. 034002, Feb 2009.

[10] M. Konstantaki, A. Klini, D. Anglos, and S. Pissadakis, "An ethanol vapor detection probe based on a ZnO nanorod coated optical fiber long period grating," *Opt. Express*, vol. 20, pp. 8472–8484, Apr 2012.

[11] S. Khaliq, S. W. James, and R. P. Tatam, "Fiber-optic liquid-level sensor using a long-period grating," *Opt. Lett.*, vol. 26, pp. 1224–1226, Aug 2001.

[12] H. Fu, X. Shu, A. Zhang, W. Liu, L. Zhang, S. He, and I. Bennion, "Implementation and characterization of liquid-level sensor based on a long-period fiber grating Mach-Zehnder interferometer," *Sensors Journal, IEEE*, vol. 11, pp. 2878–2882, Nov 2011.

[13] H. Xue, Z. Xu, H. Chen, Y. Yang, J. You, J. Yan, H. Fu, and D. Zhang, "Continuous liquid level sensor based on a reflective long period fiber grating interferometer," *Measurement Science and Technology*, vol. 26, no. 3, p. 037001, 2015.

[14] C. Mou, K. Zhou, Z. Yan, H. Fu, and L. Zhang, "Liquid level sensor based on an excessively tilted fibre grating," *Optics Communications*, vol. 305, pp. 271–275, Sep 2013.

[15] Z. Yan, C. Mou, Z. Sun, K. Zhou, H. Wang, Y. Wang, W. Zhao, and L. Zhang, "Hybrid tilted fiber grating based refractive index and liquid level sensing system," *Optics Communications*, vol. 351, pp. 144–148, Sep 2015.

[16] J. Capmany, J. Mora, I. Gasulla, J. Sancho, J. Lloret, and S. Sales, "Microwave photonic signal processing," *J. Lightwave Technol.*, vol. 31, pp. 571–586, Feb 2013.

[17] Y. Huang, B. Chen, G. Chen, H. Xiao, and S. U. Khan, "Simultaneous detection of liquid level and refractive index with a long-period fiber grating based sensor device," *Measurement Science and Technology*, vol. 24, p. 095303, Jul 2013.

[18] D. Viegas, M. Hernaéz, J. Goicoechea, J. Santos, F. Araújo, F. Arregui, and I. Matias, "Simultaneous measurement of humidity and temperature based on an SiO2-nanospheres film deposited on a long-period grating in-line with a fiber Bragg grating," *Sensors Journal, IEEE*, vol. 11, pp. 162–166, Jan 2011.

[19] S. W. James, S. Korposh, S.-W. Lee, and R. P. Tatam, "A long period grating-based chemical sensor insensitive to the influence of interfering parameters," *Opt. Express*, vol. 22, pp. 8012–8023, Apr 2014.

[20] J. Bao, P. Cheng, H. Zhao, J. Wang, and L. Wu, "Spectral characteristics of a two-section multilayer long-period fiber grating sensor," *Optik - International Journal for Light and Electron Optics*, vol. 125, pp. 4689–4693, Sep 2014.

[21] X. Zhang, H. Chen, and H. Zhang, "Layer-by-layer assembly: from conventional to unconventional methods," *Chem. Commun.*, vol. 14, pp. 1395–1405, 2007.

[22] K. E. Secrist and A. J. Nolte, "Humidity swelling/deswelling hysteresis in a polyelectrolyte multilayer film," *Macromolecules*, vol. 44, pp. 2859–2865, Mar 2011.

Chapter 5

Improving the signal response of BOTDA systems by the aid of fiber Bragg gratings

5.1 Introduction

For over two decades, Brillouin distributed optical fiber sensors have gained increasing interest because of their potential to perform distributed strain and temperature monitoring over several tens of kilometers with cm-sized spatial resolution [1, 2]. Moreover, due to their precision and high strain/temperature resolution, Brillouin-based fiber sensors can find applications in different areas such as environmental monitoring, civil structures, aerospace and geotechnical engineering, amongst others.

The first works performing strain and temperature sensing based on Brillouin scattering (BS) were carried out at the end of the XX$^{\text{th}}$ century [3, 4]. Since these original publications, Brillouin sensing has turned out to be a fascinating research field. The evidence of BS performance in a distributed fashion is based on stimulated Brillouin scattering (SBS), so called Brillouin optical time domain analysis (BOTDA), which is based on the interaction of a high power pulsed pump with a counter-propagating continuous-wave (CW) probe signal. The sensor performance is given by the signal-to-noise ratio (SNR) of the measurements, which is basically dictated by the sensor amplitude response. This response depends on the input pump and probe powers, the spatial resolution and the fiber length. Hence, for very long sensing lengths, the sensor response and consequently the SNR are significantly reduced, setting a huge limitation to the sensor performance [5].

One important limitation on the sensor response in distributed optical fiber sensing based on BS is related to the maximum pump and pulse powers that can be launched into the sensing fiber, to avoid the onset of nonlinear effects. This evidences the presence of a trade-off between spatial resolution and maximum sensing length. Some methods have been developed to partially overcome this trade-off and to enhance the Brillouin interaction along the sensing element, and consequently, to increase the optical power reaching the receiver. For instance, optical pulse coding uses pulse sequence to enhance the total pump power while the corresponding signal is retrieved by a post-processing scheme [6, 7]. Also, distributed Raman amplification has been used to amplify the Brillouin pump and probe signals during their propagation along the sensing fiber [8]. Significant improvements have been achieved when these two systems are mixed together [9].

In this chapter, an alternative approach to improve the response and performance of Brillouin distributed fiber sensors will be demonstrated. The technique requires the generation of pump and probe signal spread over different spectral components. While the power of each frequency component is still limited by the onset of nonlinear effects, the total amount of power launched into the sensor can be significantly increased, so as leading to a sensor response improvement. In addition, a frequency dependent delay has to be applied to the pump components to avoid nonlinear cross-interaction. An experiment have been performed as a proof-of-concept, based on two arrays of fiber Bragg gratings (FBGs) acting as frequency dependent delayer element. Experimental measurements show the capability of the method to improve the SNR, while the detrimental nonlinear effects are not observed in spite of increased pump and probe powers.

This chapter is a result of a collaboration between UPVLC and EPFL during a stay at GFO in Switzerland.

5.2 Principle of operation

In this section, the back-scattering phenomenon taking place within optical fibers will be briefly explained. Following, emphasis will be placed on the physics and working principle of spontaneous and stimulated Brillouin scattering. Finally, the theory and operation principle of BOTDA and its use for distributed sensing will be provided.

5.2.1 Spontaneous and stimulated scattering in optical fibers

To understand how distributed sensors work as well as the working principle of BOTDA, emphasis must be placed on the back-scattering phenomena taking place within an optical fiber. When an electromagnetic wave is launched into an optical fiber, the light will be spectrally redistributed by different mechanisms in the form of Rayleigh, Brillouin, Raman and Rayleigh-wing scatterings, as schematically depicted in Fig. 5.1 [10]. By definition, the components of the scattered light that

are down-shifted are known as Stokes components while those components of the scattered light that are up-shifted are referred as anti-Stokes components.

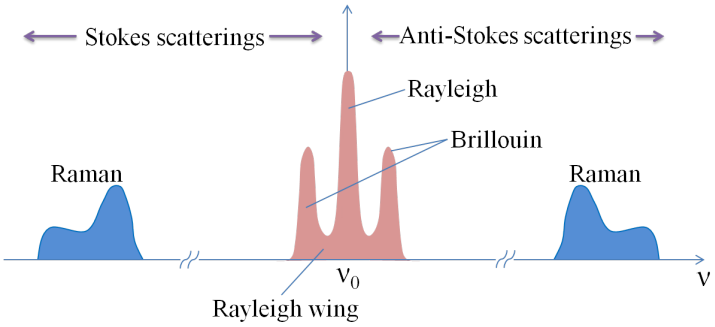

Figure 5.1: Schematic illustration of typical spontaneous scattering spectrum.

The four different scattering processes illustrated in Fig. 5.1 are briefly described hereinafter [10]. Rayleigh scattering is a linear scattering process in that the scattered power results proportional to the incident power. The electromagnetic wave propagating in the fiber core interacts with the scattering centers (particles). In optical fibers, as silica impurities and enhancing additives have dimensions well below the wavelength of the light, these interaction give raise to a partial reflection that can be detected and interpreted. Moreover, no energy is transferred to the material, therefore there is no change in frequency of the scattered light comparing with that of the incident light. Hence Rayleigh scattering is an elastic scattering phenomenon having pulse spectral width in the range of MHz.

The two contributions appearing on both sides of the Rayleigh peak are the Brillouin lines. The Brillouin effect generates from photon-phonon interaction, i.e. it is contributed by the scattering of sound waves moving in opposite directions. The frequency shift associated to the Brillouin effect is in the range of GHz. Raman scattering is an interaction between light with molecular vibrations in the medium and its frequency shift is in the range of THz. Both Brillouin and Raman scattering are inelastic process since they are associated with some frequency shifts of the scattered light components. Finally, Rayleigh-wing scattering is a scattering process occurring in the wings of the Rayleigh line, resulting from fluctuations in the orientation of anisotropic molecules [10].

While the incident light is scattered without strongly altering the property of the medium, the scattering is known as spontaneous. When the light intensity increases to a certain level, the optical property of the medium can be modified. In this case, the scattered light is proportional to the power of the incident light, so this regime is called stimulated. That means that the evolution from spontaneous and stimulated scattering corresponds to a transition of the medium behavior from a linear to a nonlinear regime, as will be further explained later.

5.2.2 Brillouin scattering

As mentioned previously, BS is an optical process resulting from an interaction between an incident light wave and thermally activated acoustic waves inside the material [11]. In quantum mechanical terms the effect can be explained in the following way: the bulk motion thermally excites acoustic waves which, when propagate in the medium, provoke variations in pressure. These changes give rise to alterations in strain which, via the elasto-optic effect, generate refractive index grating, moving at sound velocity in the fiber, V_A. Hence when an incident light wave, such as a pump laser, propagates through the fiber, a frequency-shifted optical wave (Stokes or anti-Stokes) is created and propagates in the backward direction. To ensure the coupling conditions, the frequency-shift (so called Brillouin frequency shift ν_B) is linked to optical and acoustic parameters by the relationship

$$\nu_B = \frac{\omega_A}{2\pi} = \frac{2nV_A}{\lambda_s} \tag{5.1}$$

where ω_A is the acoustic wave frequency and n is the refractive index of the propagating mode at the pump wavelength λ_s. The value of the Brillouin frequency shift is typically of the order of 10-11 GHz in silica fibers at room temperature [10].

The effect described before comprises spontaneous scattering at a very low level, since the sound waves are of low energy. In general, the optical field also induces strain that reinforce the acoustic waves, but this a small effect at low laser powers. However, an increasing of the power of the pump laser may lead to a stimulated scattering regime. Fig. 5.2 schematically shows the cycle of the SBS process where two counter-propagating waves interact along the fiber. When the frequency difference between the two waves is equal the Brillouin shift of the medium ν_B, namely phase-matching conditions, the interference between the pump and signal waves generates an optical standing wave which moves through the fiber at the acoustic velocity. The standing wave so produced will consist of electric field that applied to the medium will perturb the inter-molecular forces which hold the medium, causing the material to expand or contract. This material-dependent phenomenon is called electrostriction [10] and produces an acoustic wave in sympathy with the incident light wave. This sound wave induces a

periodic modulation of the core refractive index due to pressure, co-propagating with the pump wave. This dynamic Bragg-type grating diffracts the pump wave to the signal wave with more and more efficiency as the acoustic wave grows, and thereby resulting in the signal amplification. Gradually the signal wave amplitude grows as a result of the back-scattering of the pump wave. The entire cycle is self-sustained and enhance the Brillouin scattering process: for this reason it is referred as stimulated Brillouin scattering.

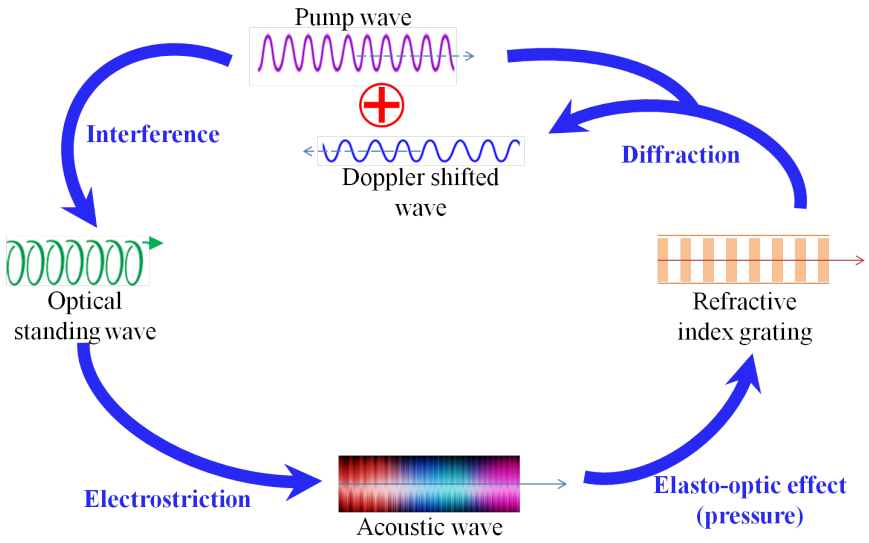

Figure 5.2: Working principle of SBS process. The realization of this self-sustained loop (counterclockwise cycle) gradually reinforces the energy transfer.

Therefore, summing up, SBS is a nonlinear parametric phenomenon in the optical fiber coupling two counter propagating waves that are detuned in frequency; a strong pump wave (up to 20 dBm) and a typical weak Stokes wave (up to 0 dBm). The SBS interaction is efficient only when the difference between the optical frequencies of the pump and probe waves is close to the Brillouin frequency ν_B.

Hence, an input signal whose frequency is ν_B lower than that of the pump wave (Stokes) will experience SBS amplification, as illustrated in Fig. 5.3. If the input probe frequency is ν_B above that of the pump wave (anti-Stokes), SBS-induced signal attenuation will be obtained instead. The net result of this waves interaction is a power transfer from the higher frequency wave to the lower frequency optical wave. The spectral characteristics of the Brillouin gain depend either on the type of optical fiber (material, type and concentration of dopant agent, refractive index profile,...) and on the relative polarization of the pump and probe signals. Finally, the spectral features of the Brillouin gain are also correlated to extrinsic parameters, like temperature and/or stain applied to the fiber. This dependence

suggests the possibility to use SBS as a sensor technique to detect environmental, physical and/or mechanical alterations along the whole length of the optical fiber [3, 4, 12, 13].

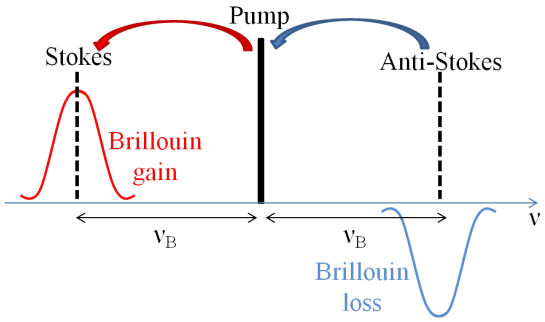

Figure 5.3: Generation of Brillouin gain and loss spectra.

5.2.3 Brillouin optical time-domain analysis

During the past decade, Brillouin-based distributed optical fiber sensing has attracted great interest from the research in optical fiber sensing community, mainly due to its ability to provide distributed strain and temperature measurements along many tens of kilometers with spatial resolution values of few meters or even tens of centimeters. One of the systems that offer the higher sensing performance is BOTDA [14]. This time-domain analysis takes advantage of SBS and is based on a pump-probe technique, as schematically depicted in Fig. 5.4. Basically, the light from a laser source is sent into a polarization controller (PC) and then modulated through an electro-optical modulator (EOM), to obtain the pump and probe signals. The light components from the EOM are amplified via an erbium-doped fiber amplifier (EDFA). By means of a wavelength-division multiplexing (WDM), the pumping pulse light is launched at one end of an optical fiber and propagates through the medium, while the weak CW light (probe signal) is launched at the opposite end of the fiber and propagates in the opposite direction. In this configuration, the pump pulse generates backward Brillouin gain; when the difference between the CW probe signal frequency and pump pulse light frequency is as same as the Brillouin frequency of the optical fiber, ν_B, then the CW light is amplified through Brillouin interaction with the pump pulse. Now, the gain experienced by the probe signal on each location can be analyzed by recording the probe amplitude in the time domain. To do so, the signal containing the Brillouin gain information is detected by a photo-detector (PD) and analyzed with the aid of a computer. Moreover, the Brillouin frequency of a fiber is changed by the strain or temperature applied on the fiber. Therefore, the Brillouin frequency shift can give the temperature and/or strain information [15].

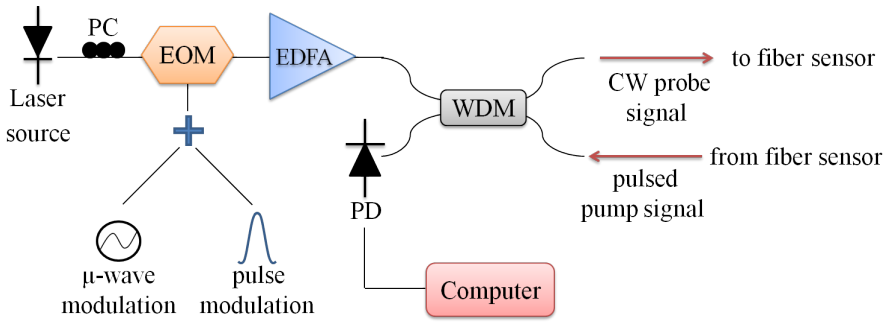

Figure 5.4: Schematic diagram of a typical BOTDA setup.

The majority of scheme employing BOTDA [13, 16] used two different lasers to generate pump and probe signals. In this configuration, the main difficulty is to generate a pump and a probe with a fixed and stable frequency difference of about 10 GHz, with stability typically better than 1 MHz for accurate measurements [15]. In [17] a simple configuration to achieve an ideal stabilization of the frequency difference, is proposed, based on a single laser source. Here, a microwave generator and an EOM are used to synthesize both pump and probe signals. The modulator is biased to operate in a suppressed carrier scheme, so that the lower modulation sideband can be used as probe signal while the upper sideband is filtered out. This way, an ideal measurement stability is reached, since any frequency drift of the laser has no impact on the frequency difference between pump and probe signals [15].

As the interference between pump and probe signals drives the electrostriction phenomenon that stimulates the acoustic wave, the states of polarization of pump and probe have to be aligned to reach the maximum gain. If pump and probe signals have orthogonal polarization states, no gain is created. Hence, as the polarization varies randomly along an optical fiber, a non-zero gain can be reached using polarization switch or polarization-diversity scheme. Finally, the spatial resolution of the BOTDA configuration is normally limited by the gain spectrum spreading due to the pump spectral broadening for short pulses [15]. Nowadays, the BOTDA technique is showing constant progress; different solutions are continuously proposed to extend the measurement range, improve the spatial resolution or enhance the sensor response.

The standard BOTDA systems use a high-power pulsed pump and a counter-propagating CW probe signal [5, 14]. Since both probe and pump powers equally contribute to the response of the entire fiber sensor [5], the ultimate limit in long-range Brillouin sensing is related to the maximum powers that can be launched into the fiber. In fact, the peak pump power of Brillouin-based sensors is limited by the threshold of any nonlinear effects, that may otherwise introduce errors in the detected Brillouin signal. More specifically, the peak pump power is essentially limited by the modulation instability (MI) [18, 19]. MI concerns the interaction between the nonlinearity and the anomalous dispersion in the fiber, which provokes instability in the signal. As a consequence of this instability, spectral sidebands are induced, situated symmetrically around the initial frequency of the pulse. The spectral sidebands grow with power and distance along the entire fiber [20]. In SBS-based distributed temperature/strain sensors these spectral sidebands result to be detrimental to the measurements. The MI induces sidebands in the pulse's spectrum that prevents accurate determination of the Brillouin intensity, limiting the peak pump power to about 100-150 mW in single mode fibers (SMFs).

As regards the CW probe power, it is limited (to ≈ 5 mW) by pump depletion, which causes distortion problems in the Brillouin gain spectrum measurement. The pump depletion may be explained as a measurement of how much the pump power depletes due to the power transfer to the probe signal [21], when the maximum Brillouin gain is reached. In distributed sensors based on spatially resolving the frequency and intensity of the back-scattered Brillouin signal along the sensing length, a pump depletion lower than 5% is needed [21], if a good spatial resolution is required. Despite this fact, the distortion effect of pump depletion can be massively alleviated using a probe signal with two spectral sidebands [21].

5.3 Proposed method based on a multi-frequency pump-probe Brillouin interaction

The main purpose of this chapter is to present an advanced configuration of distributed sensors based on SBS, using a combination of time-division and frequency-division multiplexing that is realized exploiting a smart all-fiber device containing a set of FBGs.

The technique consists in creating a multi-frequency pump pulse interacting with a matching multi-frequency CW probe signal. It is worth mentioning that there have been some prior works using multi-tone in BOTDA systems. For instance, in [22, 23] multiple tones are used to eliminate the need for pump-probe frequency scanning with the purpose to make fast dynamic measurements possible. In this method two frequency combs having different frequency separations are employed to interrogate different regions of the Brillouin gain spectrum. Otherwise, in the method proposed in this chapter, time and frequency pump-probe multiplexing are used to increase the total power launched into the fiber in order to push the limits imposed by detrimental nonlinear effects. Moreover, the interacting pump

and probe spectral components have rigorously the same frequency separation in order to enhance the response of the Brillouin interaction. In this way, a strong sensing response can be obtained as well as a significant SNR enhancement with respect to a standard BOTDA system. Also, the scheme proposed here results fully compatible with a simple direct detection, avoiding sophisticated coherent detection systems as needed in [22, 23]. This means that slight changes to the conventional BOTDA scheme are needed, since the frequency scan, acquisition process and data processing remain unaltered.

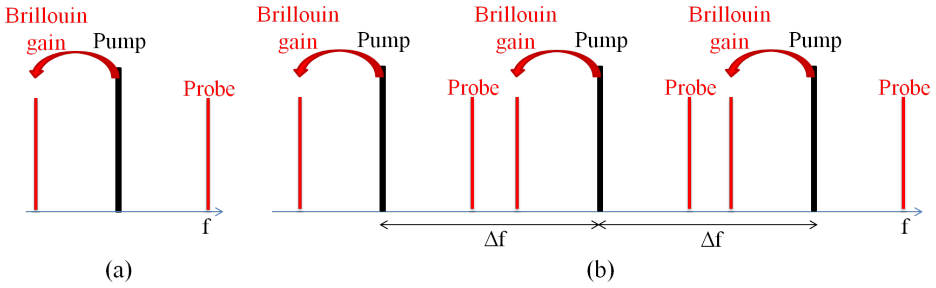

Figure 5.5: Spectral position of pump and probe signals. (a) Standard BOTDA. (b) Multi-frequency BOTDA.

Fig. 5.5(a) shows the spectral allocation of pump and probe signals in a standard BOTDA configuration, in which a single frequency pump is used. With the aim to spread the power among many frequency components to limit the peak power per pump pulse, the configuration depicted in Fig. 5.5(b) is proposed. Here, pump pulses showing N frequency components are employed to produce Brillouin amplification along the sensing fiber. This way, the total power launched into the fiber is increased, while the power in individual pulses is kept below the onset of MI. Each of these N pump frequency components interacts only with one pair of probe components symmetrically located around the pump spectral line; this interaction is similar to the one occurring in a standard BOTDA configuration. Since the sensor response linearly depends on the pump power in the small gain approximation [13], the set of the N pulses will generate a sensor response equivalent to a single pulse with an N-times larger power. Furthermore, the Brillouin interaction within each pump-probe pair must remain independent from other pair interactions. For these reason, the frequency separation Δf must be judiciously select in order to avoid unwanted Brillouin interactions with other frequency components. Actually this scheme does not work properly since the pulses show mutual interaction during their propagation giving rise to unwanted nonlinear processes. They will consequently provoke a reduction of the power and will also lead to strong distortion in the measurement, as to do so weakening significantly the system performance.

The novel concept beyond the method proposed in this chapter can be divided in two parts: the first part consists in delaying each pump pulse, to make a sequence of time-separate pulses, and then to apply a reverse delay to the probe waves to eventually obtain the equivalent reconstructed signal corresponding to the interaction of the summed pulses. The second part comprises the generation of a matching multi-frequency probe signal, as it will be described afterwards.

The first step for the proposed method consists in fractioning the pump signal in multiple replicas at different optical frequencies opportunely shifted in time (and in the subsequent time realignment at the receiver stage), as schematically depicted in Fig. 5.6. The light from an optical source composed of multiple frequency is pulse-shaped modulated, in order to obtain a high-power optical pulse. The pulsed signal is passed through a frequency selective time shifter; this way the pulse power is spread among several frequency components with the purpose to increase the total pomp power launched into the fiber, while maintaining the power of each pulse below the threshold of nonlinear effects onset [18, 19, 21].

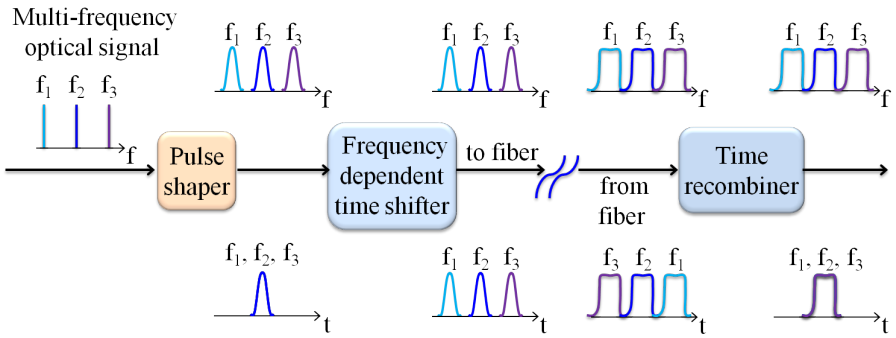

Figure 5.6: Schematic showing the working principle of the method. The pump signal is fractionated in multiple replicas at distinct optical frequencies opportunely shifted in time. At the receiver stage the BOTDA traces from the fiber sensor are temporal realigned.

According to the analysis presented in [22, 23], if the high power pulses at different frequencies are sent simultaneously into the optical fiber, during propagation undesirable nonlinear effects (such as MI or four-wave mixing) are observed. This in turn will provoke huge distortion in the traces and hence an impoverishment of the system performance. As presented in [23], a sequential pumping scheme can be employed in order to maximize the total pump power launched in the fiber, while avoiding nonlinear cross-interaction among the different frequency components. These pump pulse replicas at distinct frequencies have to be selectively delayed; the delay must be at least equal to the pulse duration in order to avoid any pulse overlapping. This way, the total signal power that can be launched into the fiber can be multiplied by an integer equal to the number

N of spectral components, even thought each pulse power remains limited by the onset of nonlinear effects.

As regarding the generation of a matching multi-frequency probe signal, two probe sidebands can be symmetrically obtained from each pump spectral line by simple amplitude modulation [17], as illustrated in Fig. 5.5(b). The frequency difference between the interacting pump-probe pairs is kept constant and identical for the N spectral pairs, thus increasing the Brillouin interaction and hence the sensor response by a factor N. As a result of this, the total amount of probe power that can be launched into the fiber can be multiplied by N, while each frequency components is still limited beyond ≈ 5 mW to avoid depletion due to amplified spontaneous BS [21].

Also, the implementation requires a time-realignment of the generated BOTDA traces at the receiver stage, as schematically depicted in Fig. 5.6. It is worth noting that the delay between the N pulses is expected to generate independent and time-shifted BOTDA traces over N different probe frequency components. Hence, the N probe signals bearing the Brillouin gain information have to be opportunely reordered in time before the photo-detection stage. This temporal rearrangement of the probe components have to be carried out by applying a reverse delay to the one originally set to the pump pulses, in order to avoid temporal jamming and hence ruining the spatial resolution of the method.

Although the use of multiple spectral components increases the sensor response and hence the SNR, the scalability of such a configuration is limited by two phenomena: four-wave mixing between the probe replicas and chromatic dispersion. Due to the closeness of the multiple frequency tones, the efficiency of four-wave mixing can increase with the number of spectral components N. Nevertheless, its effects can be reduced using unequal spacing between the spectral components, as demonstrated in [22, 23]. Since each pump-probe interaction is independent from the others, the use of unequally spaced spectral components will not negatively affect the performance of the system. Moreover, the use of a wide spectral range for the pump components will unavoidably lead to chromatic dispersion effects, which will ruin the spatial resolution. The chromatic dispersion will affect the pump pulse replicas as well as the counter-propagating sensor response. This means that, considering a round-trip propagation along the fiber, the spatial resolution increment at the end of the time-domain BOTDA signals is

$$\delta z = \frac{\lambda_c^2 \cdot D \cdot \Delta f \cdot L}{n}(N-1) \tag{5.2}$$

being λ_c the central wavelength of the frequency comb, $D(\lambda)$ the chromatic dispersion of the fiber at wavelength λ, Δf the frequency spacing between pump spectral components and L the sensing fiber length. In this way, the relationship between the maximum number of spectral components N and the increment of

the system spatial resolution δz is provided. However, if a smart choice of the spectral components allocation is made, the number of tones N can be efficiently increased, as it will be detailed in the following subsection.

5.3.1 Spectral allocation of pump and probe signals

There are different solutions for spectrally allocating pump and probe frequency tones, taking into the account that the probe sidebands generated around a given pump component must not overlap with other pump/probe tones, as schematically depicted in Fig. 5.7:

1. The first solution is illustrated in Fig. 5.7(a), where it must be ensured that $\Delta f > 2\nu_B$ to avoid spectral lines overlapping. This means that the frequency separation Δf between the N components has to be at least larger than twice the Brillouin frequency ν_B. The critical point of this frequency allocation scheme is that in the case of a large number N of frequency components, it will results in a wide spectral range, which in turn will enhance the detrimental effects of the chromatic dispersion on the system response. It is worth noting that, in this configuration and for a limited number of frequency tones ($N < 20$ and $\Delta f = 30$ GHz), the frequency uncertainty induced by gain broadening [5] would be compensated by the sensor response improvement provided by the N pump-probe interactions [24].
2. In the second configuration, depicted in Fig. 5.7(b), the pump-probe frequency pairs are interleaved. Now, the frequency separation Δf have to fulfill the condition $\nu_B < \Delta f < 2\nu_B$. This solution results more spectrally efficient than the previous one as it mitigates the undesired effects of both gain spectral broadening [5, 24] and chromatic dispersion. However, it should be considered that a narrower optical filtering is required at the receiver to properly select the BOTDA information.
3. In the third and last case, schematically described at Fig. 5.7(c), the frequency separation Δf is larger than the twice the natural Brillouin linewidth $2\Delta\nu_B = 60$ MHz, but lower than the Brillouin frequency ν_B, i.e. $2\Delta\nu_B < \Delta f < 2\nu_B$. If the latter is satisfied, it is secured that no crosstalk is generated from coincidental pump-probe gain interactions [23]. Due to the small frequency separation Δf required by this last solution, the multi-frequency pump comb would be easier to generate if compared with the previous configurations. Nevertheless, the scheme may be practically hard to implement if optical filter are employed to discriminate and to delay the different N probe replicas. In this configuration, the effect of chromatic dispersion would be negligible, while the number N of frequency components is limited by the frequency separation Δf and the Brillouin frequency ν_B, according to the relationship $N < \nu_B/\Delta f$.

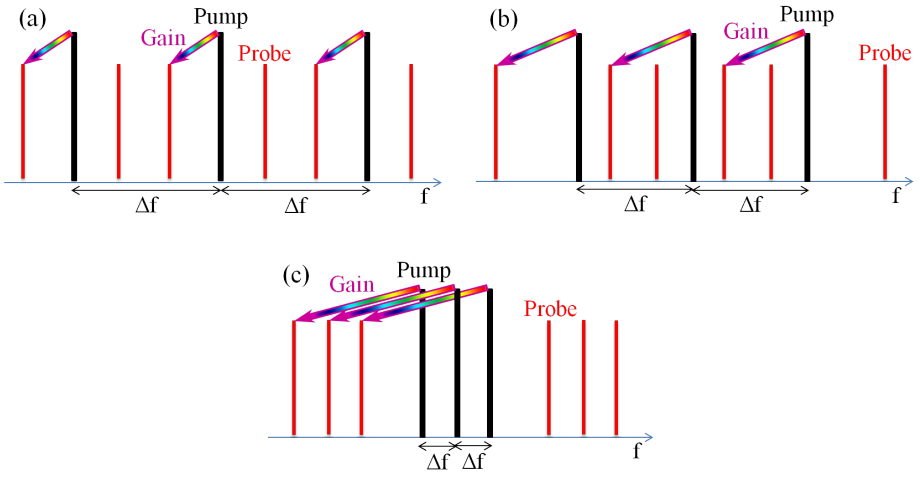

Figure 5.7: Different implementations for spectral allocating the pump and probe signals. The black lines are the pump frequency components, while the red lines represent the counter-propagating probe tones.(a) $\Delta f > 2\nu_B$. (b) $\nu_B < \Delta f < 2\nu_B$. (c) $2\Delta\nu_B < \Delta f < 2\nu_B$. $\nu_B \approx$ 10-11 GHz is the Brillouin shift in silica fiber at room temperature and $\Delta\nu_B \approx$ 30 MHz is the Brillouin linewidth.

5.4 FBG array characteristics and tuning method

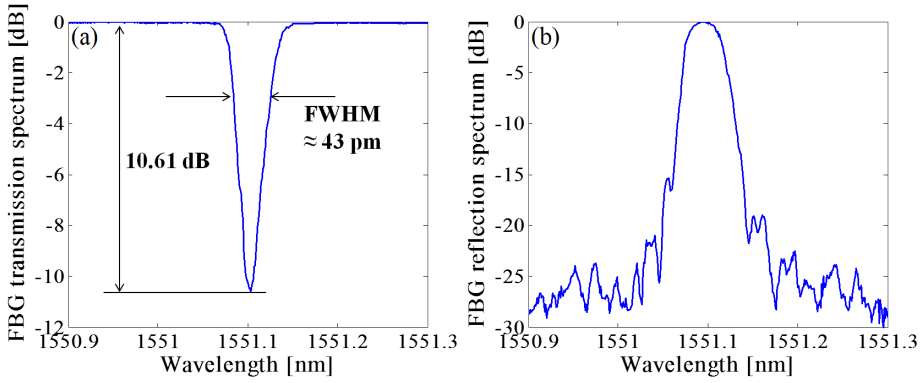

Figure 5.8: Spectral features of each gratings of the array cascaded FBGs used in the experiment(a) FBG transmission spectrum. (b) FBG reflection spectrum.

A crucial aspect of the method is to develop the devices that will generate the proper wavelength-dependent delays and the subsequently time-realignment of the N BOTDA traces. For this purpose two custom-made arrays of three FBGs have been fabricated. The fabrication of two arrays containing each one three equal and equally-spaced FBGs has required a great deal of precision and

effort. A rigorous work has be needed to fabricate, with our laboratory facilities, gratings presenting equal or very close values of Bragg resonance, reflectivity and FWHM. In particular, the grating reflectivity has been suitably controlled by accurately setting the ultraviolet exposure time during the fabrication process. Eventually, the prepared gratings show high reflectivity (above 90%), are 7 cm long and the spatial separation between consecutive elements is 5 meter. The FBGs have a Bragg resonance of $\approx$ 1551.1 nm at room temperature and show a narrow-band transmission of $\approx$ 43 pm FWHM (full width at half maximum). The mean features of one of the FBGs used in the experiment are illustrated in Fig. 5.8(a) (transmission spectrum) and in Fig. 5.8(b) (reflection spectrum).

Each FBG has been mounted on a distinct translation stage for a selective fine tuning by elongating the grating, as shown in Fig. 5.9. The translation platforms are provided with a micrometric adjuster which allows a selective tuning with a precision of less than 0.05 nm, being the strain coefficient of the optical fiber of 1.15 pm/$\mu\varepsilon$.

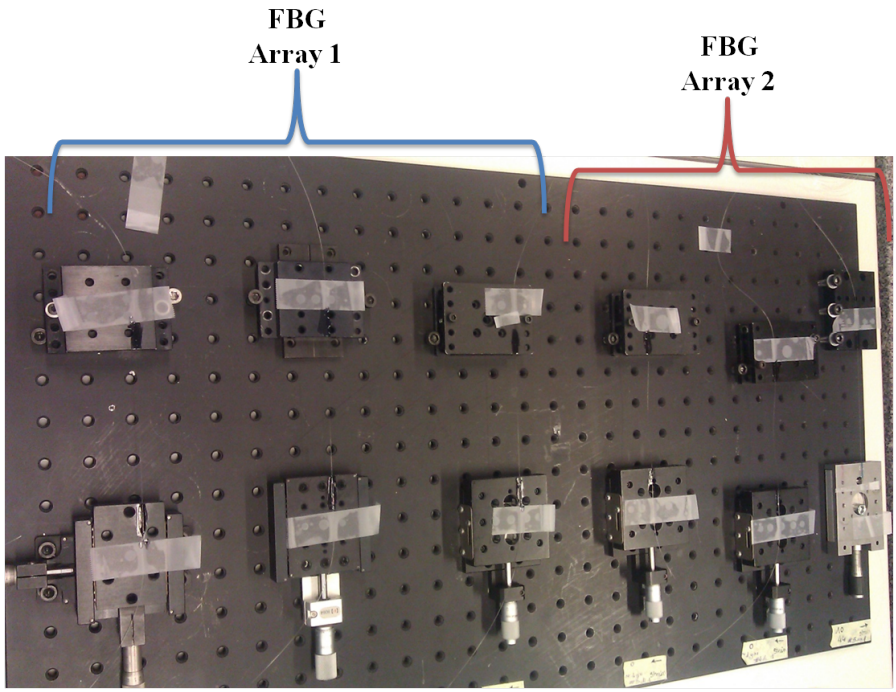

Figure 5.9: FBGs mounted on translation platforms in order to mechanical shift the resonance wavelength.

The correct operation of the method is based on the possibility to precisely control the resonance wavelength of each FBG. In order to prove this an initial test is performed according to the scheme in Fig. 5.10. A laser source is electro-optically modulated with a 17 GHz tone via a Mach-Zehnder modulator (MZM) and then modulated again by means of a 20 ns pulse using another MZM. PCs are placed before each MZMs with the purpose of enhancing the modulation efficiency. An EDFA is inserted after the first MZM to increase the power reaching the second modulation stage. The multi-wavelength pulse-comb from the second MZM is injected into the first array using an optical circulator and the reflected signal is analyzed by means of an oscilloscope. The signal at the input port (port 1) of the circulator consists of three synchronous optical pulses at three different wavelengths. Each resonance of the three FBGs connected at the port 2 of the circulator has been properly tuned in order to match one of the three wavelengths of the pulsed signal (see Fig. 5.10(a)). For this reason, after passing through the first array, the multi-wavelength signal recorded by the oscilloscope is formed of a sequence of three distinct pulses temporally delayed, each having duration of 20 ns. The delay between two consecutive pulses is exactly determined by the back-and-forth propagation time in the fiber segment between two consecutive FBGs.

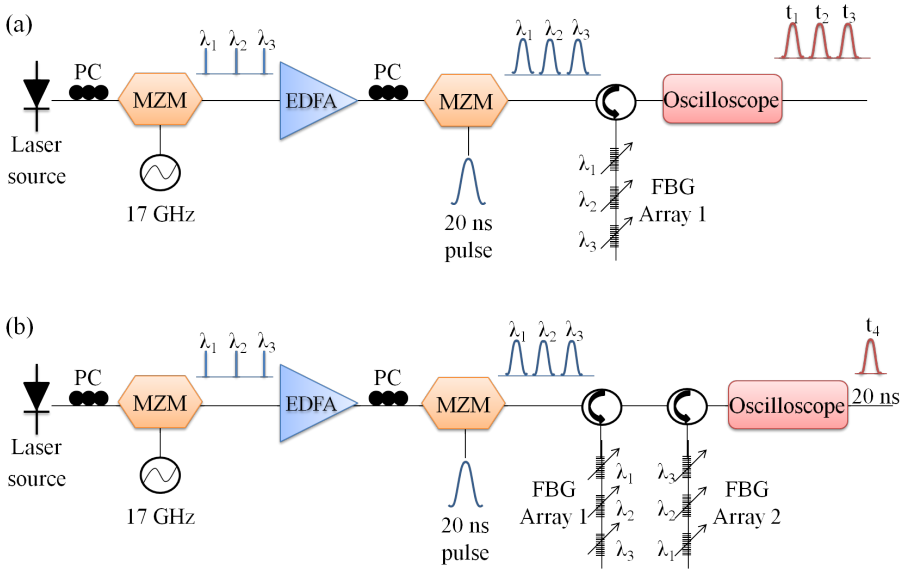

Figure 5.10: Experimental schemes used to perform the initial test on the FBG arrays. (a) Time delaying and (b) Temporal realignment of the N spectral components.

In the second part of this initial test, both arrays are cascaded and the signal reflected by the second array is temporally analyzed. As the resonances of the FBGs of the second array have been properly controlled to exactly compensate the previously induced delays (see Fig. 5.10(b)) the multi-wavelength signal displayed on the oscilloscope shows a single 20 ns pulse. It is worth to mention that, as the reconstructed signal has the same duration of the modulating pulse (20 ns), the spatial resolution of the method will not be negatively affected by the temporal shift/realignment of the N BOTDA traces.
This preliminary test proves that, by using a combination of time-division and frequency-division multiplexing, the correct operation of the FBGs is checked. The three pulses at three different wavelengths could propagate separately, i.e. temporally distinct, along the optical fiber to minimize spurious nonlinear effects and then will be recombined to form a single pulse before detection.

5.5 Description of the sensing method and experimental setup

The experimental setup used to verify the feasibility of the multi-frequency BOTDA method using $N = 3$ frequency components is depicted in Fig. 5.11. The intensity of a CW laser source is modulated using a MZM with a 17 GHz tone. The direct current (DC) bias voltage of the modulator has been adjusted so that three carrier and sidebands are obtained with the same amplitude. This multi-frequency signal is then split into two arms to generate pump and probe signals following procedures employed in standard BOTDA schemes. The probe light is created by means of another MZM driven by a microwave signal at the Brillouin frequency of the fiber ν_B, operating in carrier-suppression mode [17], which creates sidebands in the modulated laser spectrum, while the optical power at the original $N = 3$ frequencies (carriers) is nearly totally suppressed. In this way, two sidebands around each of the three original frequencies are created, thus a set of six spectral lines is obtained as probe signal. Since the separation between the three original spectral lines is $\Delta f = 17$ GHz, the probe sidebands generated from each pump component are interleaved as in the configuration depicted in Fig. 5.7(b). A polarization switch is used to avoid any gain fading effect resulting from the polarization-dependent Brillouin interaction. In the other arm the pump pulses are created by a semiconductor optical amplifier (SOA), in which the gain is gated using a train of electric pulse having duration of 20 ns, corresponding to a 2 m spatial resolution. Adjusting the output power of EDFAs and variable optical attenuators (VOAs), probe and pump powers are separately optimized at the fiber input to prevent nonlinear effects and optimize the system response.

Then the pump light is passed through the first FBG array in which the three FBGs are each properly tuned at one of the different frequency of the pump signal. This way, by simply adjusting the FBGs elongation, three pulses spectrally separated by 17 GHz are obtained with a time spacing of 50 ns. The signal reflected from the first array and the probe light are directed to each end of a 50 km sensing fiber.

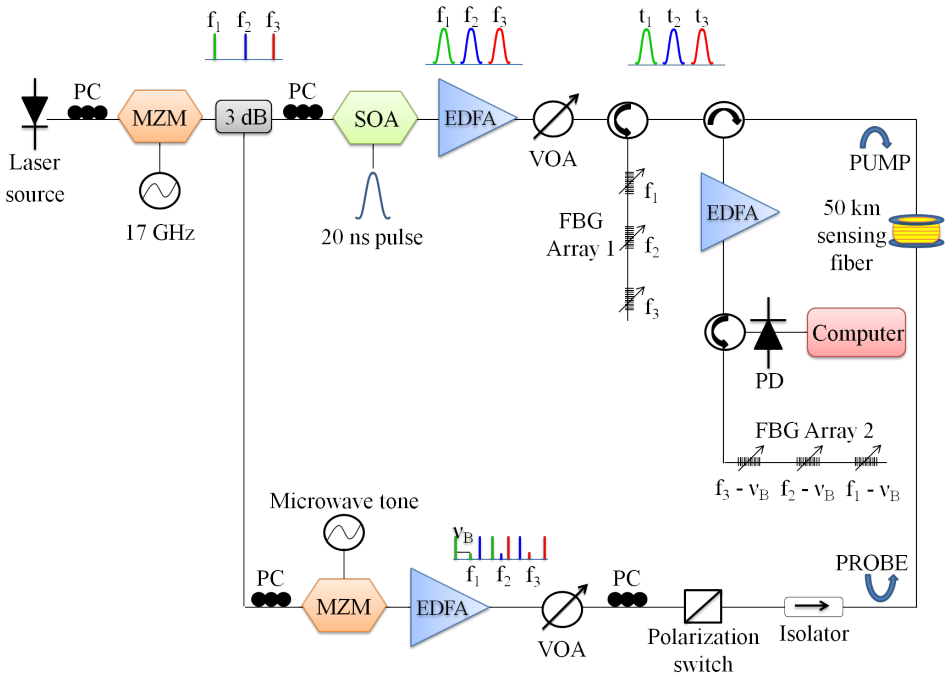

Figure 5.11: Experimental scheme for multi-frequency BOTDA sensing.

Finally, light from the probe channel is amplified by an EDFA and then extracted at the fiber output using the second array of FBGs which is employed to transmit only one of each pair of sideband onto a 125 MHz PD. These FBGs are suitably tuned in order to apply a selective reverse delay to the probe waves, as previously described in Fig. 5.6, so that the time differences resulting from the delayed pump pulses are compensated. Hence, the BOTDA traces are automatically properly rearranged to obtain the equivalent trace corresponding to the interaction of the summed pulses. Furthermore, the FBG array in the receiver also helps to filter out unwanted frequency components (i.e. the upper sidebands experiencing Brillouin loss) as well as the amplified spontaneous emission (ASE) noise originated by the EDFAs. After photo-detection, the signal is eventually acquired and digitalized with a card connected to a computer.

5.6 Experimental measurements and results

In this section the main results obtained with the BOTDA scheme described above are shown. The importance of the multi-frequency BOTDA method is underlined thanks to the comparison between the standard BOTDA configuration in which just one frequency component is used. Also, the measurement of a hot spot along the sensing fiber is reported in order to verified the spatial resolution of the method. Finally the measurement of the pump depletion is provided, resulting in negligible distortion in the BOTDA traces.

5.6.1 Sensor response

Once the initial assessment of the scheme have been completed, BOTDA traces at the peak gain frequency have been acquired for both $N = 3$ and $N = 1$ (standard BOTDA), in order to experimentally validate the multi-frequency configuration. The peak power of the pump pulses has been adjusted to the maximum of 100 mW per pulse to avoid MI [18, 19]; so that the total pump power for $N = 3$ results of 300 mW. As previously mentioned, in order to avoid the onset of nonlinearities, the three pulses are properly ordered in both time and frequency domains. This way, when the modulation frequency of the MZM in the probe channel is close to the Brillouin frequency shift of the fiber under test, the first lower sideband lies in the Brillouin gain spectrum generated by the pump and is amplified through the Brillouin interaction.

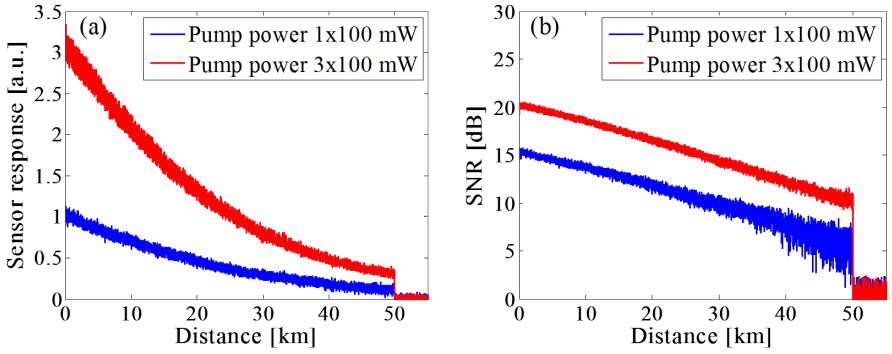

Figure 5.12: Comparison between the standard BOTDA using $N = 1$ (blue curves) and the multi-frequency configuration using $N = 3$ and delayed pump pulses (red curves). (a) Sensor response measured at the peak gain frequency. (b) SNR measured at the peak gain frequency.

Fig. 5.12(a) shows the comparison between BOTDA traces for both cases ($N = 1$ and $N = 3$). This result indicates that the use of three frequency components increases the sensor response [5] by a factor 3, as a result of the higher total pump power. This factor corresponds to a SNR enhancement of 4.8 dB, as illustrated in Fig. 5.12(b) which compares the SNR of the BOTDA traces for standard ($N = 1$) and multi-frequency ($N = 3$) cases. Using the standard BOTDA configuration with a 2 m spatial resolution and 2000 time-averaged traces, a SNR equal to 6.1 dB is observed at the fiber far end. On the other hand, under the same condition, using the multi-frequency configuration ($N = 3$), the SNR has been improved up to 10.9 dB. A PD with high-trans-impedance amplifier has been employed to optimize the SNR, making the configuration dominated by thermal noise. This assumption has been checked by measuring the noise power after photo-detection and by calculating the standard deviation of the BOTDA temporal traces after the end of the fiber, where no Brillouin gain is presented. The total noise in the BOTDA system has resulted to be the same for both configurations and turns out to be equal to the PD thermal noise. This fact explains the SNR enhancement of a factor $N = 3$ (equal to 4.8 dB) and infers that much higher SNR enhancement may be reached if the number of frequency components is increased.

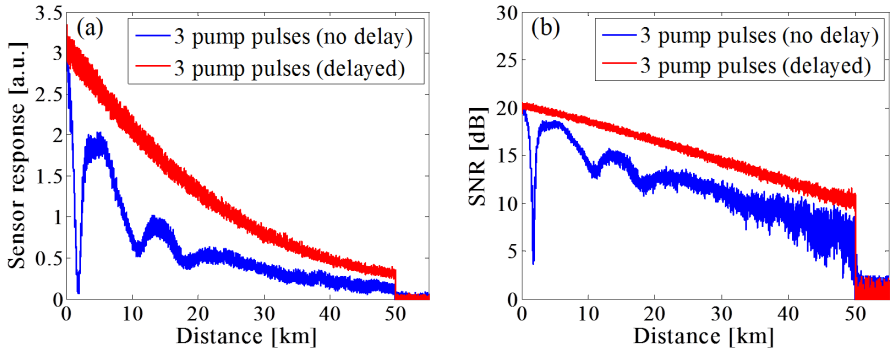

Figure 5.13: Comparison between traces measured with $N = 3$ frequency lines, with (red curves) and without (blue curves) delay between pump pulses. (a) Sensor response and (b) SNR evolution along the sensing fiber measured at the peak gain frequency.

At this point, it is important to worth out that no distortion (potentially generating from nonlinear effects) is observed in the BOTDA traces obtained for $N = 3$ (red curves in Fig. 5.13), though high pump power (300 mW) is launched into the fiber. This result infers that the delay between pump pulses at different frequencies plays a crucial role in the multi-frequency BOTDA configuration. To check this assumption three 100 mW pulses at distinct frequencies are synchronously sent into the fiber; the parametric interaction among the spectral components leads to a distorted BOTDA trace (blue curves in Fig. 5.13). The comparison between BOTDA traces at the peak gain obtained with (red curves) and without (blue curves) delays between pulses is illustrated in Fig. 5.13(a) in

terms of sensor response and Fig. 5.13(b) in terms of SNR. It is worth noticing that the same sensor response and SNR are observed in both cases at the fiber input, as the input pump power is the same in both configurations. However, without time delay between pulses, nonlinearities resulting from parametric interaction among the synchronous pulses produce strong oscillations in the effective pump power [19, 22], and hence in the measured Brillouin gain (blue curves at Fig. 5.13). These oscillations can be eliminated using the wavelength-dependent delays, leading to a Brillouin traces with no distortion (red curves in Fig. 5.13).

5.6.2 Brillouin gain spectrum and frequency uncertainty

The Brillouin gain spectrum represents the Brillouin gain for the probe signal as a function of the frequency offset ν from the pump frequency, and it is described by [17, 25]

$$g_B(\nu) = g_{B_0} \frac{(\Delta\nu_B/2)^2}{(\nu - \nu_B)^2 + (\Delta\nu_B/2)^2} \tag{5.3}$$

where g_{B_0} is the Brillouin gain coefficient and $\Delta\nu_B$ is the Brillouin gain linewidth (i.e. the FWHM). Equivalent expressions of the Brillouin gain coefficient in term of the constitutive parameters have been shown in literature [10, 17, 25]. In bulk silica, the typical value of g_{B_0} in 1550 nm band is approximately 5 x 10^{-11} m/W [25].

In our experiment, the Brillouin gain spectrum has been measured using a frequency sampling step (i.e. the frequency increment between consecutive Brillouin traces), $\delta = 1$ MHz. The measured Brillouin gain spectrum versus distance using $N = 3$ spectral components is depicted in Fig. 5.14. At this point, fitting the measured spectrum with a parabolic curve [5], the Brillouin frequency profile has been evaluated, as shown in the inset of Fig. 5.14. The latter result illustrates that the Brillouin frequency is around 10.7 GHz along the entire length of the fiber. The error in the estimate of the Brillouin frequency shift as a function of the SNR can be expressed as [5]

$$\sigma_\nu(z) = \frac{1}{SNR(z)} \sqrt{\frac{3\delta\Delta\nu_B}{8\sqrt{2}(1-\eta)^{3/2}}} \tag{5.4}$$

where z represents the sensing fiber longitudinal axis and η is the fraction of the peak level over which a quadratic least-square fitting is calculated [5].

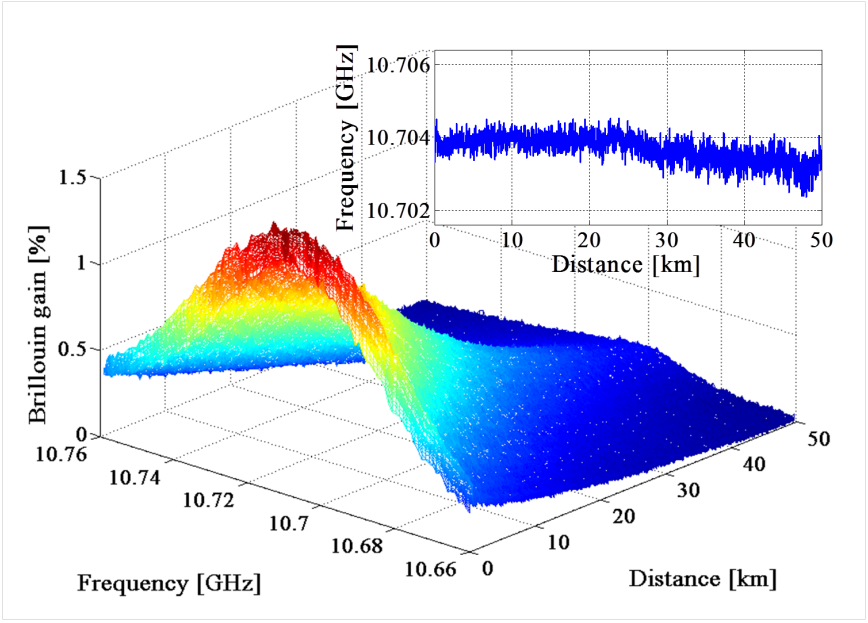

Figure 5.14: Measured Brillouin gain spectrum versus distance using $N = 3$ spectral components and 1 MHz frequency scanning step. Inset: Brillouin frequency profile at ambient temperature (24°C) obtained fitting the spectrum with a parabolic curve.

Furthermore, the uncertainty of the sensor has been estimated for the standard BOTDA scheme ($N = 1$) and for the multi-frequency configuration ($N = 3$), by calculating the standard deviation of the measured Brillouin frequency along the entire fiber. The frequency uncertainty versus distance for the standard BOTDA configuration (blue curve) and for the case using $N = 3$ spectral components (red curve) are illustrated in Fig. 5.15. This assessment indicates that an accuracy of 1.8 MHz is obtained with the standard scheme at the end of the sensing fiber (50 km) while an improved accuracy down to 0.6 MHz is reached when the scheme with $N = 3$ spectral components is used. This corresponds to a factor 3 in the uncertainty reduction, which perfectly agrees with the prediction of a 4.8 dB SNR enhancement [5].

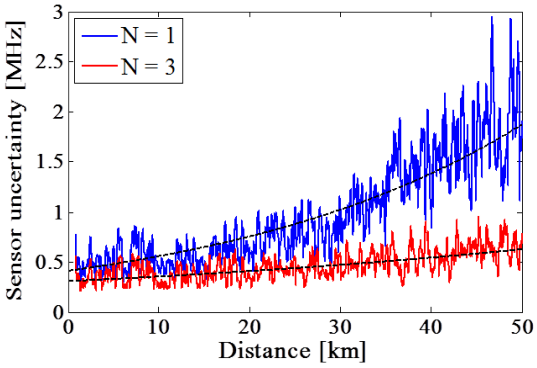

Figure 5.15: Frequency uncertainty versus distance, for standard BOTDA configuration ($N = 1$) and for multi-frequency BOTDA scheme ($N = 3$).

5.6.3 Spatial resolution

The spatial resolution of the Brillouin-based optical analysis is generally limited to 1 m [15]. The reason of this practical limitation are briefly explained hereinafter; if the pump pulse spans over a bandwidth larger than the Brillouin gain spectrum, the back-scattered signal will show a broader spectral distribution due to the convolution of the Brillouin gain spectrum with the pulse spectrum, jamming the spatial information. Hence, as the natural Brillouin distribution is given by the acoustic lifetime of about 10 ns (corresponding to a spatial resolution of 1 m) [15], the pump pulse should not be shorter than this time. In the multi-frequency BOTDA configuration described in the previous section, the pump pulses have a duration of 20 ns which corresponds to a spatial resolution of 2 m.

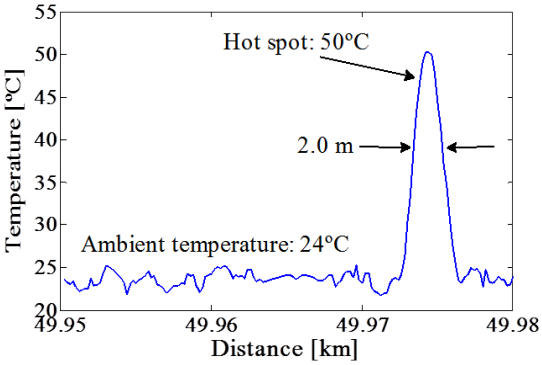

Figure 5.16: Hot spot measurement at the far fiber end, demonstrating 2 m spatial resolution when using 20 ns pump pulses.

The spatial resolution of the method has been experimentally validated by provoking a hot spot in the sensing fiber near the farthest end. For this purpose 2 m of the sensing fiber have been heated up to 50°C, while the rest of the fiber is kept at room temperature (24°C). This way a crucial assessment for this method considering the pulses de-synchronization followed by the re-synchronization of the traces has been verified. In fact, any imprecision in the reverse delays delivered by the second FBG array will eventually adversely influence the spatial resolution of the method. Fig. 5.16 illustrates the hot spot detection measured near a 50 km distance using the multi-frequency BOTDA scheme ($N = 3$). This test indicates a correct determination of the temperature within the hot region and the 2.0 m spatial resolution has not been negatively affected. It is worth pointing out that this measurement has been performed at the end of the sensing fiber length where the SNR is the worst, so that the claimed spatial resolution is effective for the entire sensing length.

5.6.4 Pump depletion

Finally, the pump depletion of the method has been experimentally verified. Actually this is a critical test for this multi-frequency BOTDA scheme, since pump depletion may cause distortion problem in the Brillouin gain spectrum measurement. As previously mentioned, pump depletion may be explained as a measurement of how much the pump power depletes due to the power transfer to the probe signal, when the maximum Brillouin gain is reached. For the pump depletion measurement purpose, the pulse signal is sent into the sensing fiber and the MZM in the probe arm is driven by a microwave signal at a frequency different from the Brillouin frequency. In this condition, as there is no Brillouin interaction between pump and probe channels, the signal reflected from the sensing fiber will experienced a 10 dB attenuation due to the length of the SMF (50 km). Now, when the modulation frequency of the MZM in the probe channel is set at the Brillouin frequency of the sensing fiber, the first lower sideband lies in the Brillouin gain spectrum generated by the pump and was amplified through the Brillouin interaction. This will provoke pump-to-probe power transfer with consequent pump depletion, as schematically shown in Fig. 5.17. The difference between the power of the pulse signal reflected from the sensing fiber whit and without Brillouin interaction is the measurement of the pump depletion.

This way, pump depletion has been measured to be below 4%. As in this type of distributed sensor based on spatially resolving the frequency and intensity of the back-scattered Brillouin signal along the sensing length, a pump depletion lower than 5% is desirable [21], the measured value of pump depletion results in negligible additional distortion in the traces.

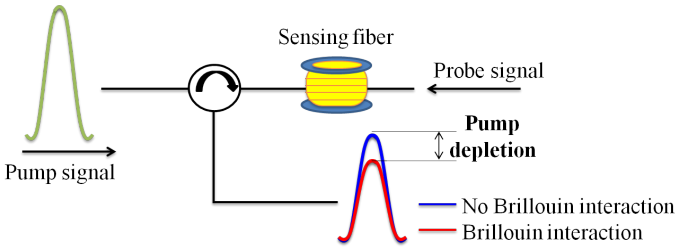

Figure 5.17: Schematic for the description of pump depletion measurement.

5.7 Conclusions

In this chapter, an advanced configuration of distributed sensors based on SBS, using a combination of time-division and frequency-division multiplexing that is realized using two FBG arrays has been experimentally validated. Brillouin-based distributed optical fiber sensing has been demonstrated to offer novel and outstanding capabilities, attracting great interest from the research in optical fiber sensing community. In particular, the reason of this matter relies on SBS-based sensing ability to provide distributed strain and temperature measurements along many tens of kilometers with relative fine spatial resolution.

One of the systems that offer the higher sensing performance is BOTDA, that is a time domain analysis based on a pump-probe technique taking advantage of SBS. A pumping pulse is launched at one end of an optical fiber while a weak CW probe is launched at the opposite side. When the difference between the CW signal and the pump pulse frequency is as same as the Brillouin frequency of the optical fiber, then the CW light is amplified through Brillouin interaction with the pump pulse. As the Brillouin frequency changes by the strain or temperature applied on the fiber, its shift can give the temperature and/or strain information. In this configuration, the ultimate limit in Brillouin-based fiber sensing is related to the maximum powers that can be launched into the fiber. In particular, the peak pump power is limited by the threshold of nonlinearities, MI chiefly, while the CW probe power is mainly limited by pump depletion, which distorts the traces.

In the work carried out and explained in this chapter, a technique to enhance the response and performance of BOTDA sensors has been proposed and demonstrated. This technique is based on a method developed to by-pass the fundamental limits given by fiber nonlinearities and pump depletion which limit the maximum power into the sensing fiber. The BOTDA scheme proposed uses a combination of time-division and frequency-division multiplexing that is realized exploiting a smart all-fiber device containing a set of 7 cm-long FBGs. Here, pump pulses showing $N = 3$ frequency components are employed to produce Brillouin amplification along the sensing fiber. This way, the total power launched into the fiber is increased, while the power in individual pulses is kept below the threshold of MI. Hence the sensor response can be arbitrarily multiplied by integer steps N

and is eventually limited by the added complexity of the passive time-frequency mux-demux device.

Firstly, BOTDA traces at the peak gain frequency have been acquired for both configurations ($N = 1$ and $N = 3$), while the peak power of the pump pulses has been adjusted to the maximum of 100 mW per pulse. Results indicates that the use of three frequency components increases the sensor response by a factor 3, corresponding to a SNR enhancement of 4.8 dB. The additional SNR achieved by using this configuration can be useful to extend the sensing range, to reduce measurement time, and/or to improve spatial and measured resolutions. Furthermore, no distortion have been observed in the BOTDA trace obtained for $N = 3$, while when three 100 mW pulses at distinct frequencies have been synchronously sent into the fiber, distorted traces have been showed. This result infers that the delay between pump pulses at different frequencies plays a crucial role in the multi-frequency BOTDA configuration.

The uncertainty of the sensor has been estimated for both cases, by calculating the standard deviation of the measured Brillouin frequency along the entire fiber. An accuracy of 1.8 MHz has been obtained with the standard scheme at the end of the sensing fiber while an improved accuracy down to 0.6 MHz has been reached when the scheme with $N = 3$ spectral components has been used. This corresponds to a factor 3 in the uncertainty reduction, which perfectly agrees with the prediction of a 4.8 dB SNR enhancement [5].

The spatial resolution of the method has been experimentally validated by provoking a 2 m-long hot-spot in the sensing fiber near the farthest end. This was a crucial assessment for this method, since any imprecision in the reverse delays delivered by the second FBG array will eventually adversely influenced the spatial resolution. Actually, this test have been indicated a correct determination of the temperature within the hot region and the 2.0 m spatial resolution has not be negatively affected.

Finally, the pump depletion of the method has been experimentally verified, resulting to be below 4%. As in this type of distributed sensors, a pump depletion lower than 5% is desirable [21], the measured value of pump depletion has resulted in negligible additional distortion in the traces.

In the end, this multi-frequency BOTDA scheme offers many advantages if compared to alternative approaches: simple direct detection has been employed, without using sophisticated detection schemes based for instance on coherent detection. Moreover, the frequency scan, the acquisition proceedings and the processing of the data retrieved remain unmodified from the standard BOTDA scheme. It is important to noting that the sensor response and SNR improvement provided by the proposed technique could be further enhanced by using a large number of spectral components. This results very attractive for long measurement range in which low power levels usually reach the PD front-end.

Bibliography

[1] L. Thévenaz, A. Denisov, and M. A. Soto, "Brillouin distributed fiber sensing at ultra-high spatial resolution," in *IEEE Photonics Conference (IPC) 2015*, pp. 337–338, IEEE, Oct 2015.

[2] Y. London, Y. Antman, N. Levanon, and A. Zadok, "Brillouin analysis with 8.8 km range and 2 cm resolution," in *Proc. SPIE*, vol. 9634, pp. 96340G–96340G–4, Sep 2015.

[3] T. Horiguchi, T. Kurashima, and M. Tateda, "Tensile strain dependence of Brillouin frequency shift in silica optical fibers," *Photonics Technology Letters, IEEE*, vol. 1, pp. 107–108, May 1989.

[4] D. Culverhouse, F. Farahi, C. Pannell, and D. Jackson, "Potential of stimulated Brillouin scattering as sensing mechanism for distributed temperature sensors," *Electronics Letters*, vol. 25, pp. 913–915, May 1989.

[5] M. A. Soto and L. Thévenaz, "Modeling and evaluating the performance of Brillouin distributed optical fiber sensors," *Opt. Express*, vol. 21, pp. 31347–31366, Dec 2013.

[6] M. A. Soto, G. Bolognini, F. D. Pasquale, and L. Thévenaz, "Simplex-coded BOTDA fiber sensor with 1 m spatial resolution over a 50 km range," *Opt. Lett.*, vol. 35, pp. 259–261, Jan 2010.

[7] A. Zadok, Y. Antman, N. Primerov, A. Denisov, J. Sancho, and L. Thévenaz, "Random-access distributed fiber sensing," *Laser & Photonics Reviews*, vol. 6, pp. L1–L5, Jun 2012.

[8] F. Rodriguez-Barrios, S. Martin-Lopez, A. Carrasco-Sanz, P. Corredera, J. Ania-Castanon, L. Thévenaz, and M. Gonzalez-Herraez, "Distributed Brillouin fiber sensor assisted by first-order Raman amplification," *J. Lightwave Technol.*, vol. 28, pp. 2162–2172, Aug 2010.

[9] M. A. Soto, M. Taki, G. Bolognini, and F. Di Pasquale, "Simplex-coded BOTDA sensor over 120-km SMF with 1-m spatial resolution assisted by optimized bidirectional Raman amplification," *Photonics Technology Letters, IEEE*, vol. 24, pp. 1823–1826, Oct 2012.

[10] R. W. Boyd, *Nonlinear Optics, Third Edition.* Academic Press, 3rd ed., 2008.

[11] K. Grattan and B. Meggitt, *Optical fiber sensor technology: advanced applications - Bragg gratings and distributed sensors.* Optical fiber sensor technology / ed. by K. T. V. Grattan, Springer, 2000.

[12] T. Kurashima, T. Horiguchi, and M. Tateda, "Distributed-temperature sensing using stimulated Brillouin scattering in optical silica fibers," *Opt. Lett.*, vol. 15, pp. 1038–1040, Sep 1990.

[13] X. Bao, J. Dhliwayo, N. Heron, D. Webb, and D. Jackson, "Experimental and theoretical studies on a distributed temperature sensor based on Brillouin scattering," *J. Lightwave Technol.*, vol. 13, pp. 1340–1348, Jul 1995.

[14] T. Horiguchi, K. Shimizu, T. Kurashima, M. Tateda, and Y. Koyamada, "Development of a distributed sensing technique using Brillouin scattering," *J. Lightwave Technol.*, vol. 13, pp. 1296–1302, Jul 1995.

[15] L. Thévenaz, "Brillouin distributed time-domain sensing in optical fibers: state of the art and perspectives," *Frontiers of Optoelectronics in China*, vol. 3, pp. 13–21, Jan 2010.

[16] L. Thévenaz, S. L. Floch, D. Alasia, and J. Troger, "Novel schemes for optical signal generation using laser injection locking with application to Brillouin sensing," *Measurement Science and Technology*, vol. 15, p. 1519, Jul 2004.

[17] M. Nikles, L. Thévenaz, and P. Robert, "Brillouin gain spectrum characterization in single-mode optical fibers," *J. Lightwave Technol.*, vol. 15, pp. 1842–1851, Oct 1997.

[18] S. M. Foaleng and L. Thévenaz, "Impact of Raman scattering and modulation instability on the performances of Brillouin sensors," in *Proc. SPIE*, vol. 7753, pp. 77539V–77539V–4, May 2011.

[19] M. Alem, M. A. Soto, and L. Thévenaz, "Modelling the depletion length induced by modulation instability in distributed optical fibre sensors," in *Proc. SPIE*, vol. 9157, pp. 91575S–91575S–4, Jun 2014.

[20] M. N. Alahbabi, Y. T. Cho, T. P. Newson, P. C. Wait, and A. H. Hartog, "Influence of modulation instability on distributed optical fiber sensors based on spontaneous Brillouin scattering," *J. Opt. Soc. Am. B*, vol. 21, pp. 1156–1160, Jun 2004.

[21] L. Thévenaz, S. F. Mafang, and J. Lin, "Effect of pulse depletion in a Brillouin optical time-domain analysis system," *Opt. Express*, vol. 21, pp. 14017–14035, Jun 2013.

[22] A. Voskoboinik, J. Wang, B. Shamee, S. R. Nuccio, L. Zhang, M. Chitgarha, A. Willner, and M. Tur, "SBS-based fiber optical sensing using frequency-domain simultaneous tone interrogation," *J. Lightwave Technol.*, vol. 29, pp. 1729–1735, Jun 2011.

[23] A. Voskoboinik, O. F. Yilmaz, A. W. Willner, and M. Tur, "Sweep-free distributed Brillouin time-domain analyzer (SF-BOTDA)," *Opt. Express*, vol. 19, pp. B842–B847, Dec 2011.

[24] G. Bolognini, M. A. Soto, and F. Di Pasquale, "Fiber-optic distributed sensor based on hybrid Raman and Brillouin scattering employing multiwavelength Fabri-Pérot lasers," *Photonics Technology Letters, IEEE*, vol. 21, pp. 1523–1525, Oct 2009.

[25] K. Hotate and T. Hasegawa, "Measurement of Brillouin gain spectrum distribution along an optical fiber using a correlation-based technique–proposal, experiment and simulation–," *IEICE Transactions on Electronics*, vol. E83, pp. 405–412, Mar 2000.

Chapter 6

Conclusions and future perspectives

6.1 Summary and overall conclusions

This Ph.D. thesis has been focused on the study, design and performance evaluation of customized grating-based devices, with the aim to improve the interrogation process of optical fiber sensors. Different kinds of grating structures have been employed, such as fiber Bragg gratings (FBGs), large-scale cascaded-FBGs and long period gratings (LPGs). Furthermore, novel systems and technologies allowing the detection of different parameters (such as liquid level, temperature, spot events and humidity) have been investigated and experimentally validated. The advantages of fiber grating devices (fast response, high sensitivity, distributed and multiplexing capability) have been exploited, performing sensing systems based on time-frequency domain analysis and on microwave photonics (MWP) techniques. Also, the feasibility of FBGs as selective wavelength filters has been demonstrated, presenting an alternative approach to improve the response and performance of Brillouin distributed fiber sensors.

Chapter 2 has been focused on a technique based on time-frequency domain analysis, which has been employed to interrogate different kinds of FBGs-based sensors. Preliminary proposals were demonstrated to characterize the Bragg frequency distribution in order to realize distributed sensors. For instance, optical low-coherence reflectometry (OLCR) [1] demonstrates high spatial resolution, but a limited measurement range and a slow response time. Also, synthesis of optical coherence function (SOCF) [2] allows a point-by-point characterization of the grating properties by simply tuning the modulation frequency of the optical source, although it requires a very complicated setup and expensive devices. A third alternative is based on optical frequency domain reflectometry (OFDR) [3], which allows long measurement range with very good performance in terms of spatial resolution and precision. However, this performance has been obtained by combining OFDR with an advance cross-correlation based method, comprising a

sophisticated post processing scheme and an auxiliary interferometer used to avoid any non-linearity. Moreover, the system results polarization-dependent and thus requires the presence of a polarization beam splitter and two separate detectors to mitigate signal fading. Furthermore, fiber distributed sensing based on very-weak reflectivity FBG has also been demonstrated using optical time-domain reflectometry (OTDR) [4, 5]. By scanning the laser frequency a distribution map of the reflectivity along the fiber has been obtained, demonstrating very good performance in terms of accuracy and signal response. The measurements presented in chapter 2 have been achieved exploiting a combination of frequency scanning of the input optical pulse and OTDR technique [6]. Firstly, a 10 cm-long high reflectivity FBG has been used as liquid level and temperature gradient sensor. A 10 ps optical pulse, having a duration much shorter than the transit time through the grating, has been used as interrogating signal. Measurements have been performed with a spatial resolution of 1 mm depending on the incident pulse duration, such as any OTDR-based method. Subsequently, the possibility of realizing a long range FBGs-based sensor for spot events detection has been investigated. For a large-scale sensor, ultra weak reflectivity elements are required to let the incident signal propagate along the entire sensing length. However, since the fabrication of a long continuous, ultra weak and homogeneous FBG is an expensive and complicated issue, we have proposed a sensor made of an array of 500 identical ultra weak FBGs written in cascade along a 5 m optical fiber. Despite the most common approach to interrogate an ultra weak FBGs sensing network is to use optical pulses much shorter than the transit time of the light through two adjacent sensing units [7, 8], we have demonstrated the possibility of interrogating a large-scale FBGs-based sensor using pulses greater than the transit time of the light through consecutive gratings. This alleviates the requirement for ultra short optical pulses and hence reducing the cost and complexity of the interrogation system. Both spatial and temperature resolution come from the interrogating pulse duration and there is a clear trade-off between these parameters, resulting from the time-frequency fundamental duality. A spatial resolution of 9 mm (ultimately dictated by one FBG length) and a temperature resolution of less than 2.62°C have been obtained with a 80 ps optical pulse; while a 5 cm spatial resolution and a temperature resolution of less than 0.42°C have been demonstrated by using a 500 ps incident pulse. Furthermore, the temperature of the spot event has been calculated with an estimated accuracy of less than 0.6°C, being this value a rough approximation that can certainly be improved by implementing standard fitting techniques. Besides, as the measurement range is essentially dictated by the length of the sensor itself, large scale sensing network only requires a longer FBGs array with no need to enhance the bandwidth in the acquisition electronics. Due to the high sensitivity of the FBG spectrum to temperature and/or strain changes, the system presents great potential for the development of a simple solution for distributed fiber sensing with no need of optical pumping and/or sophisticated controlling systems. Furthermore, as no ultra-short optical pulses have been employed, the technology proposed alleviates the instrumentation

complexity and drastically simplifies the measurement scheme as the strength for ultra-short optical pulses is lowered.

In chapter 3, a technique inspired on the operation principle of discrete time MWP filters has been employed to interrogate photonic sensors based on different FBG structures. This technique brings several advantages derived from the fact that it relies on microwave rather than on optical interferences. Microwave interferometry is by far more stable and easier to control and, if suitably combined with photonics, provides a remarkable spatial accuracy. Furthermore, since the sensor is based on a discrete time filter configuration, the system spectral performance can be properly tailored/reconfigured. Relying on microwave interferometry and working under incoherent operation, the configuration proposed is intrinsically robust against environmental changes, stable and with good repeatable performance [9, 10]. Also, this technique is potentially low cost as it is based on low bandwidth radio-frequency (RF) and off-the-shelf photonic components rather than on ultra short pulses, optical interferometry or OFDR techniques. Firstly, the feasibility of the MWP filtering technique to interrogate a 10 cm-long high reflectivity FBG has been demonstrated. However, due to the high reflectivity of the grating, this device is actually not able to detect events having the same magnitude. To overcome this limitation a pair of identical low reflectivity FBGs has been employed as sensing device. The latter has laid the foundation for the implementation of a large scale sensing network, based on 500 ultra weak FBGs written in cascade along a 5 m fiber optic. The detection of spot events has been demonstrated with remarkable spatial accuracy of less than 1 mm, using RF devices with a modest bandwidth of only 500 MHz. Since the spatial accuracy basically depends on the system frequency step, the MWP-based method will be certainly able to reach the same performance in terms of accuracy even if the length of the sensing device is enhanced to obtain a higher measurement range. Furthermore, the temperature of the hot spot can be evaluated due to the progressive scan of the central wavelength of the tunable bandpass filter, without using any more devices or additional wavelength scanned systems, with a measured accuracy of less than 1°C.

Fiber optic sensors based on customized LPGs have been presented and validated in chapter 4. A new scheme for fiber optic liquid level sensor based on a pair LPG-FBG and MWP filtering technique has been proposed. To the best of our knowledge, this is the first demonstration of a LPG sensor interrogated with a RF based scheme, as LPG sensors have been generally interrogated by means of a broadband source (BBS) and an optical spectrum analyzer (OSA) [11–13]. The sensing pair LPG-FBG has been employed to obtain the two taps of a MWP filter. When the liquid level surrounding the sensor has been increased, the LPG resonance has moved towards lower wavelengths and hence the magnitude of the tap related to the LPG has grown, causing a gradual imbalance between the weights of the two taps of the MWP filter. This intensity imbalance has caused, in turn, a step-wise reduction of the MWP filter visibility. By monitoring the latter,

the measurement of the liquid level has been achieved. Several sets of experimental measurements have been collected in order to prove the stability and repeatability of the sensor, demonstrating a sensitivity of -12.71 dB/cm and a standard deviation of 0.52 dB. The measurement range of 4 cm is limited by the physical length of the LPG but it may be certainly enhanced by fabricating a longer grating. Besides, the frequency period of the two-tap MWP filter can be suitably chosen by opportunely tailoring the optical path difference of the configuration. Hence, the operating frequency range can be further reduced below the 500 MHz, lowering the system cost and complexity and improving the interrogation speed. Furthermore, a temperature and relative humidity (RH) sensor based on a half-coated LPG has been presented. To our knowledge, this is the first time that a partially coated LPG is applied as sensing device, which allows simultaneous response for two different external magnitudes. Firstly, the optical response of a LPG has been studied when a polymeric thin film was built-up onto the cladding by using the layer-by-layer (LbL) assembly method [14]. Then, half of the LbL coating has been chemically removed. The half-coated LPG provided a split of the attenuation band observed in the full-coated LPG into two components (as theoretically investigated in previous work [15]), presenting different behavior in temperature and humidity. The half-coated LPG has been also exposed to humidity and temperature cycles, obtaining a dual-wavelength sensing mechanism based on the shifts of both contributions. The dual-wavelength based measurements provided a simultaneous monitoring of RH and temperature, with sensitivity ratios of -63.23 pm/%RH and -410.66 pm/°C for the attenuation band corresponding to the coated contribution, and 55.22 pm/%RH and -405.09 pm/°C for the attenuation band corresponding to the uncoated grating. This novel, simple and cost-efficient approach could be a good alternative to the cascaded-LPGs sensing systems where the use of at least two gratings is required to simultaneously monitor two different parameters.

Finally, in chapter 5, a technique to enhance the response of Brillouin distributed sensors has been proposed and demonstrated, consisting in creating a multi-frequency pump pulse interacting with a multi-frequency continuous-wave probe. Brillouin-based distributed optical fiber sensing has been demonstrated to offer novel and outstanding capabilities, providing distributed strain and temperature measurements along many tens of kilometers with relative fine spatial resolution [16, 17]. The Brillouin optical time domain analysis (BOTDA) system described in this chapter is based on a method developed to by-pass the fundamental limits given by fiber nonlinearities and pump depletion which limit the maximum power that can be launched into the sensing fiber [18, 19]. A combination of time-division and frequency-division multiplexing, that is realized exploiting a smart all-fiber device containing a set of 7 cm-long FBGs, has been used. Indeed, pump pulses showing $N = 3$ frequency components are employed to produce Brillouin amplification along the sensing fiber. This way, the total power launched into the fiber has been increased, while the power in individual pulses has been kept below the threshold of nonlinearities. Hence the sensor response can be arbitrarily multiplied by integer steps N and is eventually limited by the added

complexity of the passive time-frequency mux-demux device. Experimental results indicates that the use of three frequency components increases the sensor response by a factor 3, corresponding to a signal-to-noise ratio (SNR) enhancement of 4.8 dB. The additional SNR achieved by using this configuration can be useful to extend the sensing range, to reduce measurement time, and/or to improve spatial and measured resolutions. An accuracy of 1.8 MHz has been obtained with the standard scheme, while an improved accuracy down to 0.6 MHz has been reached when $N = 3$ spectral components have been used. Also, the spatial resolution of the BOTDA method has been experimentally validated by provoking a 2 m-long hot spot in the sensing fiber near the farthest end. A correct determination of the temperature has been obtained within the hot region and the 2.0 m spatial resolution has not been negatively affected. This multi-frequency scheme offers many advantages if compared to alternative approaches: simple direct detection has been employed, without using sophisticated detection schemes based for instance on coherent detection. Moreover, the frequency scan, the acquisition and data process remain unmodified from the standard BOTDA scheme. Finally, the sensor response and SNR improvement provided by the proposed BOTDA technique could be further enhanced by using a large number of spectral components, resulting in a very attractive solution for long measurement range.

6.2 Direction for future research

Although the customized grating sensors and devices reported in this dissertation have demonstrated unprecedented capabilities for the discrimination of liquid level, temperature and humidity and for improving the interrogation process of optical fiber sensing systems, the optimization of their performance and demonstration of further applications in the fields described above will require additional study and research.

In particular, the open research lines include:

- Find a proper mechanism for the liquid level detection that can make the system proposed in chapter 2 able to detect the liquid level even if the temperature change between the liquid and the surrounding ambient is of a few degree or when no temperature difference is produced.
- Find a measurement mechanism or a post-processing scheme that can alleviate the effect of coherence interferences in the time-frequency domain analysis performed for the 5 m-long FBG cascade sensor.
- Mathematically improve the algorithm used for calculating the inverse Fourier transform (IFT) in order to enhance the sensor performance in terms of minimum detectable event and two-events spatial resolution, and/or to reduce the frequency bandwidth requirement.

- Improve the performance of the LPG-based liquid level sensor by replacing the FBG with another LPG which presents a high temperature sensitivity.
- Combine the advantages of the MWP filtering technique with the potential of the partially coated LPG in order to achieve multi-parameters sensors able to simultaneously discriminate two or more physical magnitudes.
- Exploit the potential of the time-frequency multiplexing BOTDA by using a large number of frequency components N, with the purpose to enhance the sensor response in terms of SNR, sensing range, spatial and measurand resolution.
- Exhaustively study and eventually increase the performance of the presented sensors and technologies in term of resolution, accuracy and measurement range and perform experimental tests for distributed sensing.
- Evaluate the feasibility of using customized fiber optic tapers and nanowires which opportunely integrated with grating structures can implement new platforms for photonic sensors.

Bibliography

[1] M. Volanthen, H. Geiger, and J. Dakin, "Distributed grating sensors using low-coherence reflectometry," *J. Lightwave Technol.*, vol. 15, pp. 2076–2082, Nov 1997.

[2] K. Hotate and K. Kajiwara, "Proposal and experimental verification of Bragg wavelength distribution measurement within a long-length FBG by synthesis of optical coherence function," *Opt. Express*, vol. 16, pp. 7881–7887, May 2008.

[3] M. Froggatt and J. Moore, "High-spatial-resolution distributed strain measurement in optical fiber with Rayleigh scatter," *Appl. Opt.*, vol. 37, pp. 1735–1740, Apr 1998.

[4] L. Thévenaz, S. Chin, J. Sancho, and S. Sales, "Novel technique for distributed fibre sensing based on faint long gratings (FLOGs)," in *Proc. SPIE*, vol. 9157, pp. 91576W–91576W–4, Jun 2014.

[5] J. Sancho, S. Chin, D. Barrera, S. Sales, and L. Thévenaz, "Time-frequency analysis of long fiber Bragg gratings with low reflectivity," *Opt. Express*, vol. 21, pp. 7171–7179, Mar 2013.

[6] M. K. Barnoski, M. D. Rourke, S. M. Jensen, and R. T. Melville, "Optical time domain reflectometer," *Appl. Opt.*, vol. 16, pp. 2375–2379, Sep 1977.

[7] C. Hu, H. Wen, and W. Bai, "A novel interrogation system for large scale sensing network with identical ultra-weak fiber Bragg gratings," *J. Lightwave Technol.*, vol. 32, pp. 1406–1411, Apr 2014.

[8] W. Bai, H. Yu, D. Jiang, and M. Yang, "All Fiber Grating (AFG): a new platform for fiber optic sensing technologies," in *Proc. SPIE*, vol. 9634, pp. 96342A–96342A–4, Sep 2015.

[9] J. Capmany, B. Ortega, D. Pastor, and S. Sales, "Discrete-time optical processing of microwave signals," *J. Lightwave Technol.*, vol. 23, p. 702, Feb 2005.

[10] J. Capmany, J. Mora, I. Gasulla, J. Sancho, J. Lloret, and S. Sales, "Microwave photonic signal processing," *J. Lightwave Technol.*, vol. 31, pp. 571–586, Feb 2013.

[11] S. Khaliq, S. W. James, and R. P. Tatam, "Fiber-optic liquid-level sensor using a long-period grating," *Opt. Lett.*, vol. 26, pp. 1224–1226, Aug 2001.

[12] H. Fu, X. Shu, A. Zhang, W. Liu, L. Zhang, S. He, and I. Bennion, "Implementation and characterization of liquid-level sensor based on a long-period fiber grating Mach-Zehnder interferometer," *Sensors Journal, IEEE*, vol. 11, pp. 2878–2882, Nov 2011.

[13] H. Xue, Z. Xu, H. Chen, Y. Yang, J. You, J. Yan, H. Fu, and D. Zhang, "Continuous liquid level sensor based on a reflective long period fiber grating interferometer," *Measurement Science and Technology*, vol. 26, no. 3, p. 037001, 2015.

[14] X. Zhang, H. Chen, and H. Zhang, "Layer-by-layer assembly: from conventional to unconventional methods," *Chem. Commun.*, vol. 14, pp. 1395–1405, 2007.

[15] J. Bao, P. Cheng, H. Zhao, J. Wang, and L. Wu, "Spectral characteristics of a two-section multilayer long-period fiber grating sensor," *Optik - International Journal for Light and Electron Optics*, vol. 125, pp. 4689–4693, Sep 2014.

[16] L. Thévenaz, A. Denisov, and M. A. Soto, "Brillouin distributed fiber sensing at ultra-high spatial resolution," in *IEEE Photonics Conference (IPC) 2015*, pp. 337–338, IEEE, Oct 2015.

[17] Y. London, Y. Antman, N. Levanon, and A. Zadok, "Brillouin analysis with 8.8 km range and 2 cm resolution," in *Proc. SPIE*, vol. 9634, pp. 96340G–96340G–4, Sep 2015.

[18] S. M. Foaleng and L. Thévenaz, "Impact of Raman scattering and modulation instability on the performances of Brillouin sensors," in *Proc. SPIE*, vol. 7753, pp. 77539V–77539V–4, May 2011.

[19] M. Alem, M. A. Soto, and L. Thévenaz, "Modelling the depletion length induced by modulation instability in distributed optical fibre sensors," in *Proc. SPIE*, vol. 9157, pp. 91575S–91575S–4, Jun 2014.

Appendix A

Publications

A.1 Journal

- **A. L. Ricchiuti**, D. Barrera, A. Urrutia, J. Goicoechea, F. J. Arregui, and S. Sales, "Continuous liquid level sensor based on a long period grating and microwave photonics filtering techniques," IEEE Sensors Journal, vol. 16, no. 6, pp. 1652-1658, Mar. 2016.
- **A. L. Ricchiuti** and S. Sales, "Spot events detection along a large scale sensor based on ultra weak FBGs using time-frequency analysis," Applied Optics, vol. 55, no. 5, pp. 1054-1060, Feb. 2016.
- A. Urrutia, J. Goicoechea, **A. L. Ricchiuti**, D. Barrera, S. Sales, and F. J. Arregui, "Simultaneous measurement of humidity and temperature based on a partially coated optical fiber long period grating," Sensors and Actuators B: Chemical, vol. 227, pp. 135-141, May 2016.
- **A. L. Ricchiuti**, J. Hervás, and S. Sales, "Cascade FBGs distributed sensors interrogation using microwave photonics filtering techniques," Optics & Laser Technology, vol. 77, pp. 144-150, Mar. 2016.
- **A. L. Ricchiuti**, J. Hervás, D. Barrera, S. Sales, and J. Capmany, "Microwave photonics filtering technique for interrogating very-weak fiber Bragg grating cascade sensor," IEEE Photonics Journal, vol. 6, no. 6, pp. 1-10, Dec. 2014.
- M. A. Soto, **A. L. Ricchiuti**, L. Zhang, D. Barrera, S. Sales, and L. Thévenaz, "Time and frequency pump-probe multiplexing to enhance the signal response of Brillouin optical time-domain analyzers," Optics Express vol. 22, no. 23, pp. 28584-28595, Nov. 2014.
- **A. L. Ricchiuti**, D. Barrera, K. Nonaka, and S. Sales, "Temperature gradient sensor based on a long-fiber Bragg grating and time-frequency analysis," Optics Letters, vol. 39, no. 19, pp. 5729-5731, Oct. 2014.

- **A. L. Ricchiuti**, D. Barrera, S. Sales, L. Thévenaz, and J. Capmany, "Long weak FBG sensor interrogation using microwave photonics filtering technique," IEEE Photonics Technology Letters, vol. 26, no. 20, pp. 2039-2042, Oct. 2014.
- **A. L. Ricchiuti**, D. Barrera, S. Sales, L. Thévenaz, and J. Capmany, "Long fiber Bragg grating sensor interrogation using discrete-time microwave photonic filtering techniques," Optics Express vol. 21, no. 23, pp. 28175-28181, Nov. 2013.

A.2 Conference

- S. Sales, **A. L. Ricchiuti**, J. Hervás, D. Barrera, and J. Capmany, "Sensor distribuido basado en FBGs débiles en cascada utilizando técnicas de fotónica de microondas," in XXX Simposium Nacional de la Unión Científica Internacional de Radio (URSI 2014), Navarra (Spain), 2-4 Sep. 2015.
- A. Urrutia, J. Goicoechea, **A. L. Ricchiuti**, D. Barrera, S. Sales, and F. J. Arregui, "Sensitivity enhancement in fiber optic humidity sensors based on nano-coated long-period gratings," in XXX Simposium Nacional de la Unión Científica Internacional de Radio (URSI 2014), Navarra (Spain), 2-4 Sep. 2015.
- **A. L. Ricchiuti** and S. Sales, "Fiber optic sensor interrogation using microwave photonics filtering technique," in Conference on Substrate Integrated Waveguides and related Technology (CSIWT 2015), Bari (Italy), 15 May 2015.
- V. Portosi, G. Palma, T. Landeau, **A. L. Ricchiuti**, and F. Prudenzano, "SIW and optical technologies in MOE-Lab at Magna Grecia center, Politecnico di Bari," in Conference on Substrate Integrated Waveguides and related Technology (CSIWT 2015), Bari (Italy), 15 May 2015.
- S. Sales, **A. L. Ricchiuti**, J. Hervás, D. Barrera, and J. Capmany, "Microwave photonics filtering technique for interrogating distributed sensors based on series of FBGs," in Energy, Materials and Nanotechnology (EMN) Meeting in Optoelectronics, Beijing (China), 24-27 Apr. 2015.
- **A. L. Ricchiuti**, D. Barrera, K. Nonaka, and S. Sales, "Temperature gradient measurements based on a long fiber Bragg grating and time-domain analysis," in IEEE Sensors 2014, Valencia (Spain), 2-5 Nov. 2014.
- **A. L. Ricchiuti**, D. Barrera, S. Sales, L. Thévenaz, and J. Capmany, "Long fiber Bragg gratings for liquid level sensing," in XXIX Simposium Nacional de la Unión Científica Internacional de Radio (URSI 2014), Valencia (Spain), 3-5 Sep. 2014.
- **A. L. Ricchiuti**, D. Barrera, K. Nonaka, and S. Sales, "Temperature gradient sensor based on a long fiber Bragg grating and time waveform

analysis," in Advanced Photonics Congress, Barcelona (Spain), 27-31 Jul. 2014.

- J. Hervás, **A. L. Ricchiuti**, D. Barrera, S. Sales, L. Thévenaz, and J. Capmany, "Weak fiber Bragg grating cascade sensor interrogation using microwave photonic filtering techniques," in Advanced Photonics Congress, Barcelona (Spain), 27-31 Jul. 2014.
- M. Soto, **A. L. Ricchiuti**, L. Zhang, D. Barrera, S. Sales, and L. Thévenaz, "Enhanced response in Brillouin distributed optical fibre sensors by simultaneous time and frequency pump multiplexing," in 23rd Optical Fiber Sensors Conference (OFS 2014), Santander (Spain), 2-6 Jun. 2014.
- **A. L. Ricchiuti**, D. Barrera, S. Sales, L. Thévenaz, and J. Capmany, "Microwave photonics filtering technique for interrogating long weak fiber Bragg grating sensors," in 23rd Optical Fiber Sensors Conference (OFS 2014), Santander (Spain), 2-6 Jun. 2014.
- **A. L. Ricchiuti**, D. Barrera, K. Nonaka, and S. Sales, "Fiber-optic liquid level sensor using a long fiber Bragg grating," in the 5th European Workshop on Optical Fibre Sensors (EWOFS 2013), Kracow (Poland), 19-22 May 2013.

Appendix B

Other publications

Other works based on fiber grating structures and photonic-assisted radio-frequency techniques have been also investigated and carried out, leading to the dissemination of the following contributions, which, however, are not directly related to the content of this Ph.D. thesis.

B.1 Journal

- J. Perez, I. Suárez, J. Hervás, **A. L. Ricchiuti**, J. P. Martínez-Pastor, and S. Sales, "Continuous broadband MWP true-time delay with PbS-PMMA and -SU8 waveguides," to be published in IEEE Photonics Technology Letters (doi: 10.1109/LPT.2016.2561401).
- **A. L. Ricchiuti**, I. Suárez, D. Barrera, P. J. Rodríguez-Cantó, C. R. Fernández-Pousa, R. Abargues, S. Sales, J. Martínez-Pastor, and J. Capmany, "Colloidal quantum dots-PMMA waveguides as integrable microwave photonic phase shifters," IEEE Photonics Technology Letters, vol. 26, no. 4, pp. 402-404, Feb. 2014.
- G. Muñoz-Matutano, D. Rivas, **A. L. Ricchiuti**, D. Barrera, C. R. Fernández-Pousa, J. Martínez-Pastor, L. Seravalli, G. Trevisi, P. Frigeri, and S. Sales, "Time resolved emission at 1.3 μm of a single InAs quantum dot by using a tunable fibre Bragg grating," Nanotechnology, vol. 25, no. 3, pp. 035204-1-7, Jan. 2014.

B.2 Conference

- G. Muñoz-Matutano, D. Rivas, **A. L. Ricchiuti**, D. Barrera, C. R. Fernández-Pousa, J. Martínez-Pastor, L. Seravalli, G. Trevisi, P. Frigeri, and S. Sales, "Tunable fibre Bragg gratings at 1.3 μm to improve the characterization of InAs Quantum Dots," in Advanced Photonics Congress, Barcelona (Spain), 27- 31 Jul. 2014.
- G. Muñoz-Matutano, D. Rivas, **A. L. Ricchiuti**, J. Bosch, D. Barrera, C. R. Fernández-Pousa, L. Seravalli, G. Trevisi, P. Frigeri, J. Martínez-Pastor, and S. Sales, "Exciton recombination dynamics of single InAs Quantum Dots emitting at long wavelengths," in International Conference on Quantum Dots (QD 2014), Pisa (Italy), 11-16 May 2014.
- **A. L. Ricchiuti**, I. Suárez, D. Barrera, P. J. Rodríguez-Cantó, R. Abargues, C. R. Fernández-Pousa, J. P. Martínez-Pastor, S. Sales, and J. Capmany, "Integrable microwave photonic phase-shifter based on colloidal quantum dots-PMMA waveguide," in 2013 IEEE Topical Meeting on Microwave Photonics (MWP 2013), Alexandria (USA), 28-31 Oct. 2013.
- **A. L. Ricchiuti**, I. Suárez, D. Barrera, P. J. Rodríguez-Cantó, R. Abargues, C. R. Fernández-Pousa, J. P. Martínez-Pastor, and S. Sales, "Desfasadores fotónicos integrados basados en guías de onda de puntos cuánticos embebidos en PMMA," in the VIII Reunión Española de Optoelectrónica (OPTOEL 2013), Alcalá de Henares (Spain), 10-12 Jul. 2013.
- **A. L. Ricchiuti**, I. Suárez, D. Barrera, P. J. Rodríguez-Cantó, R. Abargues, C. R. Fernández-Pousa, J. P. Martínez-Pastor, and S. Sales, "Integrated microwave photonic phase-shifters based on colloidal quantum dots-PMMA nanocomposite waveguides," in the 15th International Conference on Transparent Optical Networks (ICTON 2013), Cartagena (Spain), 23-27 Jun. 2013.